ENGINEERED 3D DNA CRYSTALS: CHARACTERIZATION, STABILIZATION AND APPLICATIONS

by

Zhe Li

A Dissertation

Submitted to the Faculty of Purdue University

In Partial Fulfillment of the Requirements for the degree of

Doctor of Philosophy

Department of Chemistry

West Lafayette, Indiana

May 2019

THE PURDUE UNIVERSITY GRADUATE SCHOOL
STATEMENT OF COMMITTEE APPROVAL

Dr. Chengde Mao, Chair
Department of Chemistry
Dr. Jong Hyun Choi
School of Mechanical Engineering
Dr. Wen Jiang
Department of Biological Science
Dr. Shelley Claridge
Department of Chemistry

Approved by:

Dr. Christine A. Hrycyna
Head of the Graduate Program

For my dear parents and fiancee

ACKNOWLEDGMENTS

First, I would like to give my deepest gratitude to my advisor Professor Chengde Mao. Over the years, Chengde inspired me with his broad vision of the scientific field and gave me the firmest support for my research. His creative and critical thinking about science guided me throughout my Ph.D. study and will continue to benefit me in my career. His enthusiasm and integrity in research also set up a bright model for me to follow.

Besides my advisor, I would like to thank all members of my thesis committee: Dr. Jong Hyun Choi, Dr. Jiang Wen, and Dr. Shelley Claridge. I appreciate their suggestions and help in my study.

I would also like to thank all members of Mao's lab: Longfei Liu, Dr. Jiemin Zhao, Dr. Yulin Li, Dr. Qian Li, Dr. Siyu Wu, Dr. Mo Li, Dr. Jinwen Yu, Dr. Zhiyu Liu, Mengxi Zheng, Dake Mao, Swati Arora, Dr. Hua Zuo, Dr. Guofang Chen, Dr. Jing Zhang, Dr. Yong Wang, Dr. Xinfeng Zhao, Kai He, Dr. Dae-Ro Ahn, Dr. Qian Li (Northwest Univ.), Dr. Weili Li, Dr., Yuyan Yan, Dr. Huzhi Zheng, Emily Ankrom, Shuaikang Du and Gefan He. Their accompany brings color and happiness to my graduate school life.

For my research projects, I appreciate Dr. Patricia Bishop, Dr. Hartmut Hedderich's training in Amy facility, Laurie Mueller, Dr. Christopher Gilpin, Dr. Kunpeng Li and Valorie Bowman's help in electron microscope, Tim Schmidt's help in X-ray diffraction, Dr. Jiazhang Qiu's help in protein expression and Dr. Andy Schaber's help in confocal microscope. I also appreciate Konrad Kliewer for his continuous effort in setting up our computational work station. For my coursework, I would like to thank Dr. Nikolai Skrynnikov, Dr. Jianguo Mei, Dr. Mary Wirth, Dr. Garth Simpson, Dr, Nicholas Noinaj, Dr. Gaurav Chopra and Dr. Minji Dai for their generous sharing of knowledge. Dr. Linda Mason's workshops inspired me a lot in science communications. I also gained great teaching experience in the team of General Chemistry and would like to thank Dr. Cindy Harwood, Marybeth Miller and all our teaching team members for their help and understanding. I am very fortunate to have great friends who shared with me their board games, music, Taekwondo and parties, which fulfills my spare time at Purdue.

I would like to thank my fiancée, Wenqi Du for her accompany all along, no matter when we are enjoying the breathtaking views by Lake Michigan, or when we are sharing our life across the Pacific Ocean.

Last but not least, I would like to thank my parents for their love and encouragement. I will bring their dreams with me and achieve new heights in my life.

TABLE OF CONTENTS

LIST OF FIGURES

ABSTRACT

Author: Li, Zhe. PhD
Institution: Purdue University
Degree Received: May 2019
Title: Engineered 3D DNA Crystals: Characterization, Stabilization and Applications
Committee Chair: Chengde Mao

In recent years, DNA nanotechnology has emerged as one of the most powerful strategies for bottom-up construction of nanomaterials. Due to the high programmability of DNA molecules, their self-assembly can be rationally designed. Engineered 3D DNA crystals, as critical products from the design of DNA self-assembly, have been proposed as the structural scaffolds for organizing nano-objects into three-dimensional, macroscopic devices. However, for such applications, many obstacles need to be overcome, including the crystal stability, the characterization methodology, the revision of crystal designs as well as the modulation of crystallization kinetics. My PhD research focuses on solving these problems for engineered 3D DNA crystals to pave the way for their downstream applications.

In this thesis, I started by enhancing the stability of engineered 3D DNA crystals. I developed a highly efficient post-assembly modification approach to stabilize DNA crystals. Enzymatic ligation was performed inside the crystal lattice, which was designed to covalently link the sticky ends at the crystal contacts. After ligation, the crystal became a covalently bonded 3D network of DNA motifs. I investigated the stability of ligated DNA crystals under a wide range of solution conditions. Experimental data revealed that ligated DNA crystals had significantly increased stability. With these highly stabilized DNA crystals, we then demonstrated their applications in biocatalysis and protein encapsulation as examples.

I also established electron microscope imaging characterization methods for engineered 3D DNA crystals. For crystals from large-size DNA motifs, they are difficult to study by X-ray crystallography because of their limited diffraction resolutions to no better than 10 Å. Therefore, a direct imaging method by TEM was set up. DNA crystals were either crushed or controlled to grow into microcrystals for TEM imaging. To validate the imaging results, we compared the TEM images with predicted models of the crystal lattice. With the advance in crystal characterization,

DNA crystals of varying pore size between 5~20 nm were designed, assembled, and validated by TEM imaging.

The post-assembly ligation was further developed to prepare a series of new materials derived from engineered 3D DNA crystals, which were inaccessible otherwise. With the directional and spatial control of ligation in DNA crystal, I prepared new DNA-based materials including DNA microtubes, complex-architecture crystals, and an unprecedented reversibly expandable, self-healing DNA crystal. The integration of weak and strong interactions in crystals enabled a lot of new opportunities for DNA crystal engineering.

In the final chapter, I investigated the effect of 5'-phosphorylation on DNA crystallization kinetics. I found that phosphorylation significantly enhanced the crystallization kinetics, possibly by strengthening the sticky-ended cohesion. Therefore, DNA crystals can be obtained at much lower ionic strength after phosphorylation. I also applied the result to controling the morphology of DNA crystals by tuning the crystallization kinetics along different crystallographic axes. Together with previously methods to slow down DNA crystallization, the ability to tune DNA crystallization kinetics in both ways is essential for DNA crystal engineering.

CHAPTER 1. INTRODUCTION

1.1 Structural DNA Nanotechnology

In biology, DNA molecules are often associated with heredity. They are known as the generic information that organisms pass down from one generation to the next generation. However, in structural DNA nanotechnology, we viewed the same molecule from a very different perspective. Here, DNA molecules are used as a building block for engineering materials. Because of the highly programmable specificity of DNA molecules, their self-assembly can be precisely designed and used to construct a large variety of nanomaterials. These materials have shown great potential in analytical, biomedical, electronic and computational applications[1].

Up to the present, structural DNA nanotechnology is a mature bottom-up strategy for constructing nanostructures of almost any artificial shapes and sizes. In this section, I will introduce the basic design principles of DNA self-assembly, which will be essentially helpful for us to better understand the design of engineered 3D DNA crystals in later chapters.

1.1.1 Design Principles of DNA Self-assembly

There are several reasons for choosing DNA molecules for self-assembly of nanomaterials (Figure 1-1). To begin with, the DNA molecule is a nanoscale object. For the B-form double helical structure of DNA, the most common form of DNA in solution, two antiparallel phosphate-sugar backbones winding around each other through the well-known Watson-Crick base pairing. The DNA duplex is around 2 nm in diameter and 10~10.5 base pairs per helical turn. The rise for each base pair is around 0.34 nm, which makes the rise of one helical turn around 3.4 nm. The nanoscale dimension of DNA makes it suitable for constructing nanomaterials. Second, the base pairing rule is simple to apply, and it results in a conserved secondary structure of DNA as a double helix. Adenine (A) base pair with thymine (T), and cytosine (C) base pair with guanine (G). The DNA sequence can be designed from the combinations of the four bases, and the complementary strand which binds with high specificity can then be easily predicted from the base-pairing rule. The strict base-pairing rule results in the high programmability in DNA molecules. The specificity of interactions between DNA molecules is incomparable for almost any other molecules. Apart from this, DNA molecules also have their advantages in stability. DNA molecules are much more stable

than RNA and proteins against degradation. For denatured DNA samples, their structure can be easily recovered by an annealing process. Another important advantage owes to the fast development of the chemical synthesis of DNA oligos. Nowadays, DNA molecules with custom defined sequence under 100 nucleotides can be regularly synthesized at relatively low cost. All these advantages make DNA molecules an attractive material for studying self-assembly and for constructing new materials by a bottom-up approach.

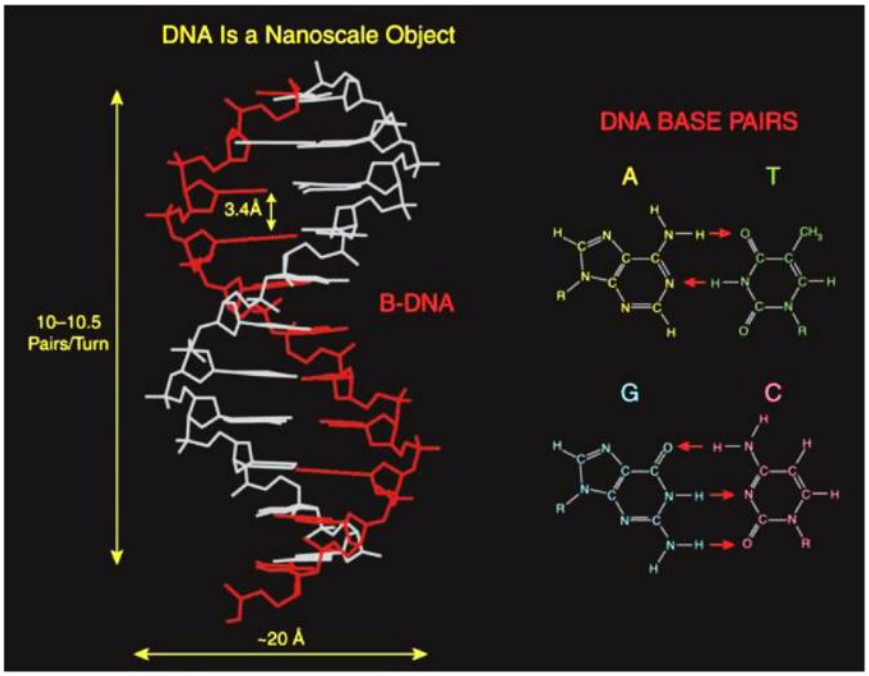

Figure 1-1 The Double Helical Structure of B-Form DNA and Four DNA Bases A, T, C and G[1]

The conceptual framework of structural DNA nanotechnology was proposed by Seeman in the early 1980s. In the past 30 years, DNA nanotechnology has achieved impressive progress in development. The technology is built upon three pillars[2]. The first one is the commercially available and affordable synthesis of custom DNA oligos as we just mentioned. The second one is stably branched DNA molecules (Figure 1-2a). This solves the problem that DNA molecules are conventionally a linear structure. The designed junctions enable DNA to extend in 2D and 3D for materials construction. The third one is sticky-ended cohesion (Figure 1-2b), which serves as the connector for designed branched DNA molecules. An example is shown for how a four-way branched molecule is connected via sticky-ended cohesion into a two-dimensional lattice (Figure 1-2a).

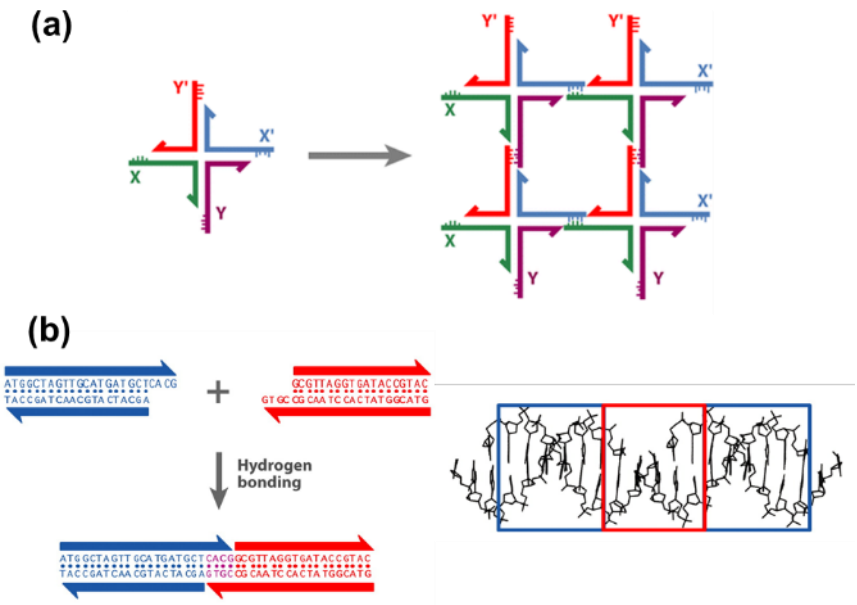

Figure 1-2 Three Pillars of Structural DNA Nanotechnology: Stably Branched DNA Molecules (a), Sticky-Ended Cohesion (b) and Convenient Synthesis of Designed DNA Sequences[2]

The first stable branched DNA molecule was designed and assembled in Seeman's lab in 1983[3]. Four different DNA strands were designed to associate into a four-way junction (Figure 1-3). The sequences were asymmetrically designed to ensure the specificity of the four 8-bp binding regions. Basing on the same idea, a 12 -way junction can be assembled by 12 different strands of designed, orthogonal sequences (Figure 1-3)[4].

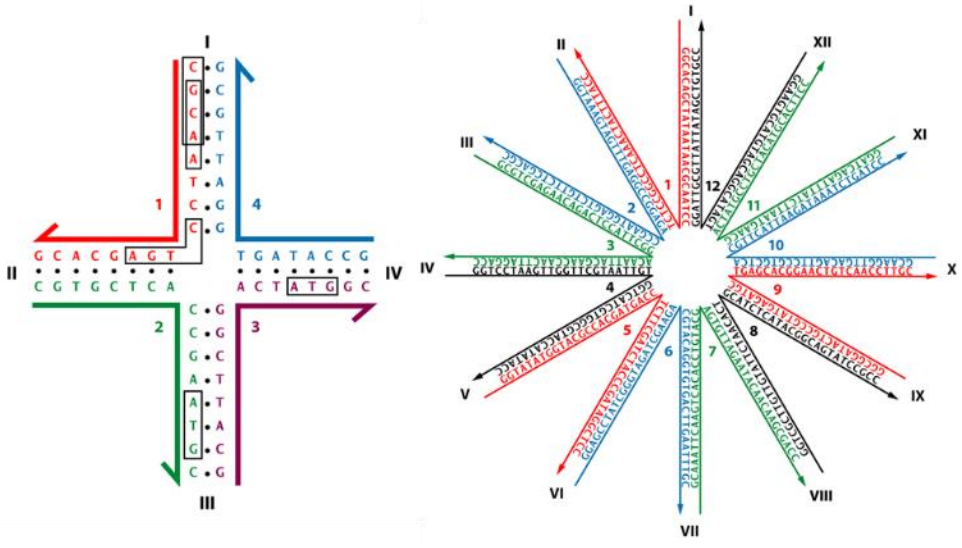

Figure 1-3 Sequence Design for 4-way and 12-way DNA Junction[2].

1.1.2 Tile-based Assembly of Robust DNA Motifs

However, these designed junctions are not ready for further self-assembly. They are very flexible in solution, and this has limited their self-assembly into larger structures. A conceptual tool, reciprocal exchange was applied between DNA duplex, and this was used to create junctions between nucleotides in proximity (Figure 1-4)[5]. Reciprocal exchange can recur 4-way junction by joining two duplexes at the center. Such connection was named as "crossover". By creating two crossovers, double-crossover (DX) molecules can be generated. This is one of the earliest motifs rigid enough for the construction of larger DNA self-assemblies. For example, 2D DNA crystal from DX molecules has been successfully assembled and characterized by AFM (Figure 1-5)[6]. Triple-crossovers can also be designed in the same fashion (Figure 1-4).

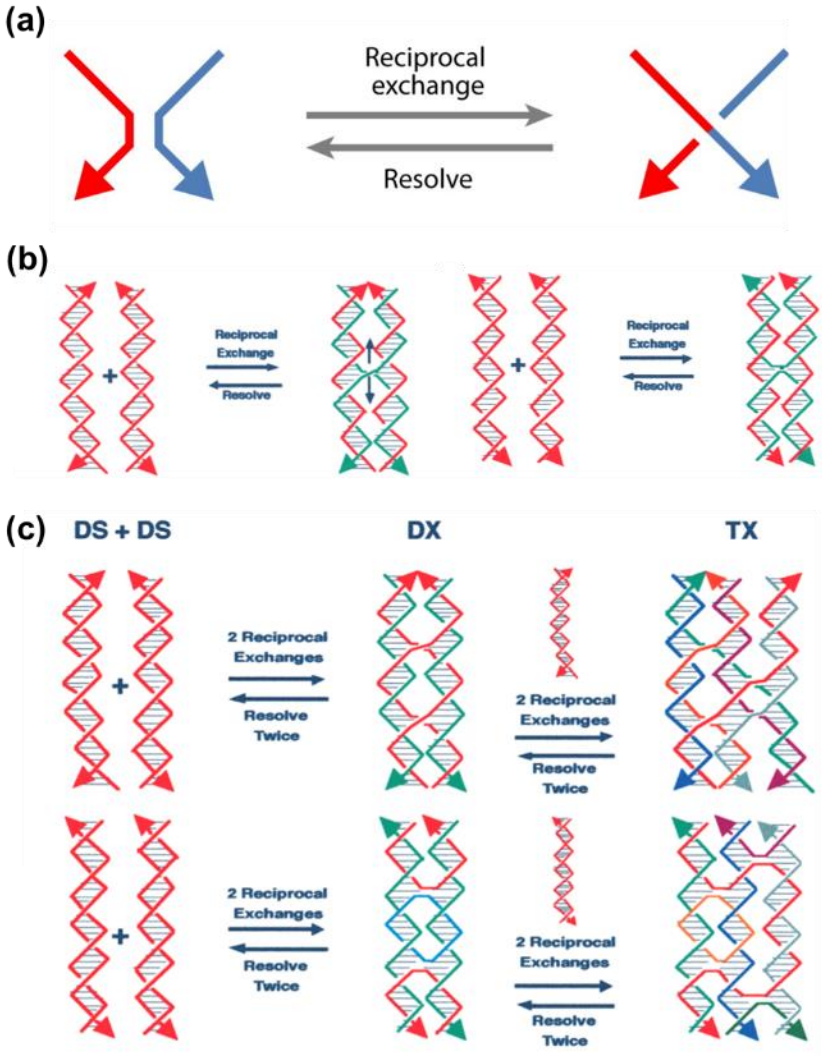

Figure 1-4 Reciprocal Exchange for Constructing Robust DNA Motifs[5]

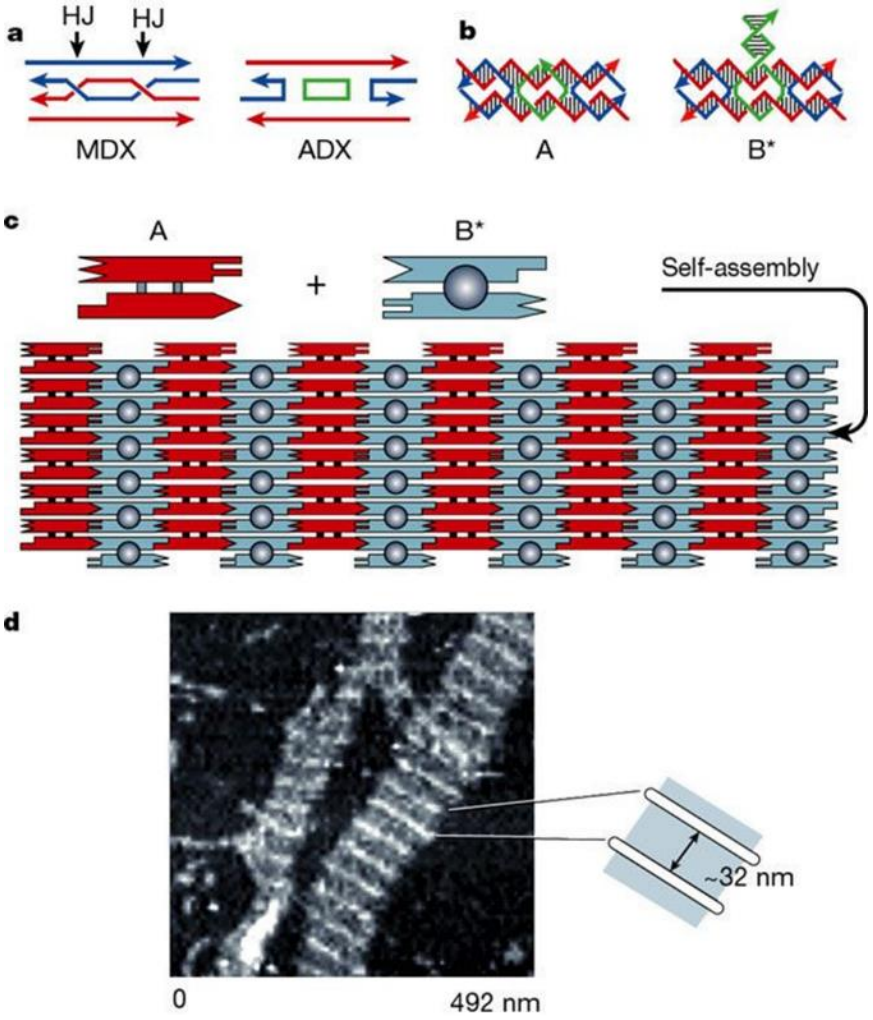

Figure 1-5 2D DNA Crystals Designed from the Self-assembly of DNA Double Crossover (DX) Motifs. HJ: Holliday junction; MDX: meiotic DX; ADX: analogue DX.[6,7]

Star motif has been created by arranging DX-molecules by rotational symmetry and joining them with linking loops of controlled flexibility. These star motifs have become versatile building blocks for 2D DNA crystalline arrays (Figure 1-6)[8–10] and 3D DNA nanocages (Figure 1-7)[10–12]. So far, the self-assembly of DNA nanostructures from rigid branched DNA motifs by sticky-ended cohesion has been summarized as "tile-based assembly" strategy. The development of this assembly strategy has been promoted by the design of novel motifs and the design of novel interaction interfaces other than sticky ends.

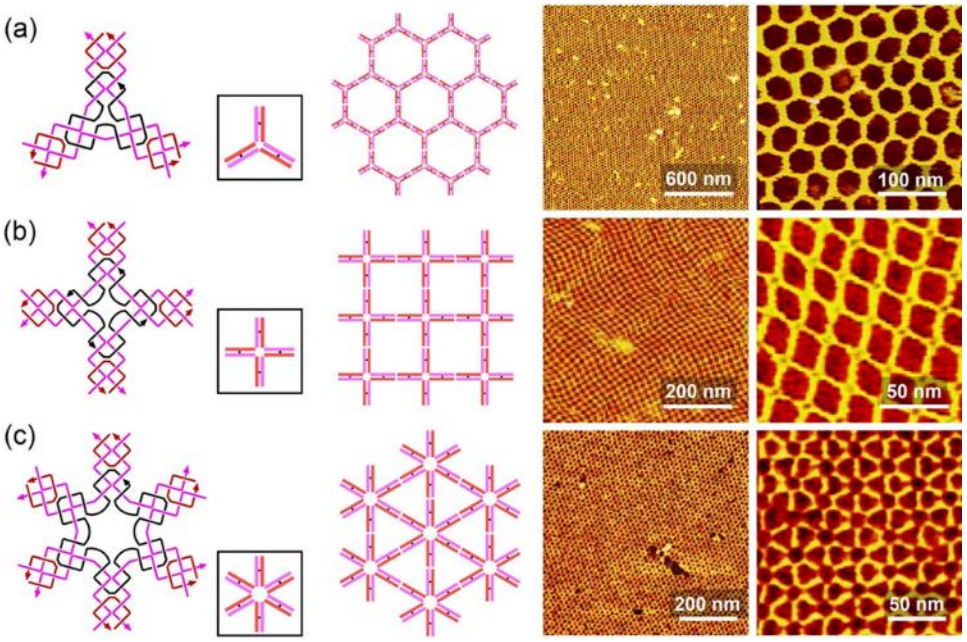

Figure 1-6 2D DNA Crystals Designed from the Self-assembly of DNA Star Motifs with 3-fold, 4-fold and 6-fold Symmetry[13].

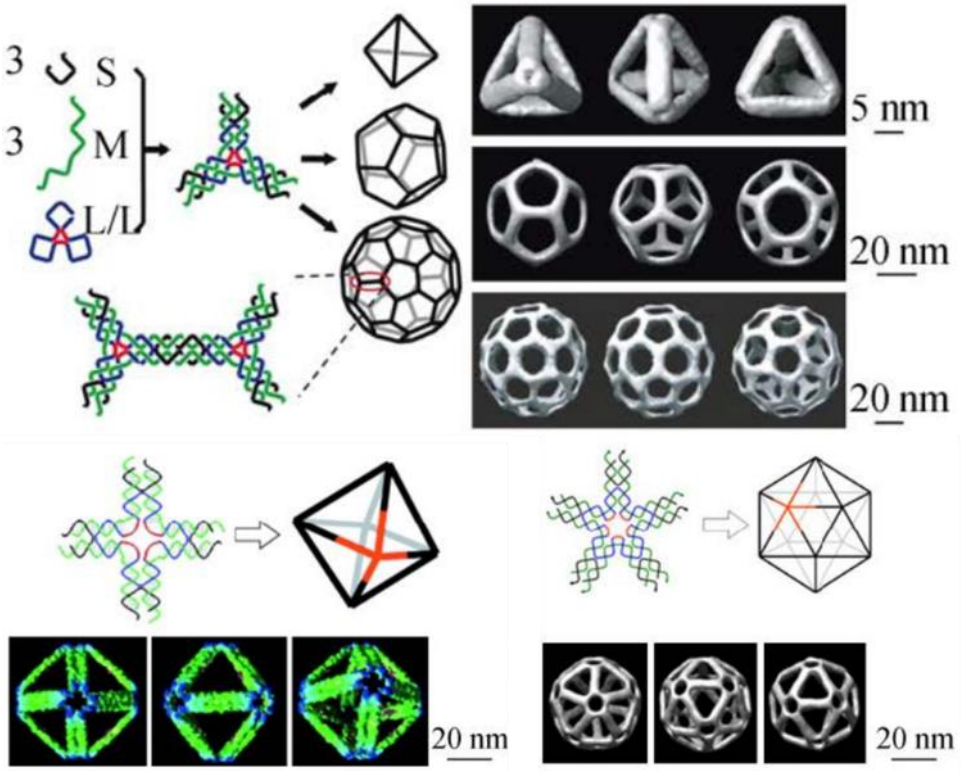

Figure 1-7 3D DNA Nanocages Designed from the Self-assembly of DNA Star Motifs [10–12].

1.1.3 DNA Origami and DNA Bricks

In 2006, “DNA origami” approach for creating DNA nanostructures was put forward by Rothemund (Figure 1-8)[14]. Unlike previous tile-based assembly that starts from DNA tiles, a long scaffold strand from virus DNA was folded by hundreds of short staple strands cooperatively into shapes and patterns. In 2010, another approach was developed by Yin by assembling DNA nanostructures from hundreds of different short DNA strands known as “DNA bricks”(Figure 1-9)[15]. These two methods both take advantage of the high programmable specificity of DNA molecules. The final assembled structures have no identical regions as in tile-based assembly, where symmetry is always applied to eliminate the number of distinct strands. DNA origami and DNA brick approaches with addressable complexity have enabled the design of almost any artificial 2D and 3D shapes from DNA molecules.

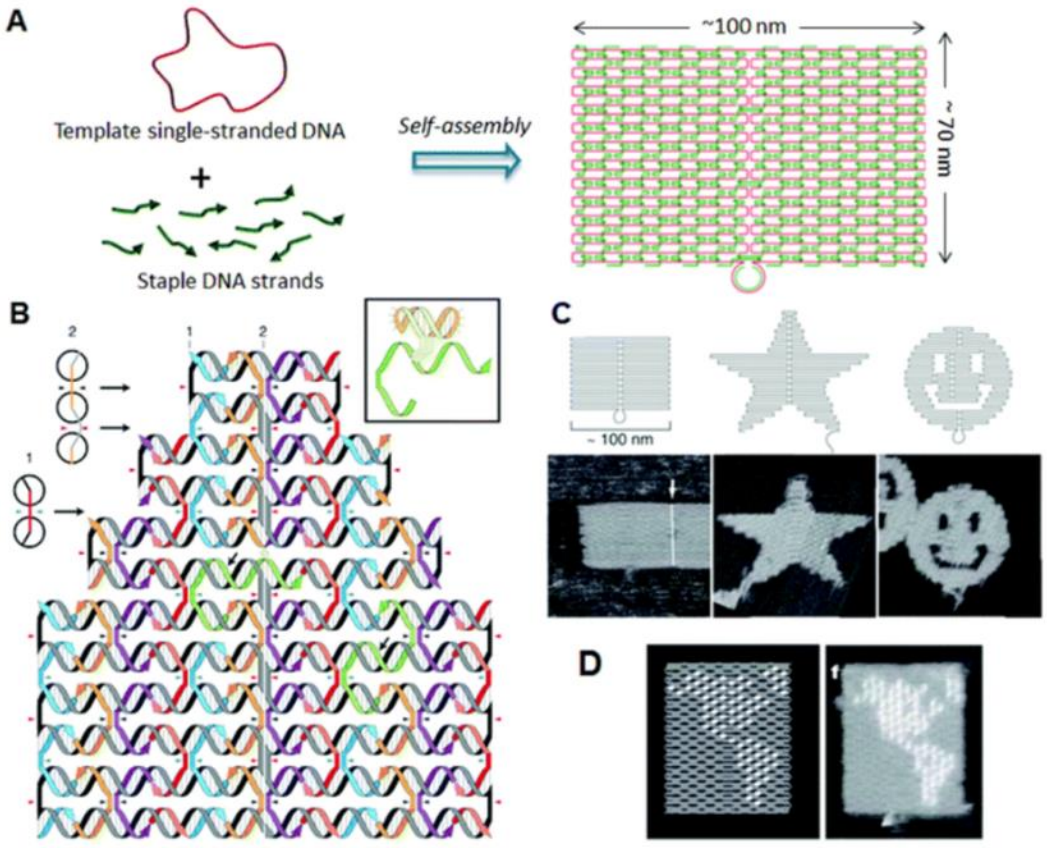

Figure 1-8 DNA Origami Approach for Designing DNA Self-assembly[14]

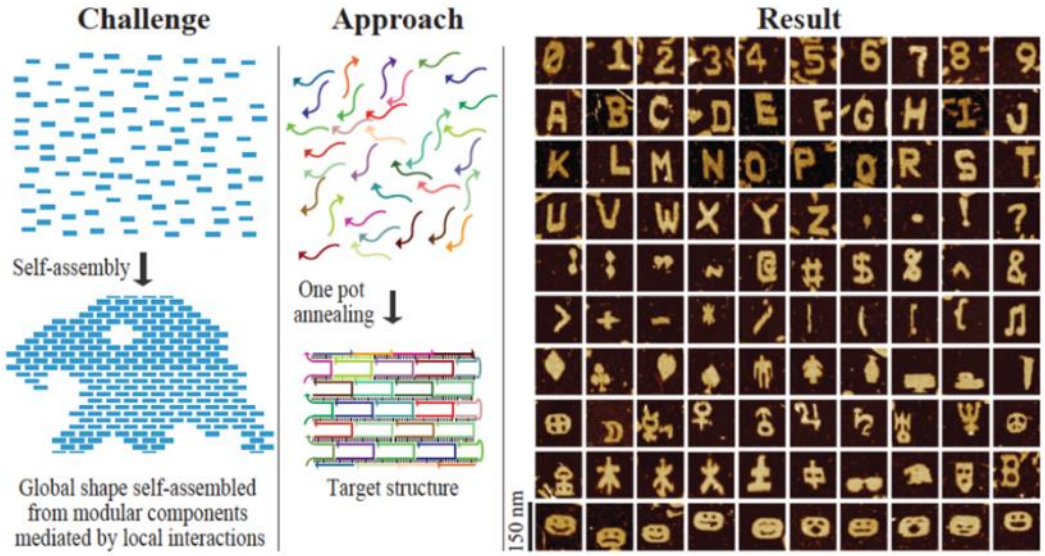

Figure 1-9 DNA Brick Approach for Designing DNA Self-assembly[15]

1.2 Rationally Designed 3D DNA Crystals

The idea of self-assembly DNA molecules into 3D crystals was the very initial motivation of Dr. Seeman when he started DNA nanotechnology[16]. He proposed to use 3D DNA crystals as a scaffold to put proteins that are hard to crystallize in a crystalline arrangement so that the structures of these proteins can be characterized by X-ray diffraction. Apart from this purpose, DNA crystal is a general macroscopic 3D scaffold for arranging materials into artificial devices. In this section, I will introduce how these 3D DNA crystals are designed, modulated and stabilized. The applications of these DNA crystals will be summarized in section 1.3 together with other porous crystalline materials.

1.2.1 Design of 3D DNA Crystals

The first design of a self-assembled 3D DNA crystal was established in 2009 by tile-based assembly[17]. A tensegrity triangle tile was first designed from DNA (Figure 1-10). The motif can be regarded as the joint of three stacked Holliday junctions. It is assembled from 7 DNA strands in total. This can be simplified into only 3 identical strands if 3-fold symmetry is applied. The DNA triangle tiles can further self-assemble in 3D by 2-nt sticky ends into rhombohedral symmetry lattice (Figure 1-11). The success of this DNA crystal designs owes to the construction of a rigid DNA motif with interacting interfaces in 3D space.

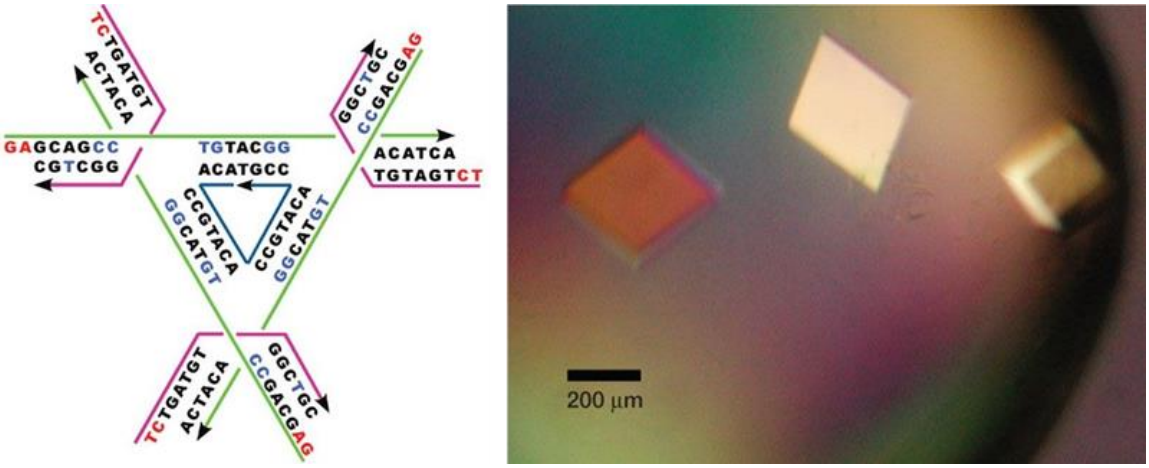

Figure 1-10 Schematic Design and Optical Images of 3D DNA Triangle Tensegrity Crystals[17]

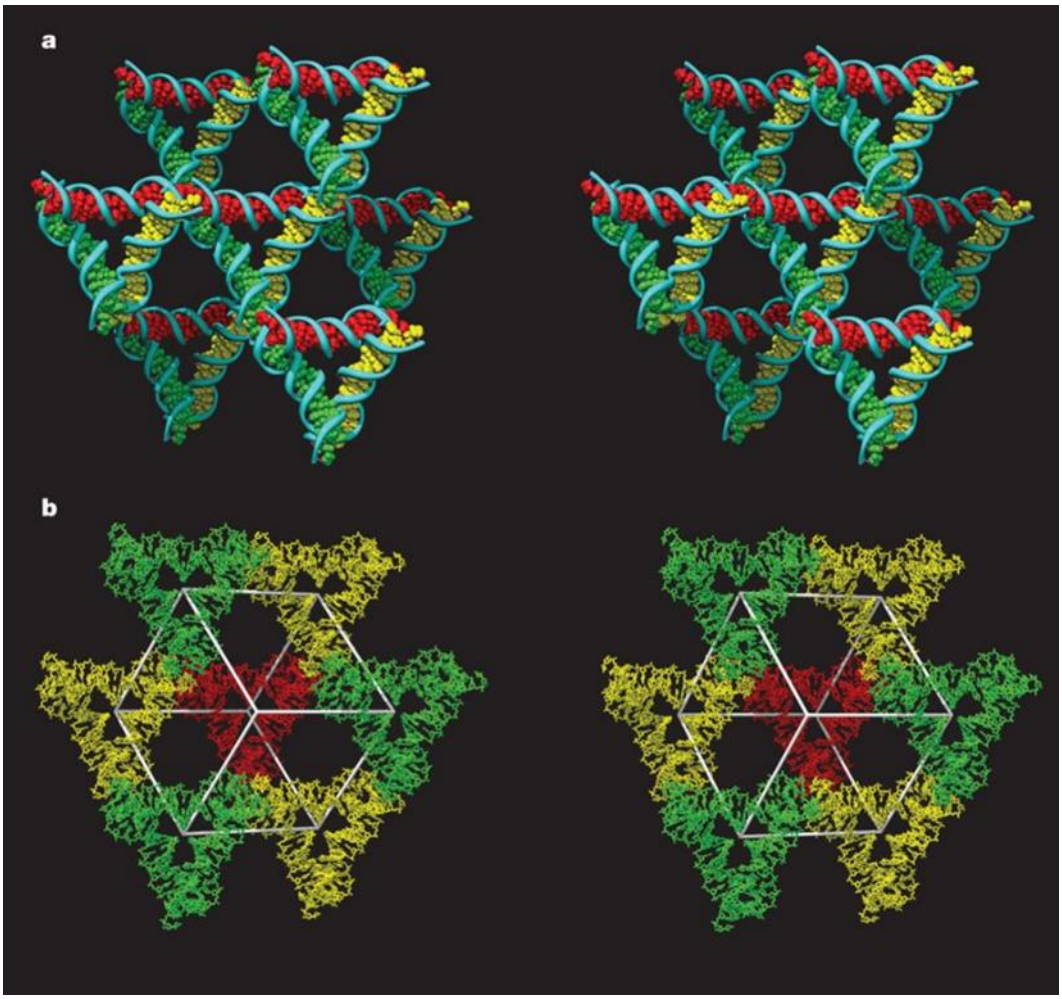

Figure 1-11 Crystal Unit Cell Formed by DNA Tensegrity Triangles[17]

In recent years, more varieties of 3D DNA crystals have been designed from Yan's group. Several designs were made from the complex arrangements of Holliday junctions by symmetry operations (Figure 1-12, 1-13)[18,19]. Yan's group also came up with a group of new DNA tiles by layered-crossovers. These new tiles were designed into 3D crystals by the continuous layering up of the 2D interactions (Figure 1-14)[20].

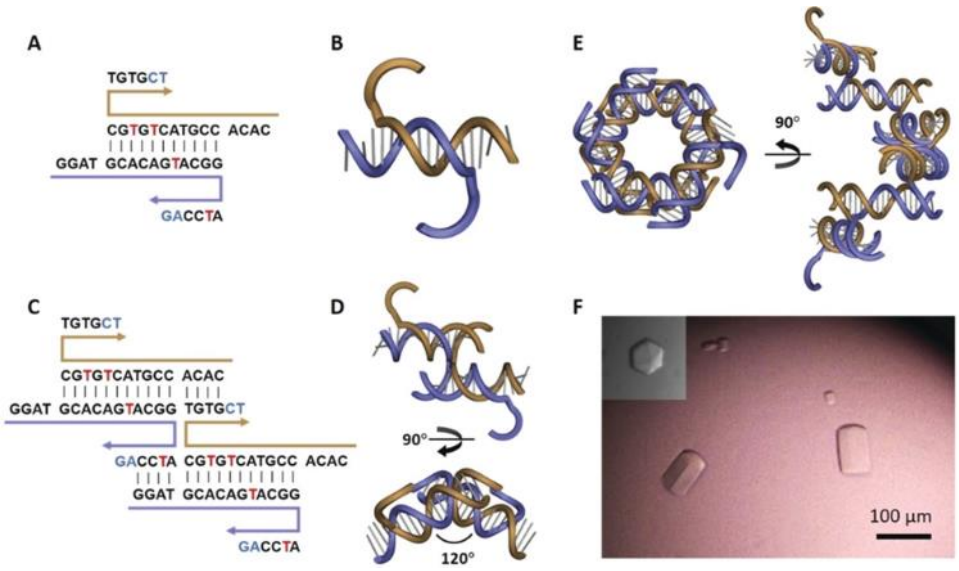

Figure 1-12 Schematic Design and Optical Images of 3D DNA Crystal with Six-fold Symmetry[18]

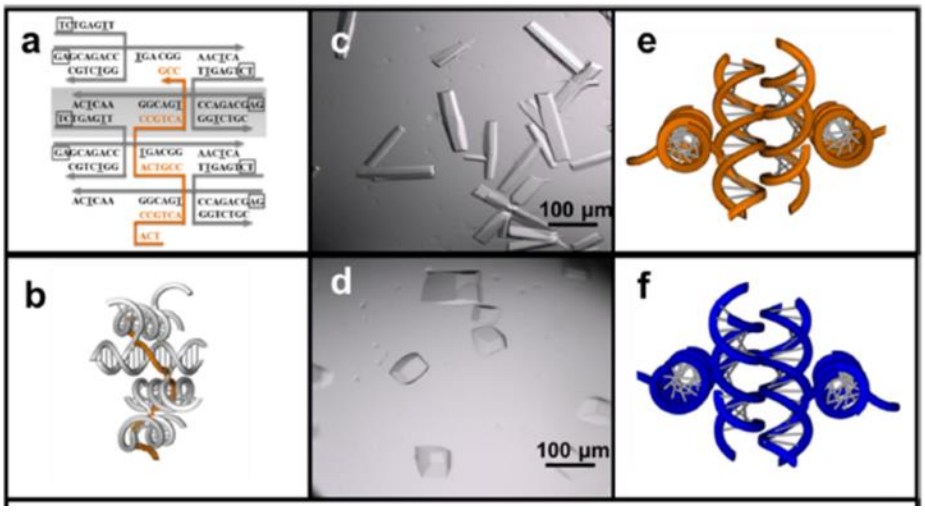

Figure 1-13 Schematic Design and Optical Images of 3D DNA Crystal with l-DNA and d-DNA[19]

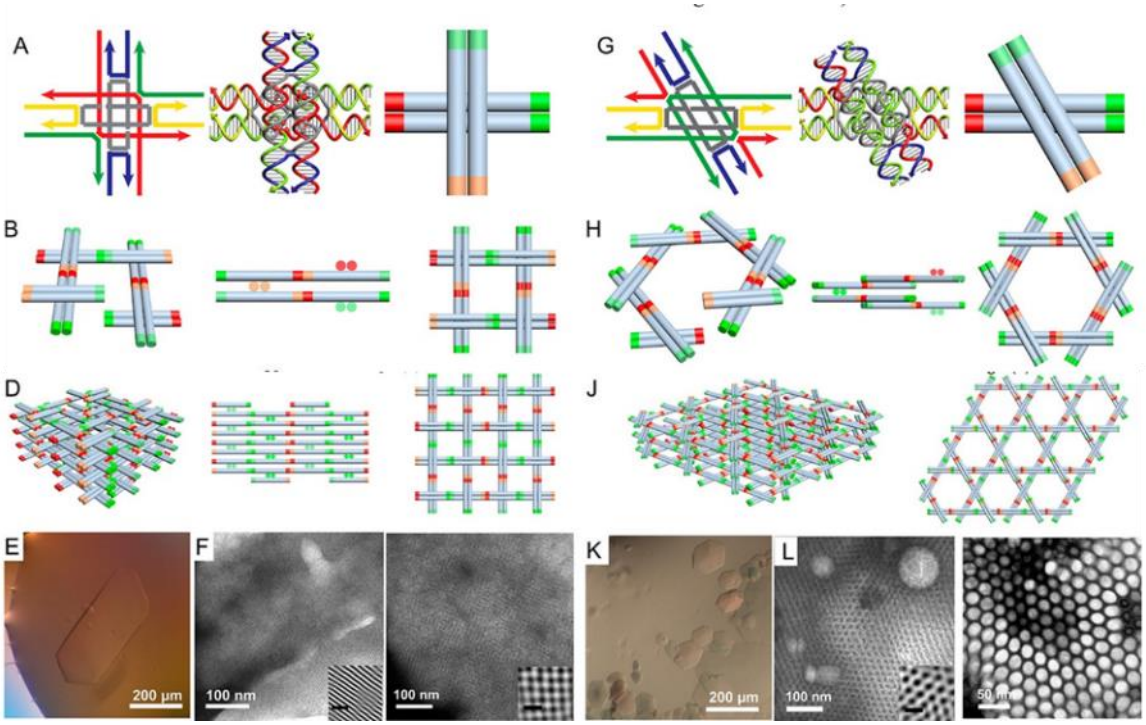

Figure 1-14 Schematic Design and Optical Images of 3D DNA Crystal from Layered-crossover Tiles[20]

DNA crystals introduced above were all assembled by Watson Crick base pairing. DNA crystals were also found to be assembled from non-canonical base pairings[21]. More recently, Michele's group discovered that DNA crystals could be assembled by hydrophobic interactions from flexible amphiphilic DNA stars (Figure 1-15)[22]. In this design, flexible DNA linkers were used to connect the micelles of cholesterol modified DNA into crystalline arrangements.

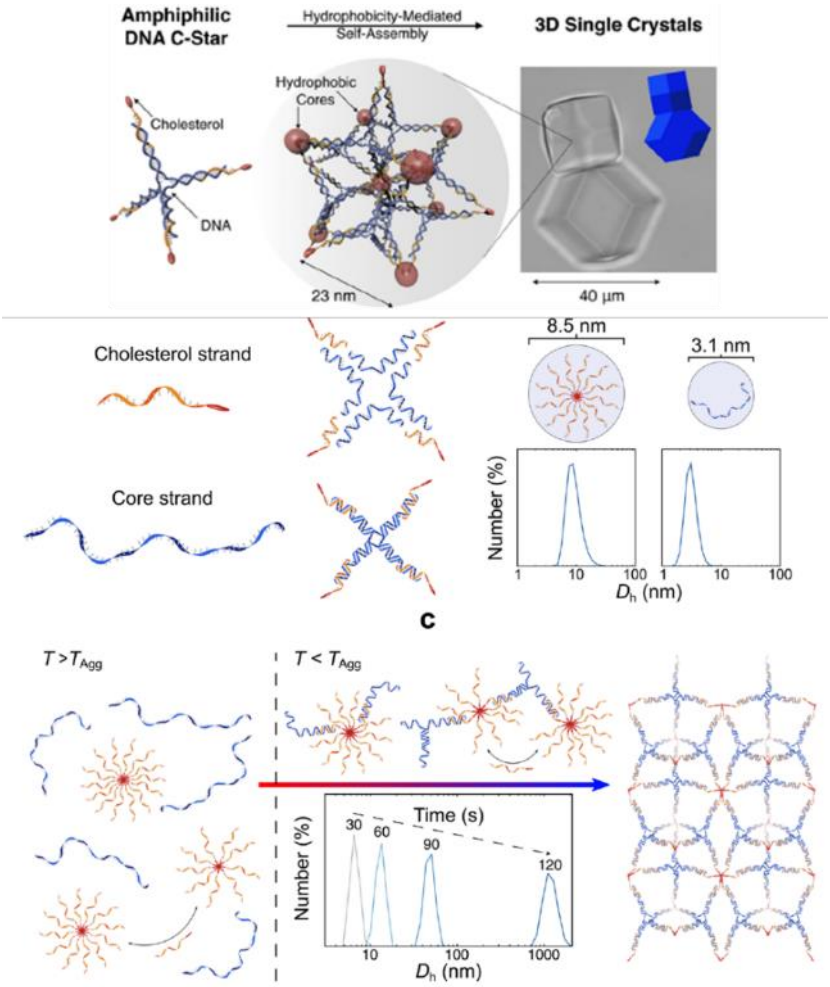

Figure 1-15 3D DNA Crystal Assembled from Amphiphilic DNA C-Stars[22]

1.2.2 Modulation of the Self-assembly of 3D DNA Crystal

With the successful design and construction of 3D DNA crystals, several different methods were developed to modulate the self-assembly process. Paukstelis's group achieved layer-by-layer assembly of DNA crystals (Figure 1-16)[23], which is also known as "macro-seeding" in crystallography. In the core-shell crystals obtained, guest molecules of fluorescence can be covalently attached on specific shell layers. The self-assembly kinetics on specific DNA crystal facets was also modulated by Paukstelis group[24] and our group[25] (Figure 1-17). "Poison" oligonucleotides were added during the crystallization process, which selectively passivated specific crystal contacts. We also reported that DNA crystals with such modulation experimentally achieved higher X-ray diffraction resolution.

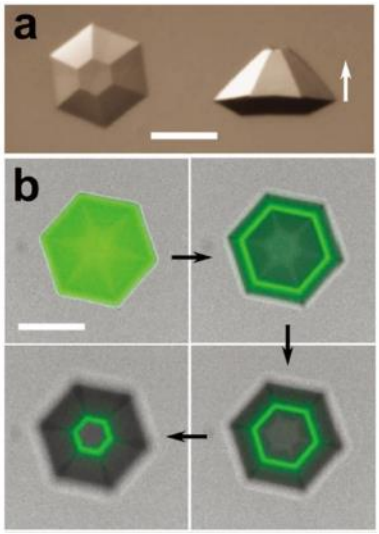

Figure 1-16 Core-shell Assembly of 3D DNA Crystal[23]

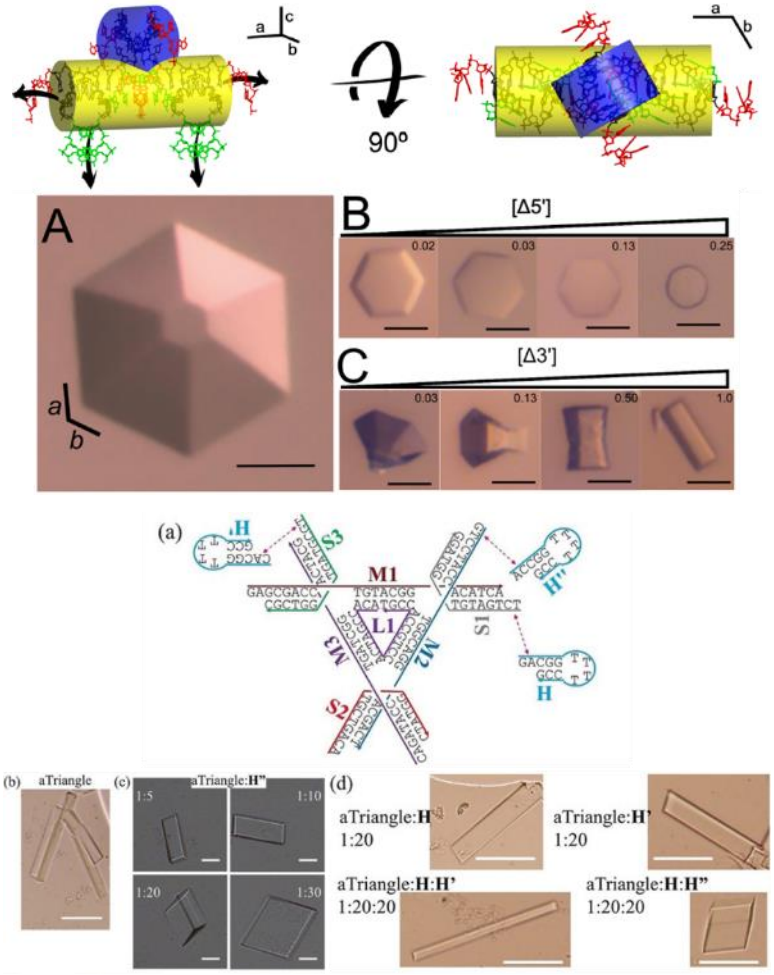

Figure 1-17 Modulation of the Crystallization Process of 3D DNA Crystal[24,25]

1.2.3 Stabilization of 3D DNA Crystals

One important goal for engineering 3D DNA crystals is to realize the precise 3D arrangement of molecules and nano-objects by using DNA as a scaffold. However, the development for such applications has been hindered by the stability of crystal scaffold. It is always hard to accommodate the crystallization buffer condition to the conditions where guest molecules are stable and functional. For example, in current crystallization buffers, inorganic nanoparticles aggregate, and enzymes lose function. To solve this problem, our group designed a triplex bundle around the interacting sticky ends at the crystal contacts. After the stabilization, the crystal can be stable in ionic strength of as low as 20 mM of $(NH_4)_2SO_4$ (Figure 1-18)[26]. Chemical cross-linking was also developed in Seeman's group by using psoralen modified DNA[27] and in Paukstelis's group by using DNA alkylating mustard[28] (Figure 1-19). These methods stabilized DNA crystals to endure temperatures of as high as around 30 °C.

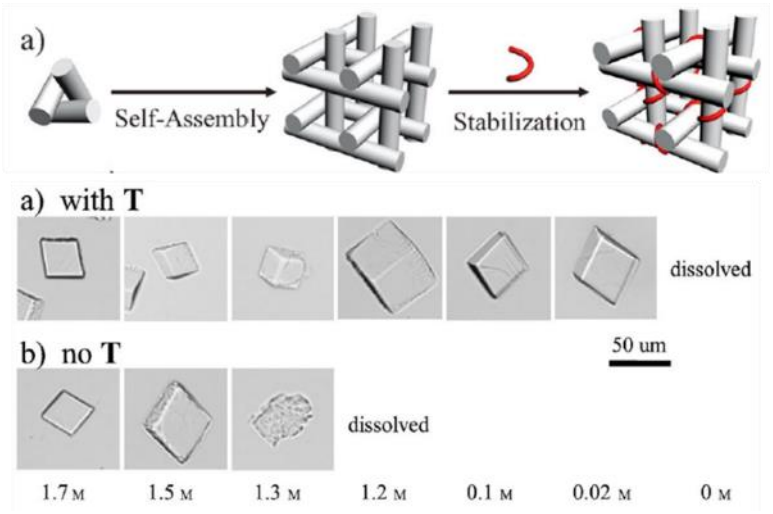

Figure 1-18 Stabilization of 3D DNA Triangle Crystal by Triplex Bundling[26]

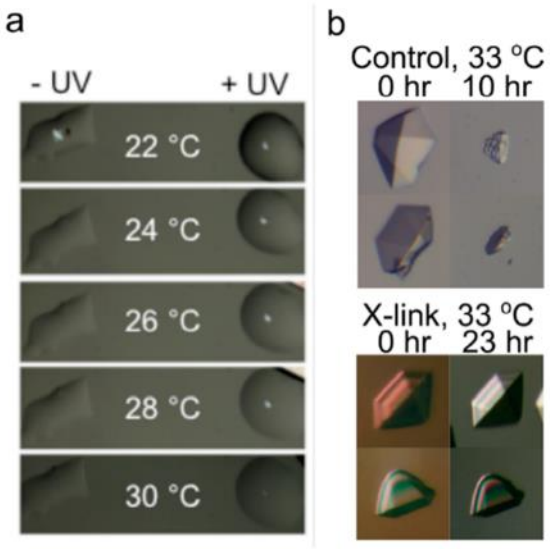

Figure 1-19 Enhancement of Thermostability of 3D DNA Crystal by Chemical Crosslinking[29]

1.3 Applications of Porous Macromolecular Crystals

In this section, we will review current applications developed for both protein crystals and DNA crystals. While they are both porous crystals assembled from macromolecules, current protein crystals were not rationally designed. Therefore, protein crystal scaffolds could not achieve as much control and variations in crystal parameters as in DNA crystals. However, the applications of protein crystals have been more developed as compared with DNA crystals, mostly because robust methods have been set up for a long time to stabilize protein crystals. Crosslinkers like glutaraldehyde have been widely used to make stable protein crystals[30]. In this case, we summarize the applications of protein crystals, and this can be the helpful inspiration of what applications well-stabilized DNA crystals could potentially achieve.

1.3.1 Applications of 3D Protein Crystals

Snow's group developed various arrangements of guest molecules in the crystal of CJ0 protein (Figure 1-20)[31–33]. CJ0 is a putative periplasmic polyisoprenoid-binding protein from *Campylobacter jejuni*. To find the crystals, they screened through the protein data bank (PDB) for crystals with large solvent channels. Then they selected the CJ0 crystal with 13 nm diameter pores running only in the vertical direction. They have successfully encapsulated gold nanoclusters and proteins inside crosslinked CJ0 crystal. The crystal's mammalian cytocompatibility was also evaluated for biotechnology and nanomedicine applications[34].

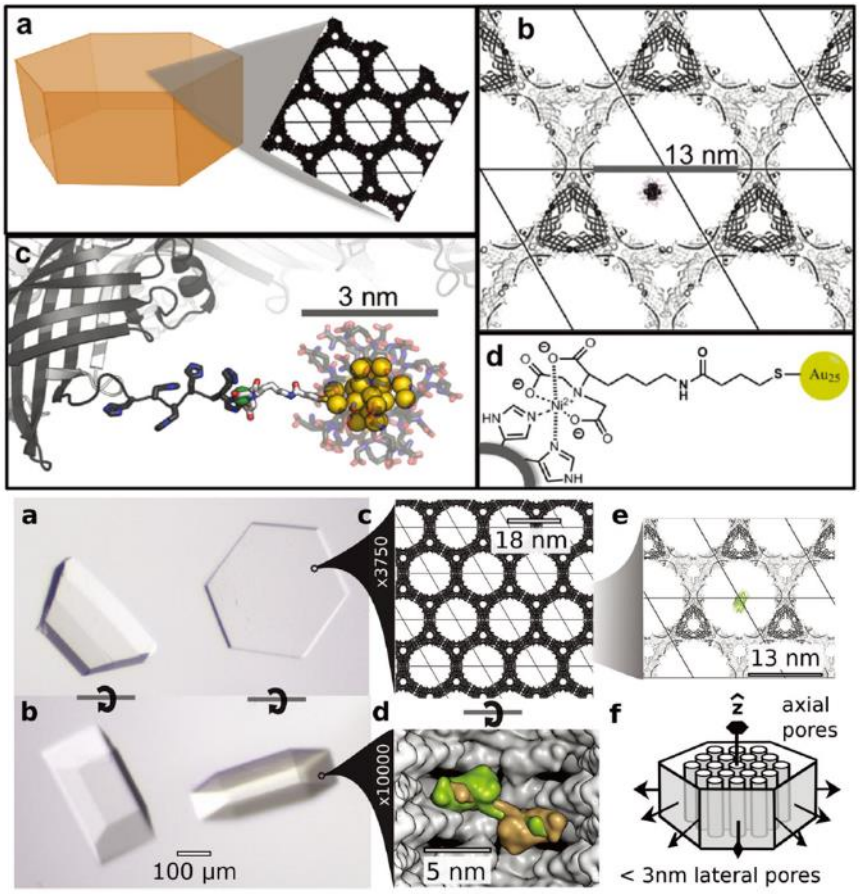

Figure 1-20 Au Nanoclusters and GFP Captured in Protein Crystals[31,32]

Besides scaffolding nano-objects, crosslinked protein crystals were also used to template material synthesis. Mann's group applied crosslinked lysozyme crystals to the synthesis of inorganic nanomaterials[35] and organic polymers[36] (Figure 1-21). Recently Tezcan's group demonstrated a hyper-expandable and self-healing crystal by fusing hydrogel inside the crystal of ferritin (Figure 1-22)[37]. Such protein crystal-hydrogel hybrid can recover their atomic-level periodicity even after rounds of reversible expansion.

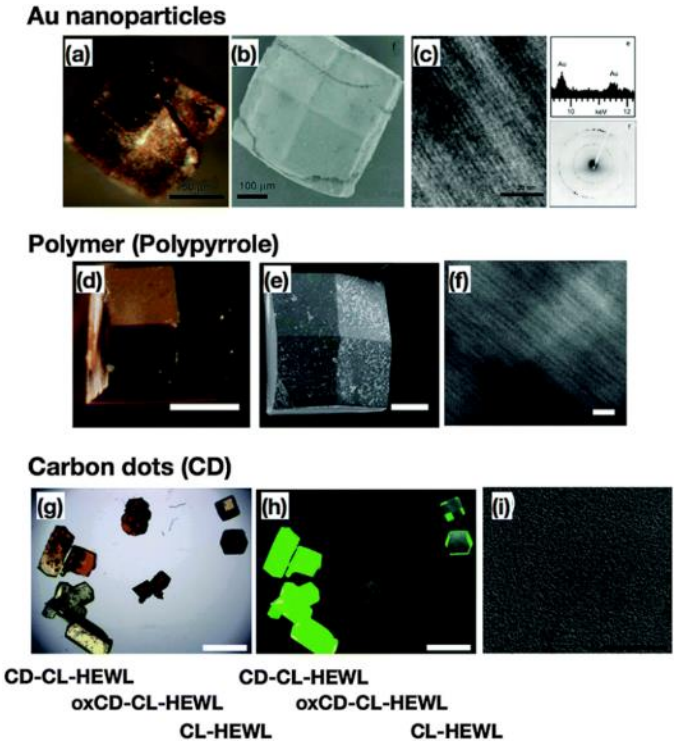

Figure 1-21 Crosslinked Lysozyme Crystals as a Template for Chemical Synthesis[38]

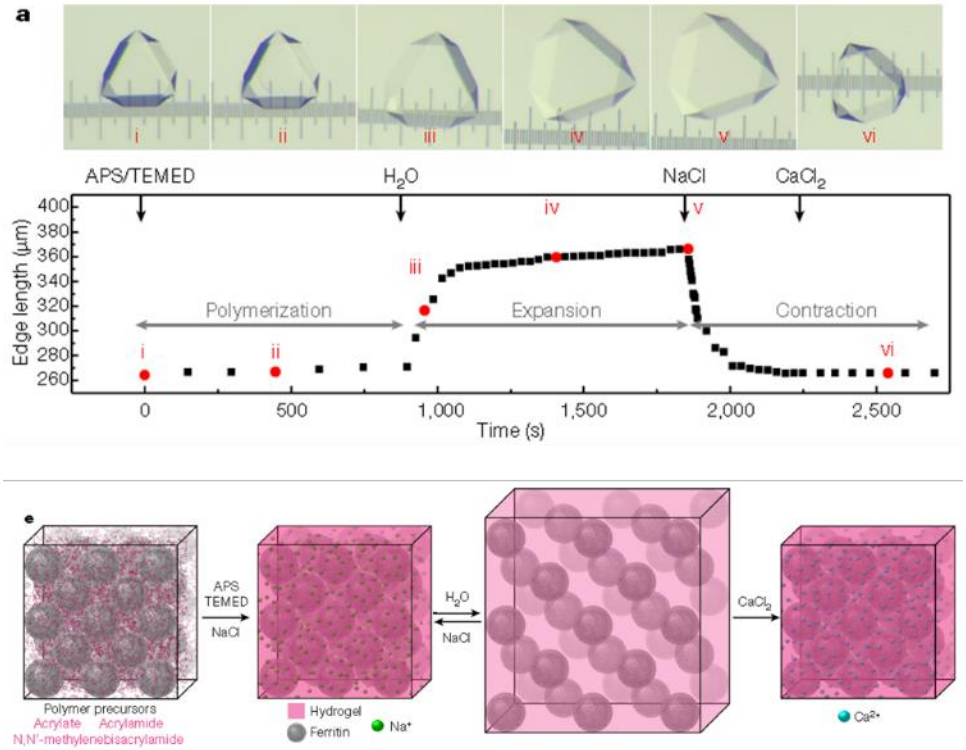

Figure 1-22 Hyperexpandable Crystal Prepared by Fusing Polymer Gel inside Ferritin Crystal[37]

1.3.2 Applications of 3D DNA Crystals

In 2014, Paukstelis's group reported the application of DNA crystal as a vehicle for biocatalysis (Figure 1-23)[39]. In the 9-nm-diameter solvent channels, RNase A was encapsulated and used to cleave a fluorescent substrate. In 2017, Seeman's group demonstrated that DNA strand displacement could happen inside DNA crystals (Figure 1-24)[40]. They further built such crystal into a three-state device of changing colors. They were also able to arrange organic semiconductors inside DNA crystal as a redox switch (Figure 1-25)[41]. Redox cycling within the crystal switch was characterized by Raman microscopy and directly visualized by the change of crystal color.

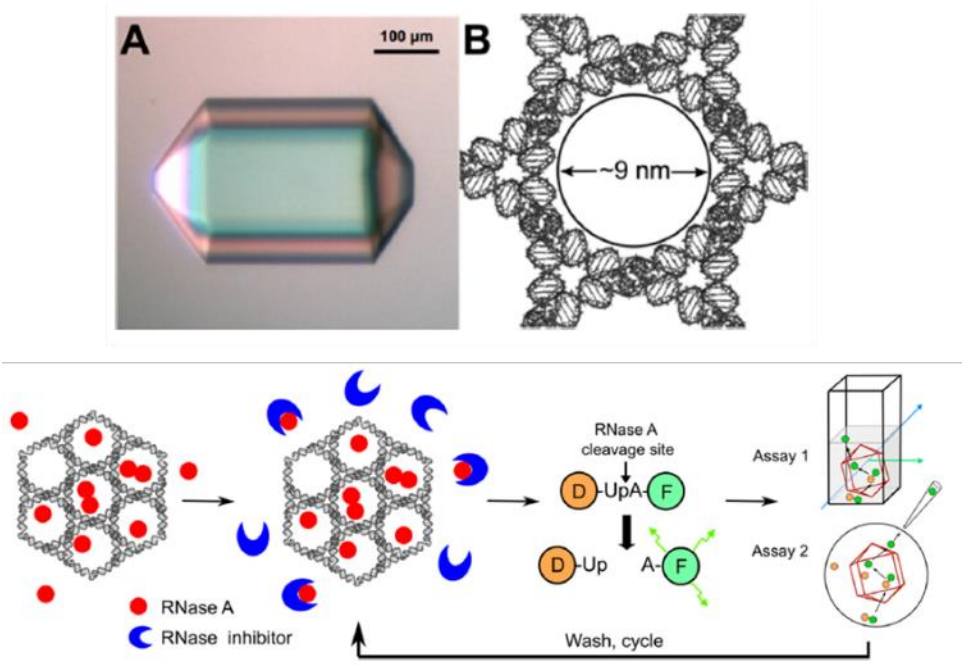

Figure 1-23 3D DNA Crystal as Vehicles for Biocatalysis[39]

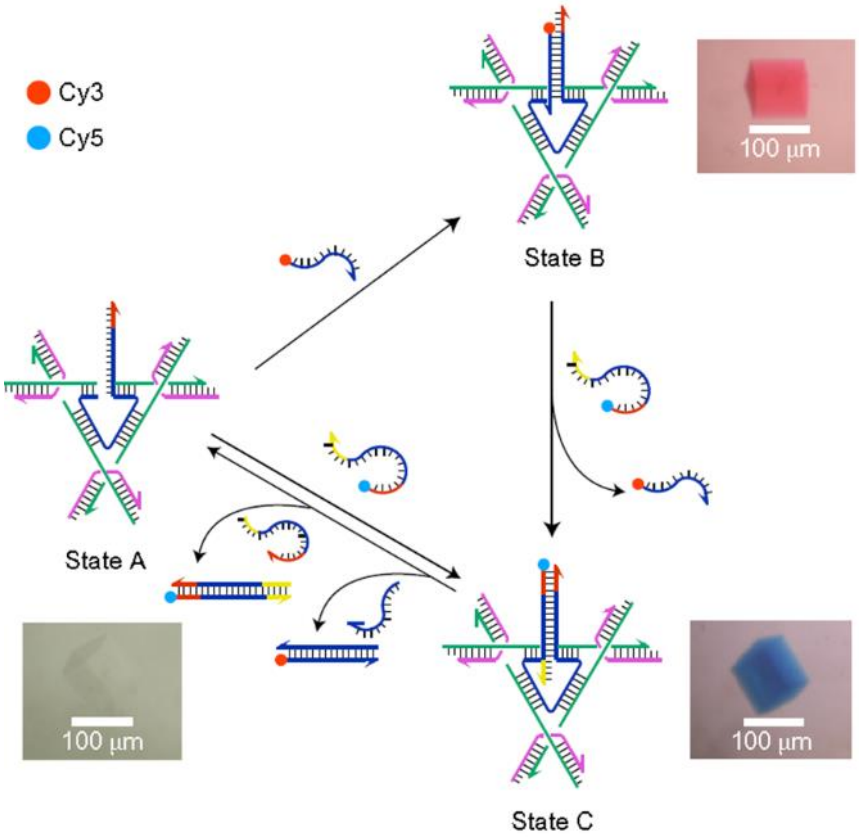

Figure 1-24 A Three-states Color DNA Crystals Device by Strand Displacement[40]

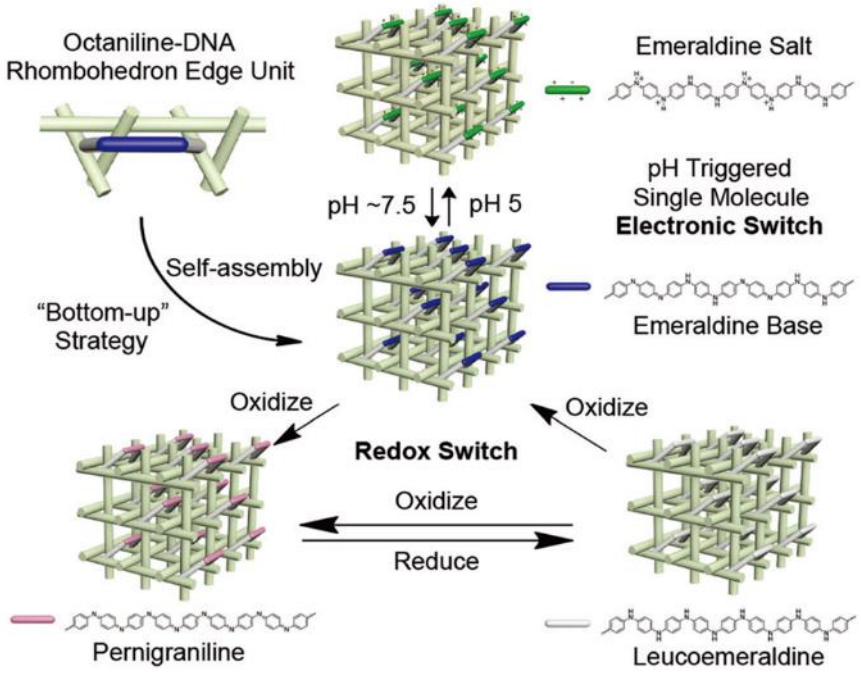

Figure 1-25 A Redox Switch by Organizing Semiconductors inside 3D DNA Crystal[41]

CHAPTER 2. POST-ASSEMBLY STABILIZATION OF ENGINEERED 3D DNA CRYSTALS BY ENZYMATIC LIGATION

2.1 Introduction

Engineered 3D DNA crystals have been proposed as promising platforms for arranging nano-objects into three-dimensional, macroscopic devices. However, the development of such applications has been hindered by the crystal stability. Like all macromolecular crystals, DNA crystals are fragile and very sensitive to solution conditions. For example, low ionic strength and elevated temperature can dissolve the self-assembled crystal. Though methods have been developed to stabilize the crystalline scaffold, current methods have lots of limitations. For example, the triplex bundling approach requires an acidic pH, while the chemical crosslink requires complex DNA modification, and can only increase the crystal stability up to ~ 30 °C. Here we developed a simple and highly efficient method to significantly increase the stability of engineered 3D crystals. We achieved the stabilization by post-assembly modification. In an enzymatic ligation reaction, we were able to convert the reversible, weak sticky-ended cohesions at crystal contacts into covalently linked, continuous DNA duplex at high yield throughout the crystal. The ligation yield was confirmed from the electrophoresis gel, and the crystal stability was tested against low ionic strength, high temperature, dehydration and organic solvents. Ligated crystals were also more mechanically robust. We then demonstrate examples showing how ligated DNA crystals can easily accommodate the functioning of enzyme and DNA aptamer.

2.2 Design and Scheme

Ligation is an essential step in molecular biology to create recombinant DNA, and it has been used in DNA nanotechnology to stabilize 2D DNA crystalline[6] and produce DNA hydrogels[54]. During ligation, the ends of DNA fragments are joined together by the formation of phosphodiester bonds between the 3'-hydroxyl of one DNA terminus with the 5'-phosphoryl of another. For engineered DNA crystals, a post-assembly ligation is designed to convert sticky ends at the crystal contacts into continuous covalent bonds (Figure 2-1). In this way, individual triangle motifs in the crystal are crosslinked in three dimensions, and the hydrogen-bonded network is converted into a covalently bonded network. After ligation, the crystal is expected to become much more robust.

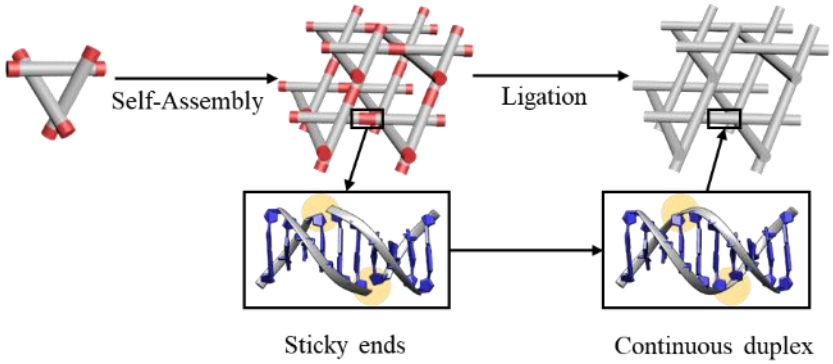

Figure 2-1 Schematic Drawing of Post-assembly Ligation for DNA Crystal

To achieve such an enzymatic reaction inside 3D DNA crystals, two problems need to be addressed. The first problem is to find an appropriate buffer condition. The buffer should have high enough ionic strength for native DNA crystals to be stable, and at the same time not inhibit the function of DNA ligase. The second one is the steric hindrance. For ligation to happen throughout the 3D crystal lattice, crystal pores need to be large enough for DNA ligase to diffuse in and bind on the sites to be ligated. For the investigation of these two problems, our work focused on two DNA tensegrity triangle designs of 3-turn edge length ($s\Delta^{3T}$) and 4-turn edge length ($s\Delta^{4T}$) (Figure 2-2).

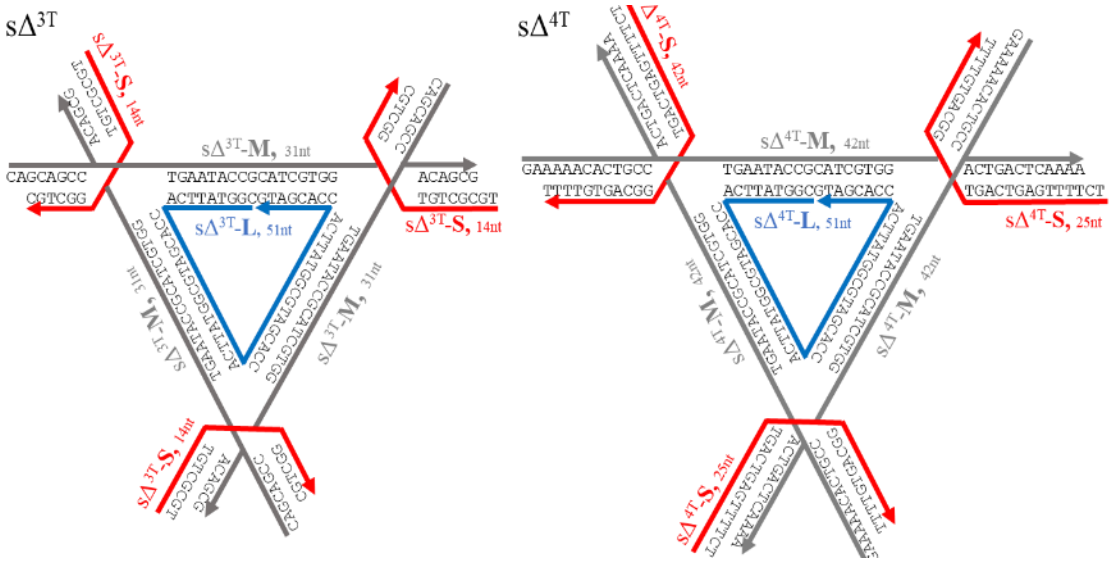

Figure 2-2 Schematic Design of DNA $s\Delta^{3T}$ and DNA $s\Delta^{4T}$

2.3 Material and Methods

2.3.1 DNA Oligonucleotides

All oligonucleotides were purchased from IDT and purified by 20% denaturing PAGE. Purified DNA strands were phosphorylated by T4 polynucleotide kinase (*New England Biolabs, Inc., NEB*) overnight (5 μL kinase (50 units) for every 4 nmol of DNA) in T4 DNA ligase reaction buffer (*New England Biolabs, Inc., NEB*). On the second day, the mixture was phenol extracted to remove kinase. Phosphorylated DNA strands were then ethanol precipitated from the solution. The pellet was washed and redissolved in water. Then they were desalted by home-made spin columns of G25 matrix (*Illustra, Sephadex G-25 Superfine DNA Grade*).

sΔ^{3T}-L/ sΔ^{4T}-L, 51 nt: 5'-CGGTATTCACCACGATGCGGTATTCACCACGATGCGGTATTCACCACGATG-3'

sΔ^{3T}-M, 31 nt: 5'-CAGCAGCCTGAATACCGCATCGTGGACAGCG-3'

sΔ^{3T}-S, 14 nt: 5'-TGCGCTGTGGCTGC-3'

sΔ^{4T}-M, 42 nt: 5'-GAAAAACACTGCCTGAATACCGCATCGTGGACTGACTCAAAA-3'

sΔ^{4T}-M, 25 nt: 5'- TCTTTTGAGTCAGTGGCAGTGTTTT-3'

sΔ^{5T}-L, 84 nt: 5'-TAGATGCGGTCAGTAATTCACCACGAGCTAGATGCGGTCAGTAATTCACCACGAGCTAGATGCGGTCAGTAATTCACCACGAGC-3'

sΔ^{5T}-M, 52 nt: 5'-GAAAAACACTGCCTGAATTACTGACCGCATCTAGCTCGTGGACTGACTCAAA-3'

sΔ^{5T}-S, 24 nt: 5'- TCTTTGAGTCAGTGGCAGTGTTTT-3'

sΔ^{8T}-L, 84 nt: 5'- CGGTCAGTAATTCACCACGAGCTAGATGCGGTCAGTAATTCACCACGAGCTAGATGCGGTCAGTAATTCACCACGAGCTAGATG-3'

sΔ^{8T}-L-6H7, 127 nt: 5'-GCTATGGGTGGTCTGGTTGGGATTGGCCCCGGGAGCTGGCtttCGGTCAGTAATTCACCACGAGCTAGATGCGGTCAGTAATTCACCACGAGCTAGATGCGGTCAGTAATTCACCACGAGCTAGATG-3'

sΔ^{8T}-M, 84 nt: 5'-GAGGAGCAAACTTCTAACAGCATACTGCCTGAATTACTGACCGCATCTAGCTCGTGGACTGATCGACCTCCTTGAAAGACAGAG-3'

sΔ^{8T}-S, 56 nt: 5'- CTCCTCTGTCTTTCAAGGAGGTCGATCAGTGGCAGTATGCTGTTAGAAGTTTGCTC-3'

aΔ^{4T}-L, 51 nt: 5'-GTAATCGCACCGTCAACTATTGGTCACCTGAACGAGTTCTCCACCAAGATC-3'

aΔ^{4T}-L-6H7, 92 nt: 5'-GCTATGGGTGGTCTGGTTGGGATTGGCCCCGGGAGCTGGCt GTAATCGCACCGTCAACTATTGGTCACCTGAACGAGTTCTCCACCAA GATC-3'
aΔ^{4T}-M1, 42 nt: 5'-ACAAAACACTGCCTGCGATTACGATCTTGGACGAAGCGTCTG-3'
aΔ^{4T}-M2, 42 nt: 5'-GACAGTGACAGCCTGACCAATAGTTGACGGACTGACTCAAAA-3'
aΔ^{4T}-M3, 42 nt: 5'-GGTGCAAACGACCTGGAGAACTCGTTCAGGACCTACTGCTAC-3'
aΔ^{4T}-S1, 25 nt: 5'-TCTTTTGAGTCAGTGGCAGTGTTTT-3'
aΔ^{4T}-S2, 25 nt: 5'-CCGTAGCAGTAGGTGGCTGTCACTG-3'
aΔ^{4T}-S3, 25 nt: 5'-GTCAGACGCTTCGT GGTCGTTTGCA-3'

2.3.2 Crystallization of DNA Triangle Crystals

For the crystallization of sΔ^{4T}, DNA strands were combined at designed ratio of L: M: S= 1: 3: 3 in 0.5×TAE/Mg^{2+} buffer (1×TAE/Mg^{2+} buffer contains 40 mM Tris base, 20 mM acetic acid, 2 mM EDTA and 12.5 mM magnesium acetate, pH 8) by slowly cooling the DNA solution from 95 ºC to 22 ºC in 2 hours. The final triangle motif concentration is 2 μM. 5 μL of assembled DNA triangle solution was incubated against 600 μL of 5×TAE/Mg^{2+} solution in a hanging-drop setup at 22 ℃ for 3 days to a week. Rhombohedral shape crystals of 50-200 μm size appeared in the drops. For different designs, different drop buffer and reservoir buffer were used to suit the best crystallization kinetics. For sΔ^{3T}, the drop buffer and reservoir buffer were 0.5×TAE/Mg^{2+} and 10×TAE/Mg^{2+}; For sΔ^{5T}, they were 1×TAE/Mg^{2+} and 5×TAE/Mg^{2+}; For sΔ^{8T} and aΔ^{4T}, 0.2×TAE/Mg^{2+} and 3×TAE/Mg^{2+} were used. The crystal size and morphology were examined by optical microscopy (OLYMPUS, BX51).

2.3.3 Native PAGE Analysis

Native PAGE containing 6% polyacrylamide (19:1 acrylamide/ bisacrylamide) was run in Hoefer SE 600 electrophoresis unit at 250 V at room temperature in 1×TAE/Mg^{2+} buffer for 2-3 hours. After electrophoresis, the gels were stained by stains-all (*Sigma*), destained and scanned by an office HP scanner.

2.3.4 Ligation of DNA Triangle Crystals

Crystals were washed twice by 5×TAE/Mg^{2+} buffer and then incubated overnight in the freshly prepared ligation mixture. The mixture contains 1 mM ATP and 80 units/μL T4 DNA

ligase in 5×TAE/Mg^{2+}. After incubation, the crystals were extensively washed and stored in 5×TAE/Mg^{2+} buffer. For 8-turn crystals, 2.5×TAE/Mg^{2+} was used instead for 5×TAE/Mg^{2+}.

2.3.5 Denaturing PAGE Analysis

Gels contained 20% polyacrylamide (19:1 acrylamide/ bisacrylamide) and 8.3 M urea were run at 55°C. The running buffer 1×TBE consisted of 89 mM Tris base, 89 mM boric acid, and 2 mM EDTA, pH 8.0. Gels were run in Hoefer SE 600 electrophoresis unit at 600 V (constant voltage). For sample preparation, ligated crystals from 5 crystal drops were washed by 5×TAE/Mg^{2+} and transferred to 40 μL of formamide. The crystals completed dissolved in formamide. Samples were heated at 95 °C for 5 mins before loading into the denaturing gel.

2.3.6 X-ray Diffraction

Crystals were transferred by cryoloops into a drop containing the same crystallization buffer supplemented with 30% glycerol, and cryocooled by liquid nitrogen. Diffraction data were collected at 1.54 Å on a Rigaku RU-H2R rotating anode X-ray machine at Purdue University (the detector distance was set as 200 mm). All the data were indexed and refined using HKL2000[47] to determine the unit cell parameters.

2.3.7 UV Spectrophotometer Measurement of Crystal Melting

Six to ten ligate crystals were washed by 0.2×TAE/Mg^{2+} and transferred into a 100 μL cuvette. The cuvette was set for 30 mins to let the crystals settle down. Then the absorbance was monitored when the cuvette was heating up from room temperature to 85 °C, with temperature increasing 1°C per minute. To give dissolved crystal portions more time to diffuse inside the cuvette, the temperature was held for one hour at 37°C, 50 °C, 65 °C, 70 °C, 75 °C and 80 °C during the elevation process.

2.3.8 Biocatalysis by HRP Encapsulated in DNA Crystal

Ligated DNA crystals were incubated with ~20 mg/mL HRP in 0.1 M KH_2PO_4, pH 6 for two days to a week at 4 °C, and then used to catalyze the reaction between ABTS and peroxide. The crystal surface was blocked by polylysine to eliminate enzyme leakage by incubating in 5 μg/mL polylysine, 0.1 M KH_2PO_4, pH 5 for 1 hour, and washed by incubating overnight in 0.1 M KH_2PO_4, pH 5 before the catalysis reaction. The substrate mixture contained 5 mg/mL ABTS and

0.01% H_2O_2 in 0.1 M KH_2PO_4, pH 5, and was freshly prepared every day. The catalysis reaction was performed either in 5 µL drop for microscope observation or in 100 µL solution for spectrophotometer measurement at 414 nm. The crystal was transferred by cryoloop into the drop or the cuvette for reaction. For spectrophotometer measurement, the solution in the cuvette was pipetted to mix evenly before each data point was taken.

2.3.9 Encapsulation of His-tag Proteins in DNA Crystal

Ligated DNA crystal with 6H7 aptamer was washed repeatedly by PBS buffer and incubated in 5 µL 3.7 µM of 27 kD His tagged GFP or 76 kD His tagged GFP-deaminase in PBS buffer for encapsulation. The encapsulation process was examined by fluorescence microscopy (OLYMPUS, BX51).

2.4 Results and Discussion

2.4.1 Steric Hinderance and Buffer Condition for Successful Ligation

DNA tensegrity triangles of $s\Delta^{3T}$ and $s\Delta^{4T}$ were assembled and checked by native PAGE analysis at room temperature. Both triangle motifs were successfully assembled at high yield (Figure 2-3, Figure 2-4). For the first problem of finding a proper buffer condition, we found that although high concentration of monovalent cation (for example, 200 mM NaCl) inhibits ligase function, T4 DNA ligase showed no decrease in enzymatic activity at a high Mg^{2+}concentration (Figure 2-5). In the solution ligation of $s\Delta^{4T}$ triangles, high ligation yield was achieved for Mg^{2+} concentration ranging from 5 mM to 100 mM of Mg^{2+}. In crystallization screening, we also found that TAE/Mg^{2+} buffer was optimal for the crystallization of DNA tensegrity triangles. Therefore, the buffer accommodation problem was solved by choosing the TAE/Mg^{2+} buffer for both DNA triangle crystallization and post-assembly ligation.

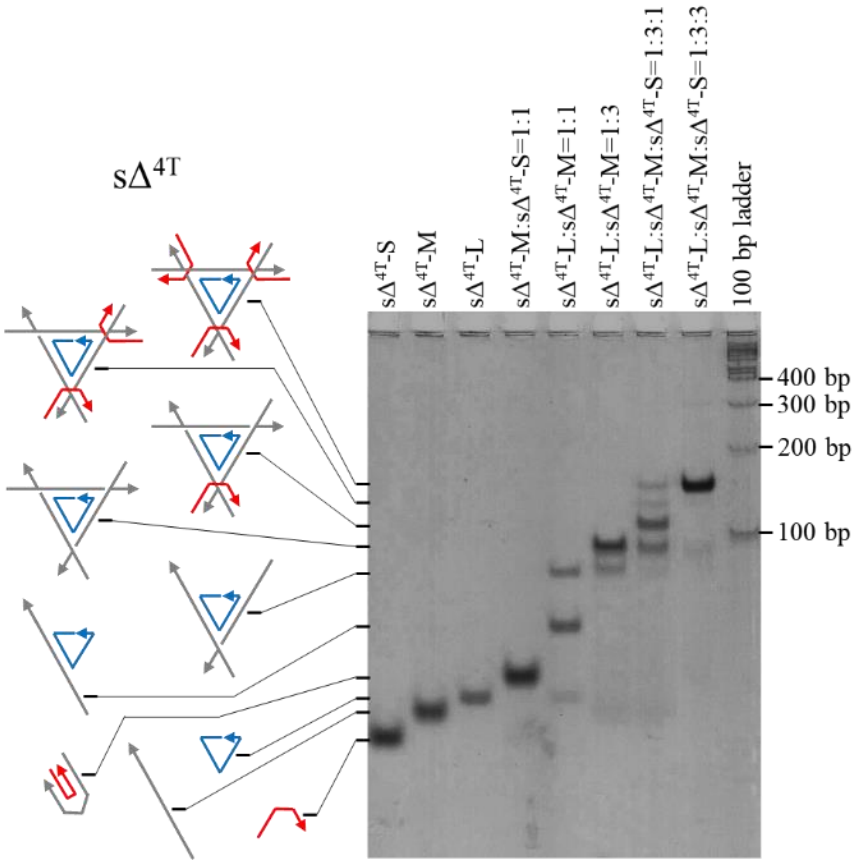

Figure 2-3 Native PAGE (6%) Analysis of DNA sΔ^{4T} Motif

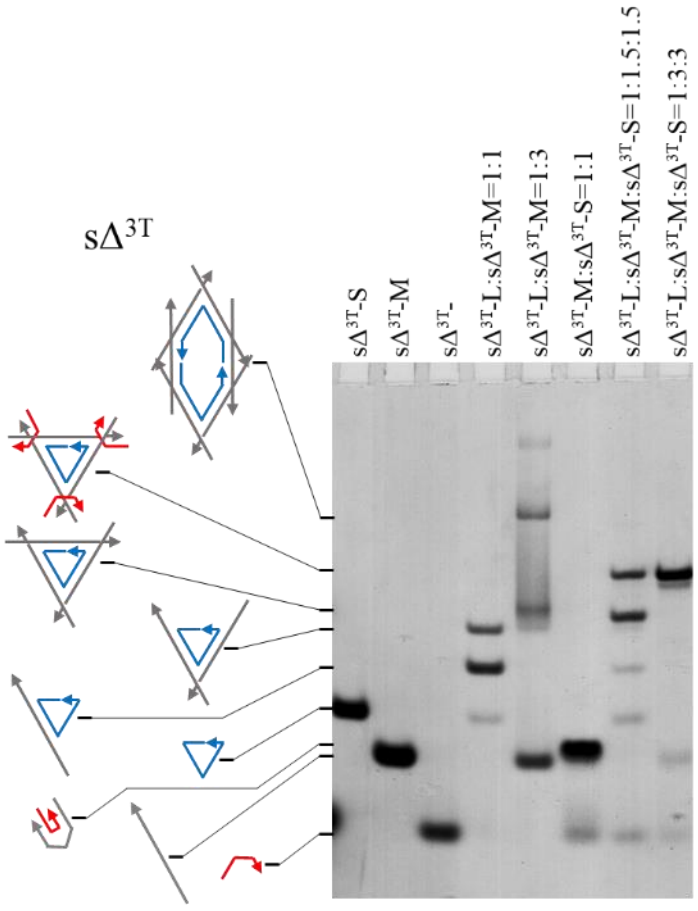

Figure 2-4 Native PAGE (6%) Analysis of DNA $s\Delta^{3T}$ Motif

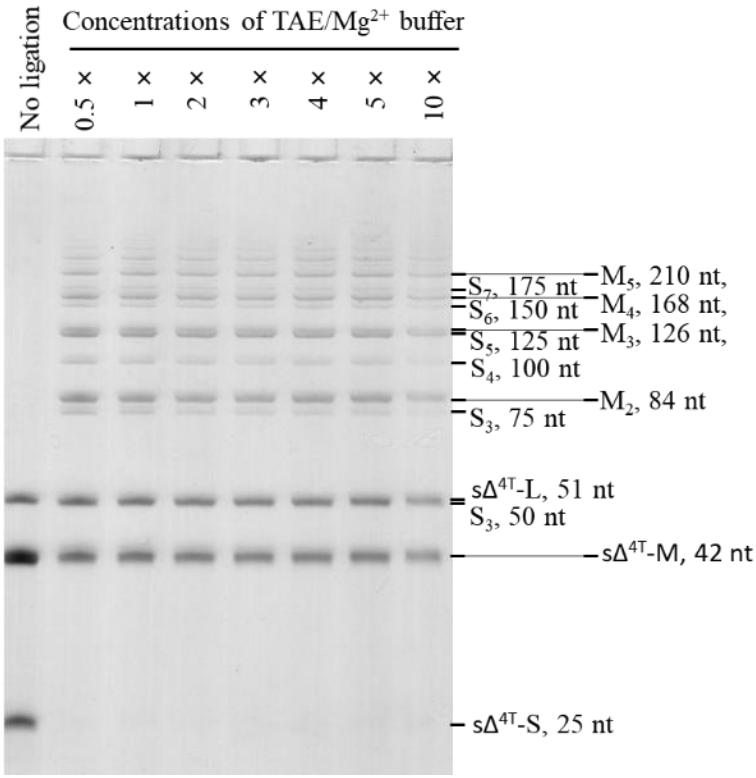

Figure 2-5 Denaturing PAGE (20%) Analysis for T4 DNA Ligase Activity in Different Concentrations of TAE/Mg^{2+} Buffer.

To solve the problem of steric hindrance for ligation inside DNA crystal lattice, we modeled the relative size between DNA crystal pores and the T4 DNA ligase (Figure 2-6). The B-form DNA duplex in the crystal was represented as 2 nm-diameter rigid rods, and the rods were arranged into the crystal scaffold according to the crystallographic symmetry data from X-ray diffraction. T4 DNA ligase has a molecular weight of 55.3 kD, and it contains 487 aa. Since no crystal structure was known for T4 DNA ligase, we simplified the ligase as a sphere with 5.4 nm diameter. By visually comparing the rod model and the sphere, the triangle motif needs to be at least three helical turns in edge length to fit the ligase.

DNA triangles $s\Delta^{3T}$ and $s\Delta^{4T}$ were crystallized in TAE/Mg^{2+} buffer to test the ligation efficiency inside the crystal lattice (Figure 2-7). The crystals were ligated overnight, dissolved in formamide, and then characterized by denaturing PAGE analysis. From the gel, we observed low ligation yield for $s\Delta^{3T}$ crystals, but $s\Delta^{4T}$ crystals were found to be ligated at high yield with a series of oligomers up to high molecular weight. These results indicate that DNA tensegrity triangle with

an edge length of 4 helical turns of DNA is the smallest DNA triangle design which enables ligation inside DNA crystal lattice.

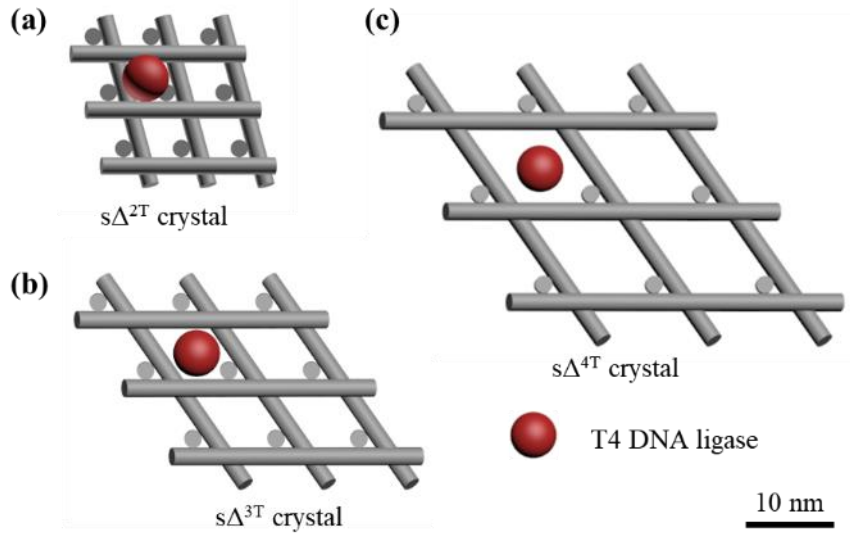

Figure 2-6 Size Comparison between DNA Crystal Pore Aperture and T4 DNA Ligase

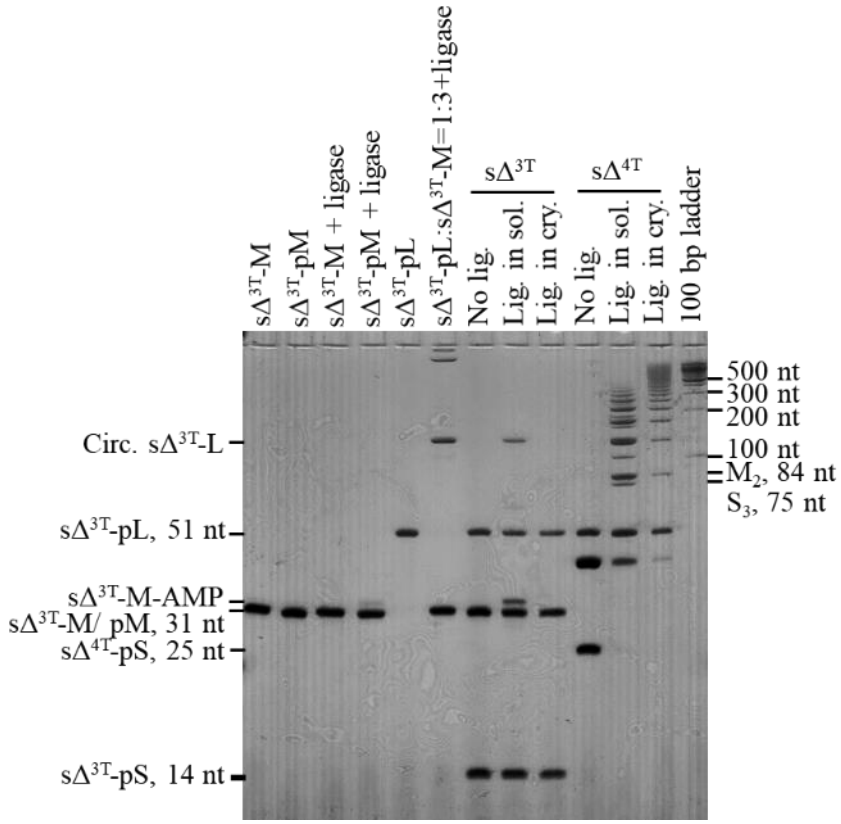

Figure 2-7 Denaturing PAGE (20%) for Ligation of DNA $s\Delta^{3T}$ and $s\Delta^{4T}$ in Solution and in Crystal.

We further characterized the ligation yield of each composing strand in the $s\Delta^{4T}$ crystal. To ligate only one identity of strand inside the crystal, only the selected DNA strand was phosphorylated before the crystal self-assembly. Note here we also noticed that the 5'-phosphorylation at the crystal sticky ends could significantly change the crystallization kinetics, and this was further investigated in more details in the last chapter. All these $s\Delta^{4T}$ triangles with selective phosphorylation were crystallized successfully (Figure 2-8). In the denaturing gel (Figure 2-9), we can observe and identify the ligated oligomers from strand M and strand S. Both M and S strands were ligated at high yield, with 100% of S strand and 82% of M strand linked into oligomers. Minimal ligation was observed for the central strand L, which is probably hindered by the close distance between junctions along DNA triangle edge.

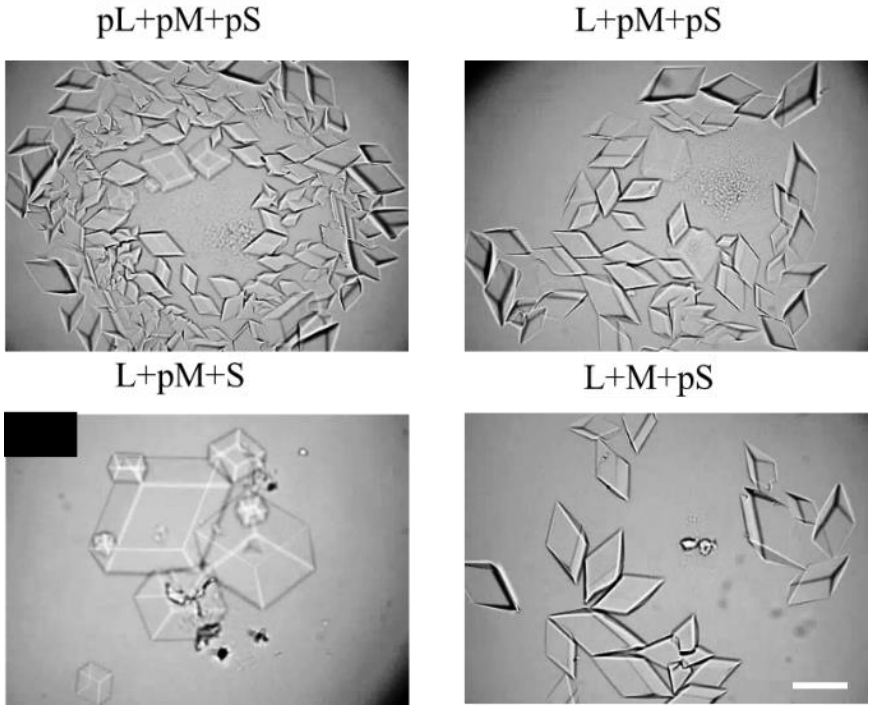

Figure 2-8 Optical Images of Different DNA $s\Delta^{4T}$ Crystal. Scale bar: 100 μm.

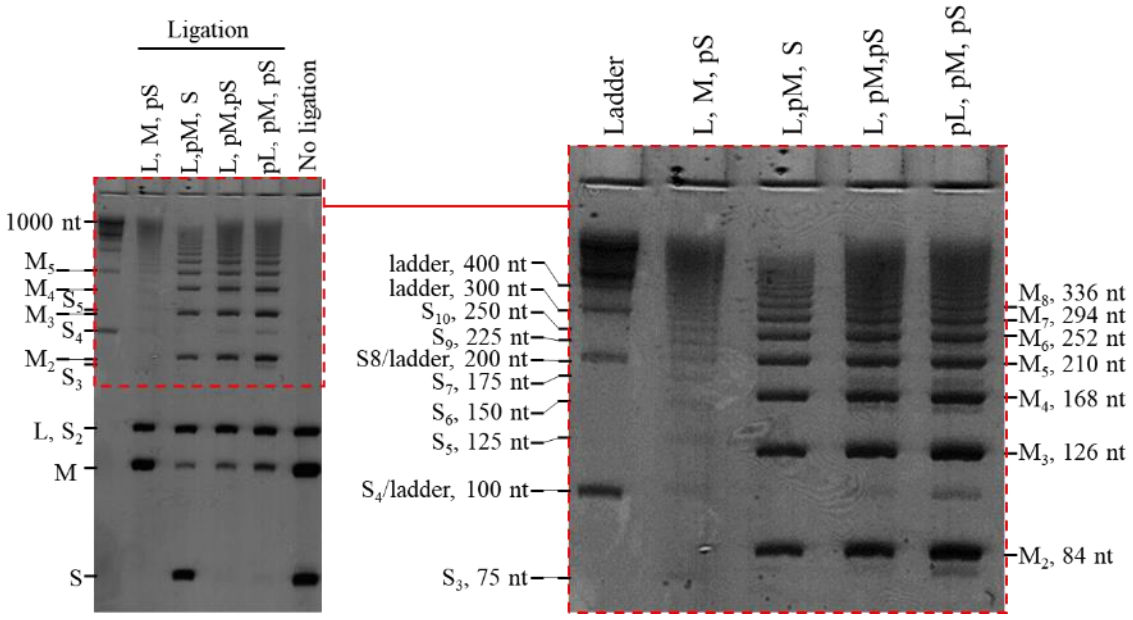

Figure 2-9 Denaturing PAGE (20%) for Ligation of Different Combinations of DNA $s\Delta^{4T}$ in Crystal.

We further found that with an elongated distance between the junctions, the central strand can also be ligated with ~100% yield in a 5-turn edge length triangle $s\Delta^{5T}$ (Figure 2-10).

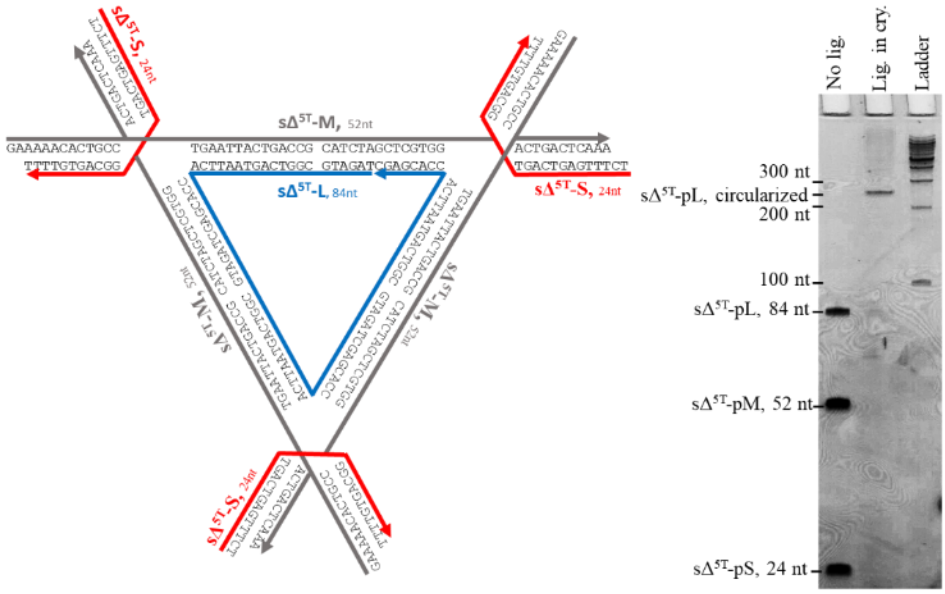

Figure 2-10 Schematic Design of DNA $s\Delta^{5T}$ and Denaturing PAGE (20%) for Ligation Yield

2.4.2 Investigation of Crystal Stability and Mechanical Strength after Ligation

After post-assembly ligation, DNA $s\Delta^{4T}$ crystals had a significant enhancement in their stability against low ionic strength and high temperature. Ligated crystal survived for more than 42 days after transferred into pure water (Figure 2-11, Figure 2-12). At the same time, crystal without ligation fully dissolved in 10 mM Mg^{2+} within one day. Later in X-ray characterization, we proved that ligated crystal maintained their morphology and crystallinity even after excessive washes by water. However, after incubation in 100 mM EDTA to completely strip Mg^{2+}, ligated crystal fully dissolved shortly after transferring into water. These results demonstrated that the trace amount of Mg^{2+} bound on the ligated crystals, which did not simply dissociate by washing, sustain the crystal stability. Similar stabilization by trace amount of Mg^{2+} was also reported for DNA origami structures[42]. In the presence of 2 mM Mg^{2+}, the ligated crystal can endure 65 °C for 16 hours (Figure 2-11), which is a much higher temperature than previously achieved 33 °C. In pure water, ligated crystal dissolved within 1 hour of incubation at 50 °C. The melting of ligated crystals at different ionic strength was also monitored by UV spectroscopy (Figure 2-13). The melting temperatures may be overestimated because of the lag of diffusion of dissolved DNA from the bottom of the cuvette to the light path.

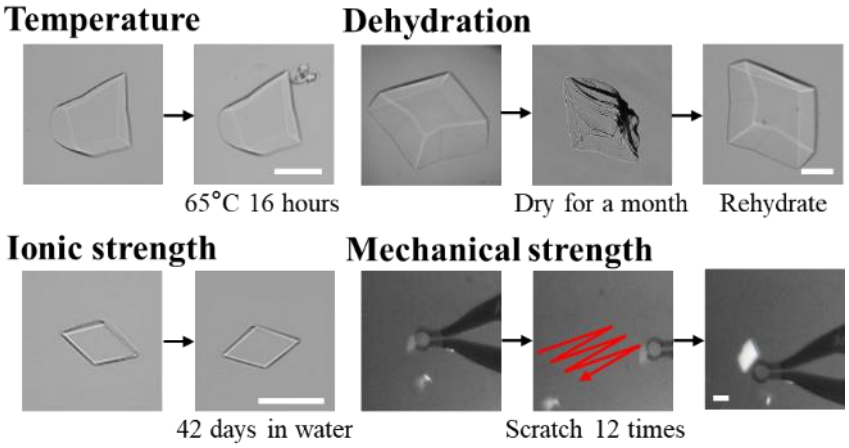

Figure 2-11 Stability Tests for Ligated DNA $s\Delta^{4T}$ Crystals. Scale bar: 100 μm.

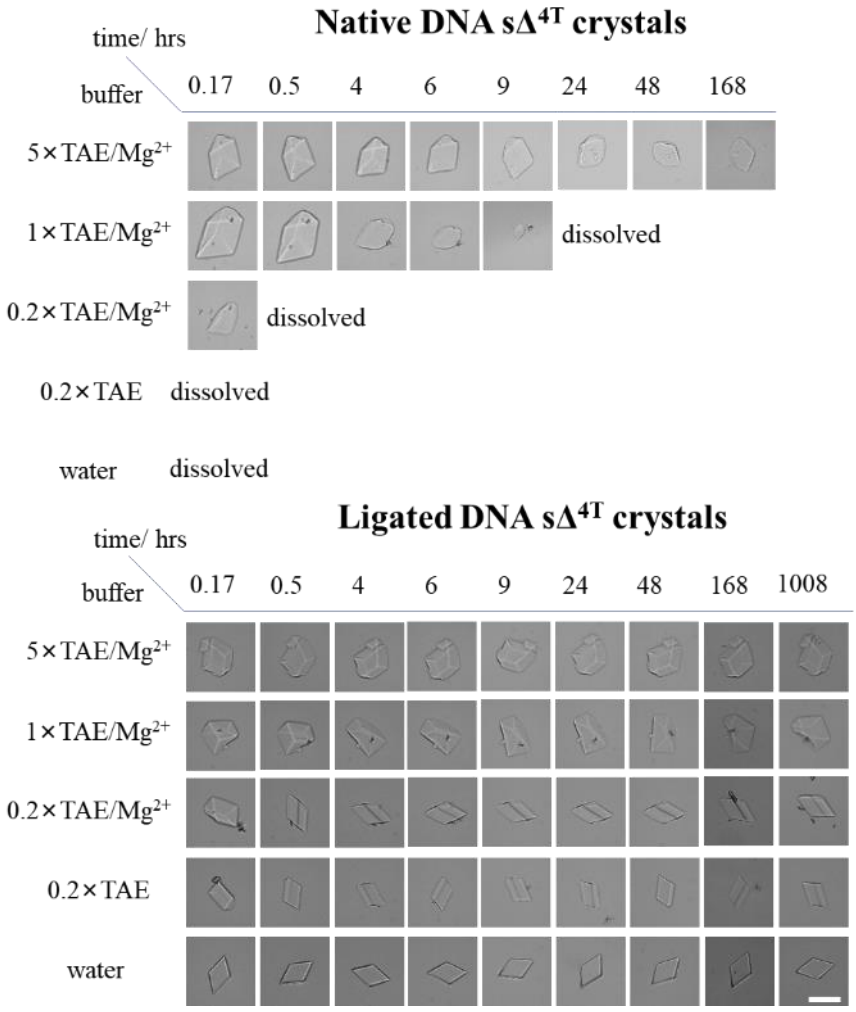

Figure 2-12 Stability of Ligated DNA $s\Delta^{4T}$ Crystals Against Ionic Strength. Scale bar: 100 μm.

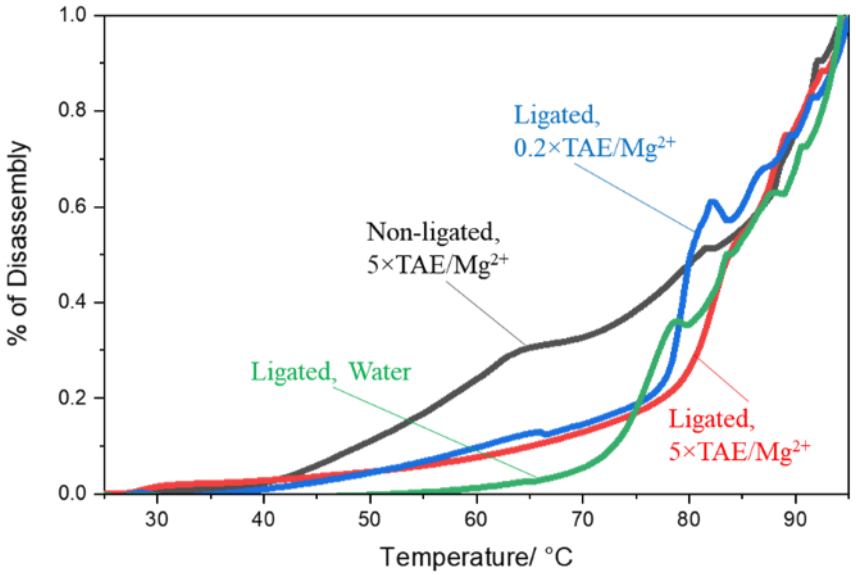

Figure 2-13 Stability of Ligated DNA $s\Delta^{4T}$ Crystals Against Elevated Temperature

Ligated DNA $s\Delta^{4T}$ crystals also showed increased stability against dehydration, organic solvents and enzymatic degradation. While native DNA crystals cracked and fell apart if transferred into air, ligated crystals maintained their crystal morphology and crystallinity when dried and rehydrated. After being excessively washed with water, the ligated crystal was dried in air. The crystal collapsed during drying and quickly expanded to its original shape when rehydrated by water. The dehydration could be extended to at least a month at room temperature (Figure 2-11), and the dehydration-rehydration can be exerted on the ligated DNA crystal for more than five cycles without any change in crystal morphology (Figure 2-15). Such property will be very advantageous for the storage and transportation of DNA crystal materials. Further X-ray experiments proved that ligated crystals maintained most crystallinity after two cycles of dry-rehydrate-freeze-thaw (Figure 2-15). Ligated and dehydrated DNA crystals were stable in organic solvents. After incubation in organic solvents of various polarity and rehydration with water, crystals went back to their original morphologies (Figure 2-16). So far formamide is the only pure solvent to fully dissolve ligated DNA crystals. The stability of ligated crystals in solvent mixture was also investigated, and crystal dissolved in the PBS mixture with DMF and DMSO (Figure 2-17). As to enzymatic degradation, the ligated crystal was degraded by DNase I at 0.1 unit/μL from the periphery and disappeared after 20 mins of room temperature incubation. However, ligated

crystals are stable in 100% FBS at room temperature for a week (Figure 2-18). The stability in FBS medium will enable further development of ligated DNA crystals as vehicles for drug delivery.

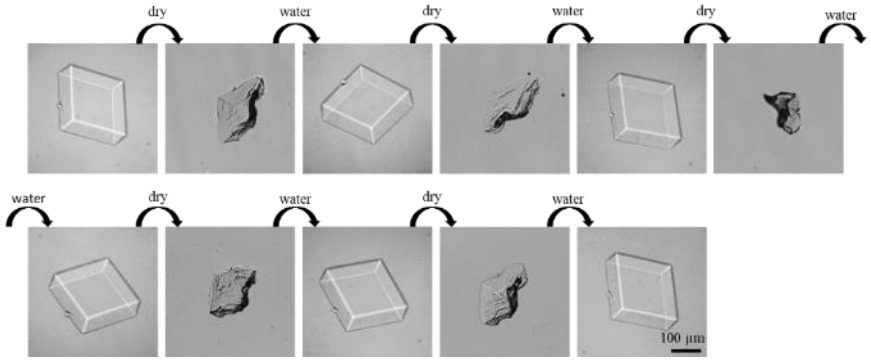

Figure 2-14 Stability of Ligated DNA $s\Delta^{4T}$ Crystals Against Dehydration-Rehydration Cycles with Water

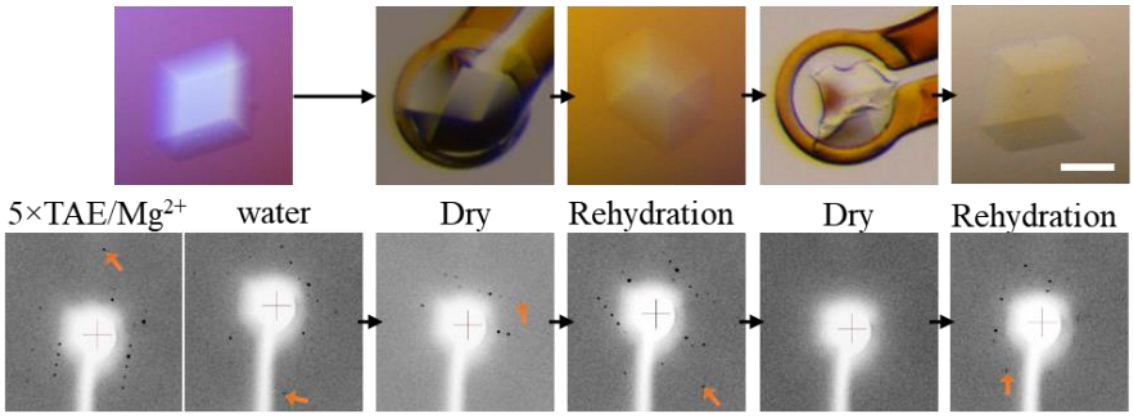

Figure 2-15 Stability of Ligated DNA $s\Delta^{4T}$ Crystals Against Dehydration-Rehydration-Freeze-Thaw and the Change in Crystallinity. Scale bar: 100 µm.

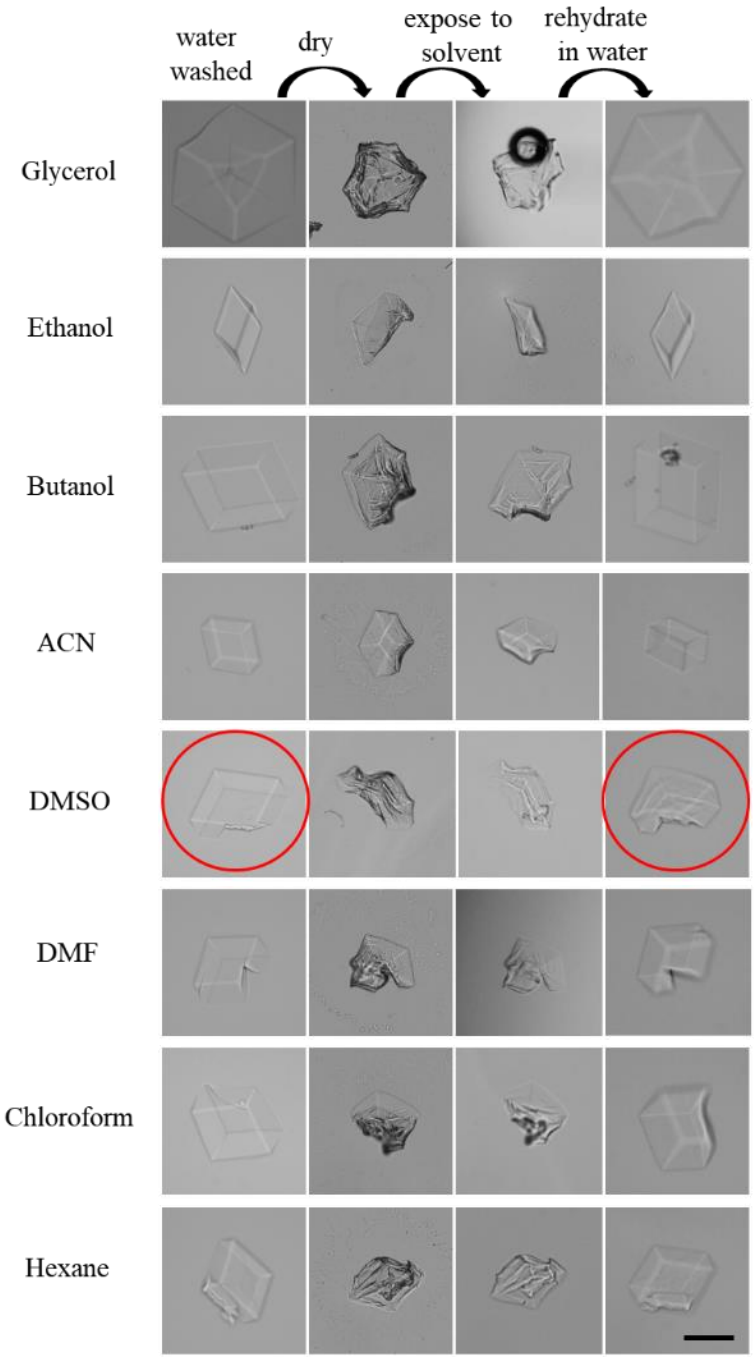

Figure 2-16 Stability of Ligated DNA sΔ^{4T} Crystals Against Organic Solvents. Scale bar: 100 µm.

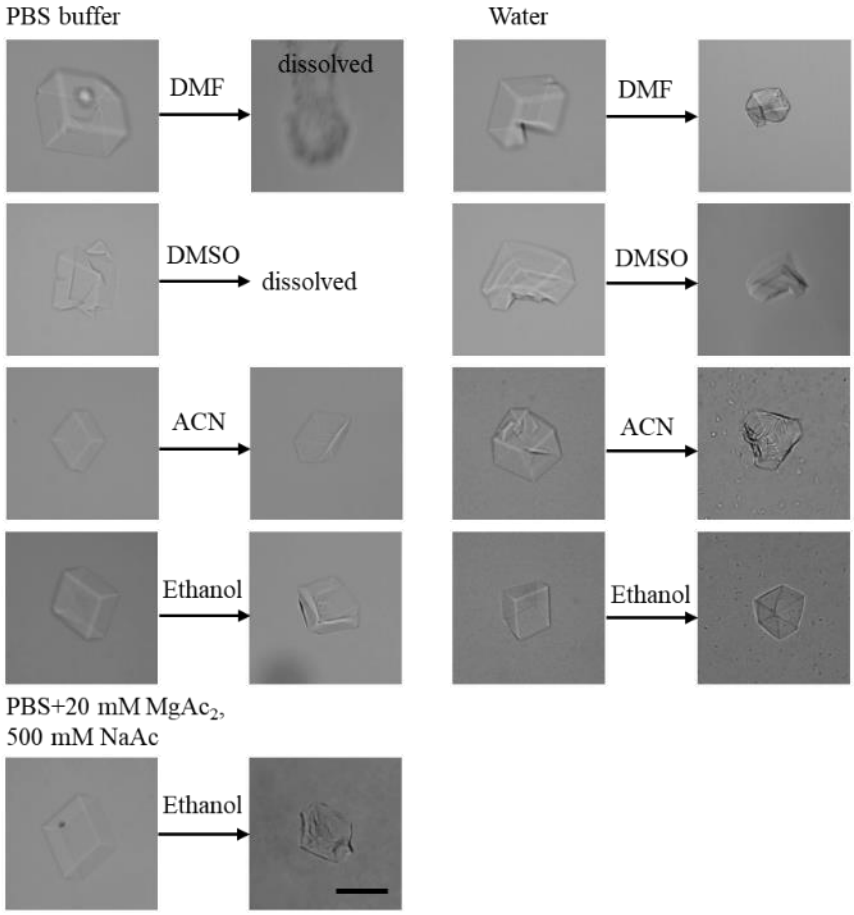

Figure 2-17 Stability of Ligated DNA $s\Delta^{4T}$ Crystals Against Water: Organic Solvents 1:1 (v:v). Scale bar: 100 μm.

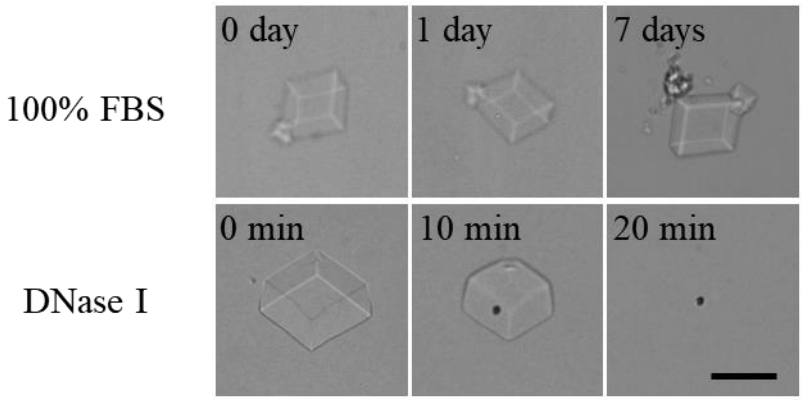

Figure 2-18 Stability of Ligated DNA $s\Delta^{4T}$ Crystals Against Enzymatic Degradation. Scale bar: 100 μm.

During handling, ligated DNA sΔ^{4T} crystals were found to be more mechanically robust than native crystals. It is difficult to break ligated crystals apart even by crushing and scratching. We intentionally pushed the crystal against the glass slide by cryo-loop and scratched it along the surface for tens of times, and the crystal was still intact without any cracks (Figure 2-11). In one attempt to analyze ligated sΔ^{4T} motif oligomers by native PAGE, crystals with and without ligation were crushed in 1×TAE/Mg^{2+} buffer to help with crystal dissolution (Figure 2-19). While crushed native crystals were rich in small, round-edged broken pieces, crushed ligated crystals were large pieces with still sharp edges. Possibly because these pieces were too large to enter the pores of polyacrylamide gel, nothing was observed in the lane for ligated crystals, as compared with an only single band of sΔ^{4T} motifs for crushed native crystals. The increase in mechanical strength makes the crystal handling much easier for downstream applications.

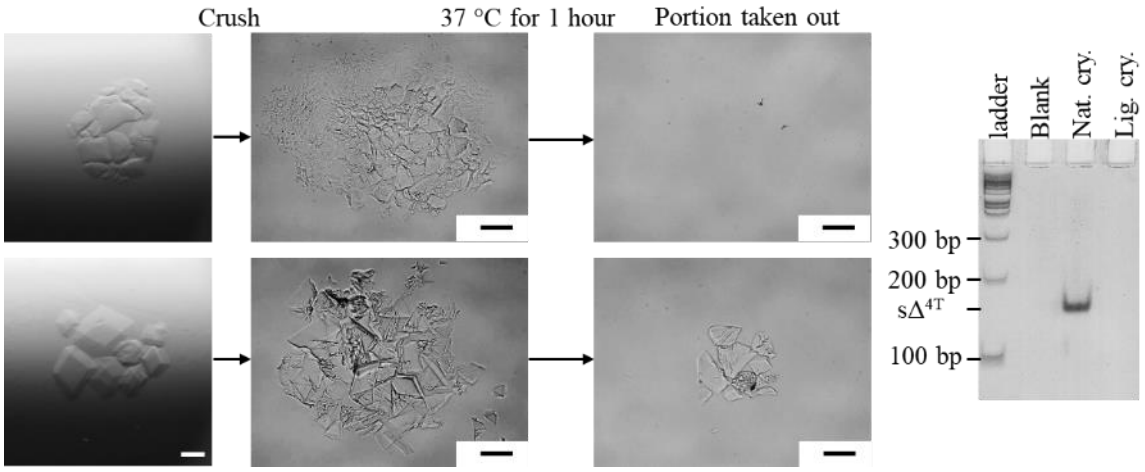

Figure 2-19 Mechanical Strength of Ligated DNA sΔ4T Crystals Against Crushing and Native PAGE (6%) Analysis. Scale bar: 100 μm.

2.4.3 Applications of Ligated DNA Crystal for Biocatalysis and Protein Capture

In previous studies, 3D DNA crystals have been demonstrated for their applications in arranging nanoparticles[43,44], arranging proteins[45] and encapsulating enzymes for biocatalysis[39]. Now with the advance of the stabilization of DNA sΔ^{4T} crystals, many new opportunities open up for these applications. For all these applications, the visual tracking of DNA crystals is important, and we first investigated how the ligated crystal can be stained and visualized. The ligated DNA crystal can be stained well with both fluorescent dyes and colorimetric dyes (Figure 2-20). Because

of the enhanced stability of the ligated crystal to accommodate low ionic strength, the potential problem that high ionic strength inhibits fluorescent intensity no longer exist. We were also able to study the staining kinetics by adding multiple dyes spontaneously (Figure 2-21) or in a stepwise fashion (Figure 2-22).

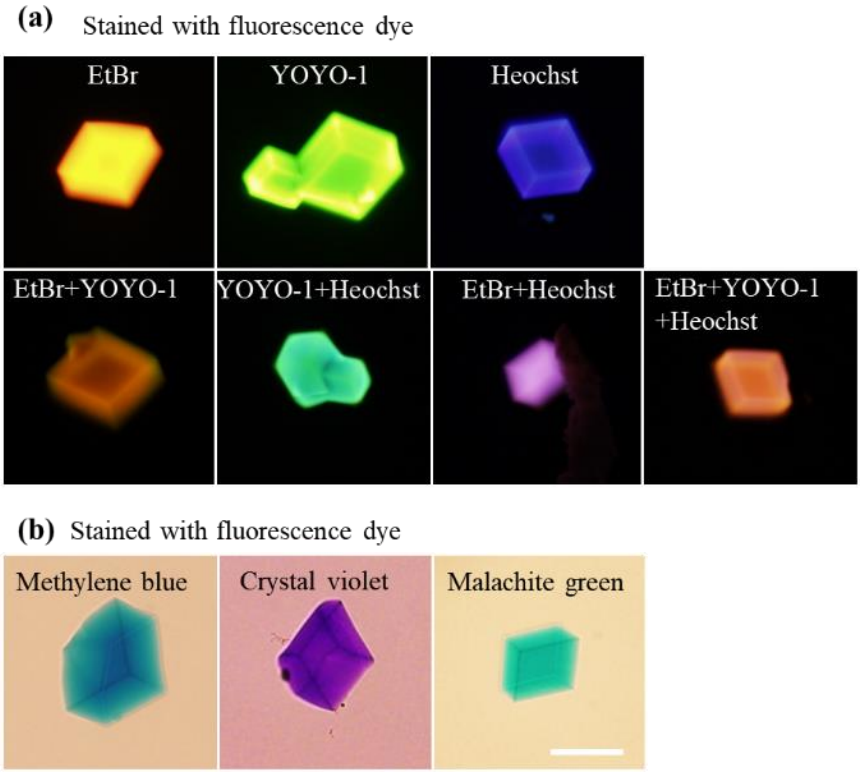

Figure 2-20 Staining of Ligated DNA $s\Delta^{4T}$ Crystal by Different Fluorescent Dyes. Scale bar: 100 μm.

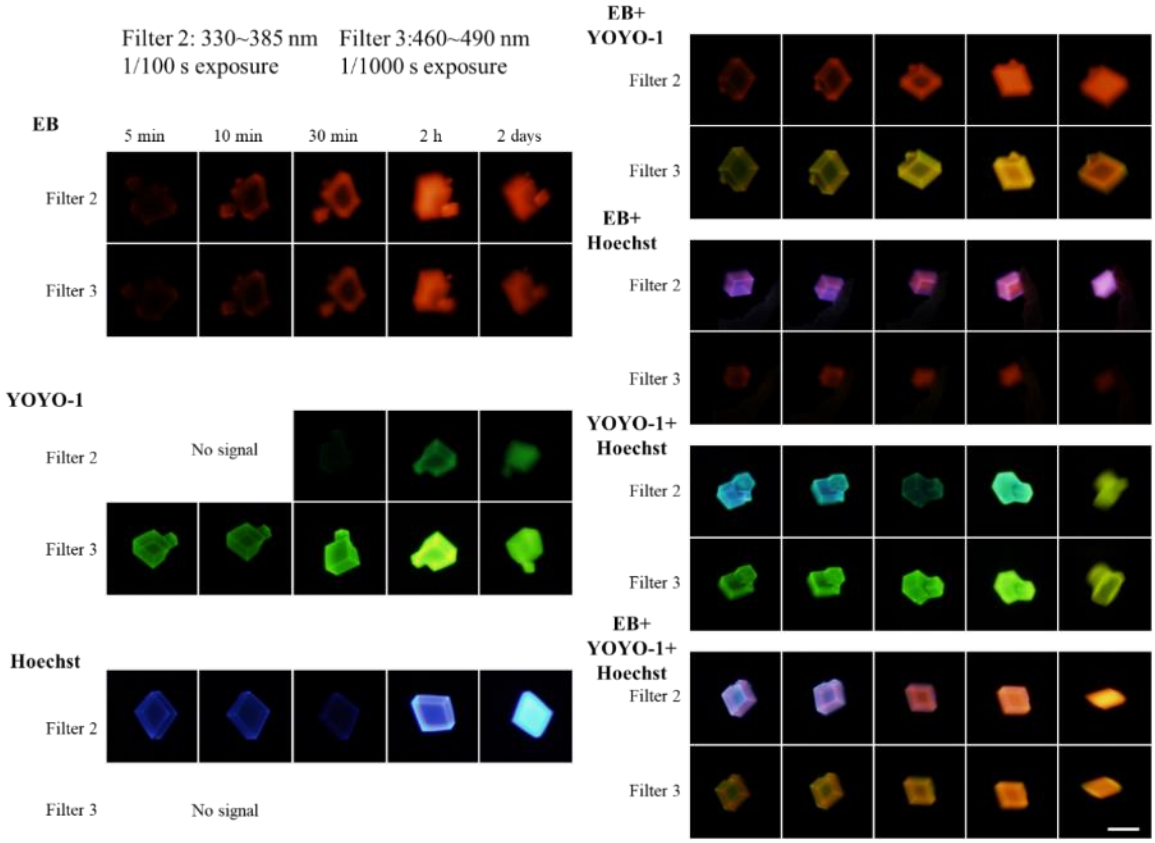

Figure 2-21 Staining Kinetics of Ligated DNA $s\Delta^{4T}$ Crystal with Fluorescent Dyes EB, YOYO-1 and Hoechst. Scale bar: 100 μm.

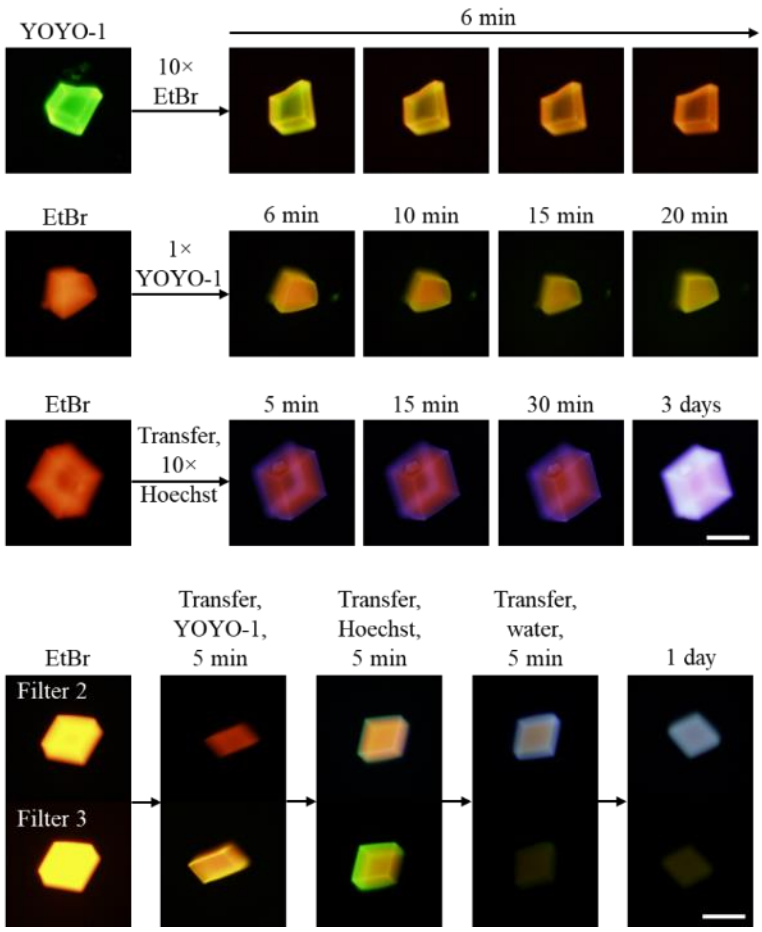

Figure 2-22 Stepwise Staining of Ligated DNA sΔ^{4T} Crystal by Multiple Fluorescent Dyes. Scale bar: 100 μm.

Next, we demonstrate that ligated DNA crystals can be used as robust biocatalysis vehicles. Horseradish peroxidase (HRP) and green fluorescence proteins (GFP) were used in this study, and their size and electrostatic potential are compared with the Δ^{4T} crystal lattice (Figure 2-23). When native DNA crystals were previously used to encapsulate enzymes for biocatalysis, enzymes need to be chosen carefully to make sure that they can function well in the buffers where DNA crystals are stable. However, many enzymes aggregate and lose activity in these buffers of high ionic strength, and the types of enzymes that can be used are limited. With ligated crystals, we no longer have such restrictions. Optimal buffer condition for enzymes can be directly applied to immobilized enzymes in the crystal. To prove this idea, we performed seven cycles of biocatalysis with HRP enzymes encapsulated in DNA crystal lattice in 100 mM KH_2PO_4, pH 5 (Figure 2-24). The buffer condition was taken from HRP assays, and crystal catalyst showed no change in

morphology throughout the catalysis process. The reaction and collection process also benefitted from the mechanical strength of the ligated crystal. The reaction mixture with crystal can be stirred (600 rpm) to speed up the heterogeneous catalysis process, and the transfer becomes easier without worrying about the cracking of crystals. One unusual phenomenon we observed during the catalysis is that the crystal turned violet color after the reaction. The reason for the color change is still under investigation, but control experiments showed that DNA, HRP and the ABTS reaction are all required for the color change (Figure 2-25).

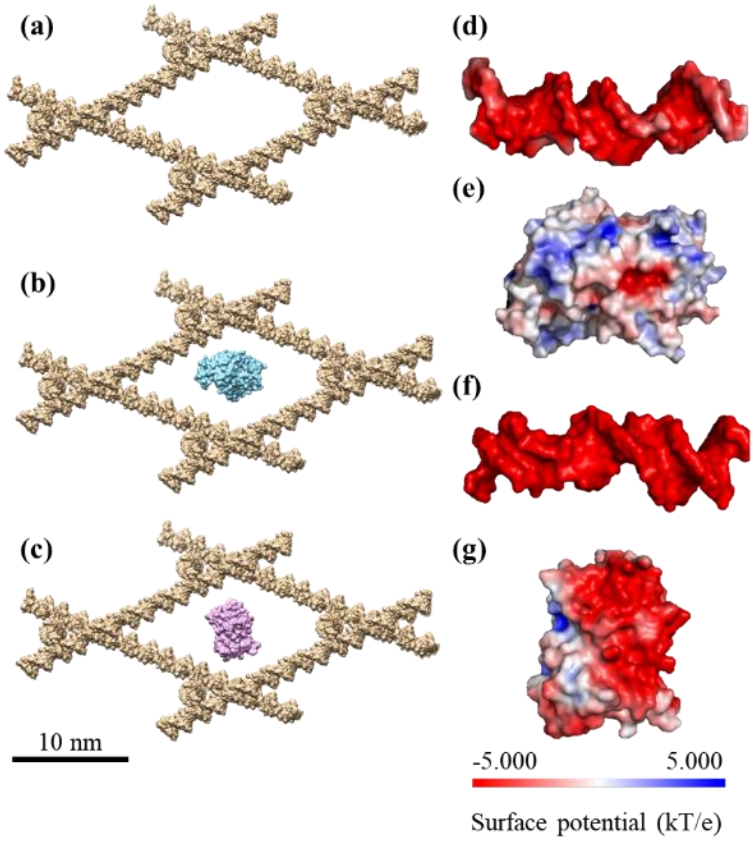

Figure 2-23 Models and Electrostatics of Protein Encapsulation in DNA $s\Delta^{4T}$ Crystal.

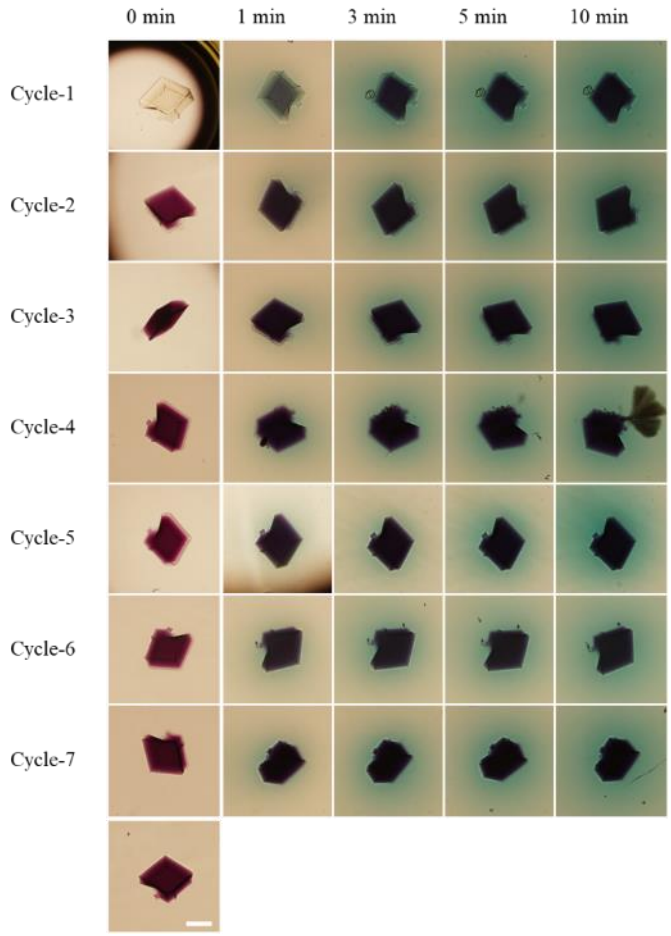

Figure 2-24 Seven Cycles of ABTS Catalysis in DNA sΔ^{4T} Crystal with Horseradish Peroxidase (HRP). Scale bar: 100 μm.

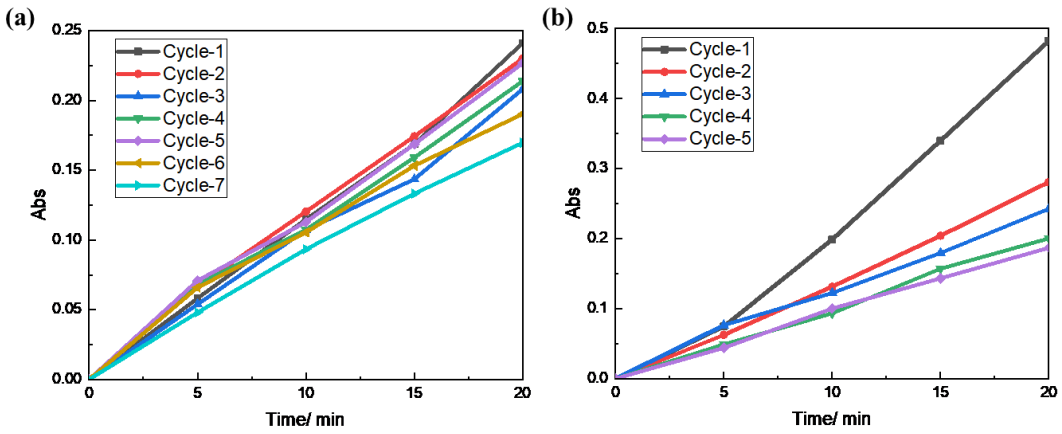

Figure 2-25 Catalysis Cycles of DNA sΔ^{4T} Crystal with Horseradish Peroxidase (HRP), with (a) and without (b) Polylysine Coating

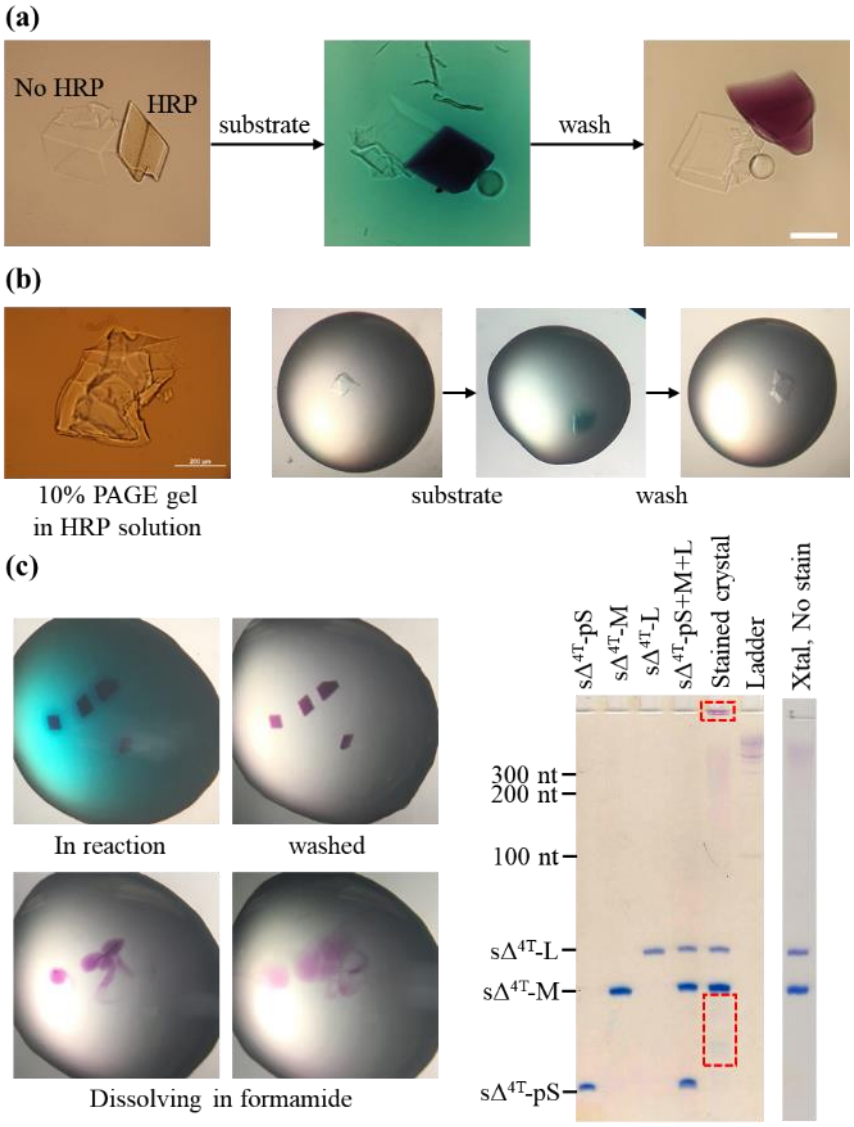

Figure 2-26 Control Experiments for DNA $s\Delta^{4T}$ Crystal Staining During Catalysis. Scale bar: 100 μm.

Ligated DNA crystals can also be used to capture and arrange proteins by specific interaction. Here we designed a new DNA tensegrity triangle motif with anti-His tag aptamer 6H7[55] (Figure 2-27). The optimal ionic condition for the aptamer binding with His-tag proteins is 50mM K_2HPO_4, 150mM NaCl, 0.05% Tween 20 (pH 7.5), where native DNA crystals will dissociate very fast. Compared with a control design without 6H7 aptamer, we were able to concentrate and capture His-tagged GFP proteins inside the crystal lattice. In another design with

larger crystal pores in an 8-turn edge length DNA crystal (detailed designs to be introduced in the next chapter), a 76 kD-recombinant protein His-tag-GFP-deaminase was captured.

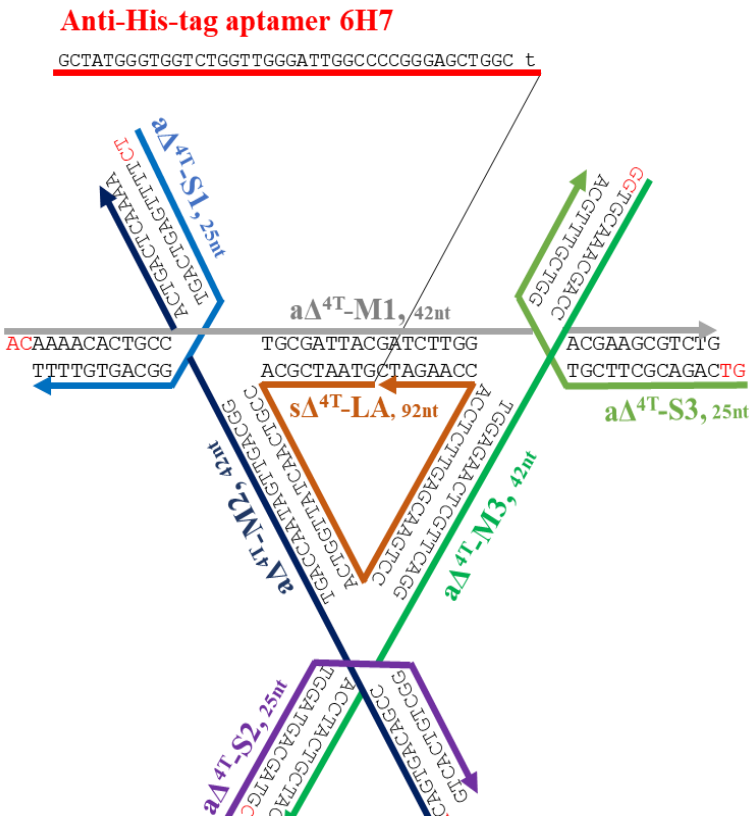

Figure 2-27 Schematic Design of DNA aΔ^{4T} Triangle with Anti-His-tag Aptamer 6H7

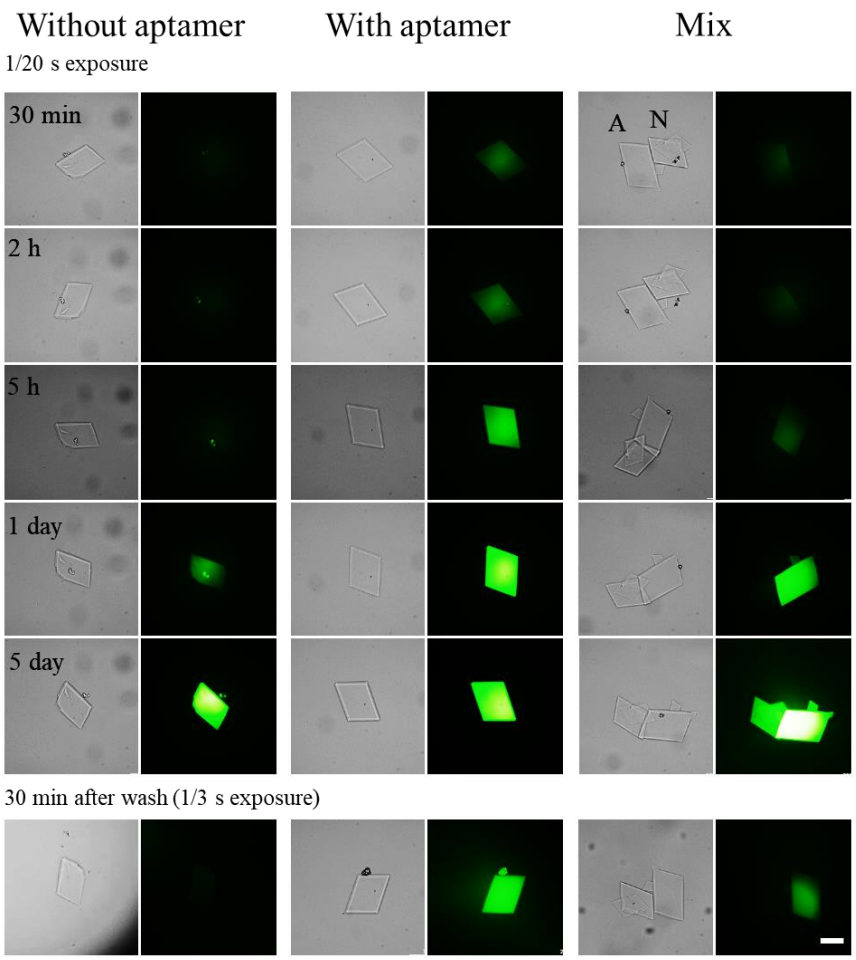

Figure 2-28 Protein Encapsulation for Ligated DNA aΔ^{4T} Crystals with Anti-His tag Aptamer 6H7. Scale bar: 100 µm.

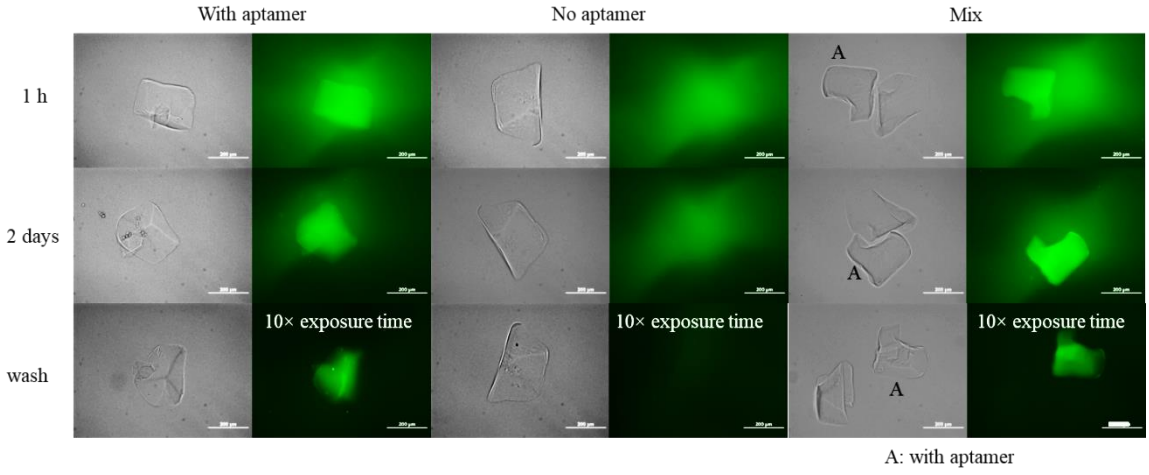

Figure 2-29 Protein Encapsulation for sΔ^{8T} Crystal with 76 kD Protein. Scale bar: 100 µm.

2.5 Conclusions

We developed an efficient method to prepare robust engineered DNA tensegrity triangle crystals by post-assembly ligation. With the optimal buffer condition and the increased crystal pore size, DNA crystals can be ligated at high yield. Ligated DNA crystals have enhanced stability over harsh solution conditions, and they are also mechanically more robust. Examples in dye staining, biocatalysis and protein capture demonstrated that ligated DNA crystals have broad and promising downstream applications. We believe our strategy to increase the stability of engineered 3D DNA crystals removes one key obstacle in DNA crystal engineering.

CHAPTER 3. MODELING AND STRUCTURAL CHARACTERIZATION OF ENGINEERED 3D DNA CRYSTAL

3.1 Introduction

For engineered 3D DNA crystals of tensegrity triangles, their X-ray diffraction resolutions are experimentally low. As we reported earlier[17], the best diffraction resolution was achieved in DNA triangles with 2-turn edge length to be around 4 Å. There was a tendency for the DNA crystals to diffract worse when the edge length was elongated. Low resolutions make it difficult to solve and study the crystal structures by X-ray diffraction, and new methods are required to characterize these crystals. Here we show that DNA tensegrity triangle crystals can be characterized by TEM imaging and the imaging results were validated with model predictions. Either large crystals were crushed into small pieces or microcrystals were prepared by fast nucleation, and then they were imaged by negative-stained TEM. The models were either built from rigid rods according to unit cell parameters from X-ray diffraction or predicted by finite element modeling framework CanDo. High correlations were found between TEM images and models. With the initial success of the characterization of 4-turn edge length DNA crystals, we further characterized a series of engineered DNA crystals with different edge length up to 8 turns. For these DNA crystals, they have pore sizes ranging from ~5 nm to ~20 nm. The 8-turn DNA crystal also has ~98% solvent, which is one of the highest solvent contents ever realized in crystalline materials.

3.2 Designs and Schemes

A series of DNA tensegrity triangles with elongated edge length were designed as shown in Figure 3-1. The detailed triangle motif design with sequence are provided in results and discussion session to compare with model and TEM images. In enlarged DNA triangle motif designs, the routings of the DNA strands are maintained, while the reciprocal exchange positions on each edge of the triangles are shifted. The inter-junction distance for 2-turn triangles edge-length triangles (Δ^{2T}) is 7 bp, and this distance is elongated to 17 bp for 3-turn and 4-turn triangles, and to 28 bp for 6-turn to 8-turn triangles. We also found that larger DNA triangles will need stronger sticky ends for self-assembly, possibly because of the increased electrostatic repulsion with larger

structures. Therefore, for Δ^{7T} and Δ^{8T} the sticky end overhangs were increased to 3 nt for successful crystal self-assembly.

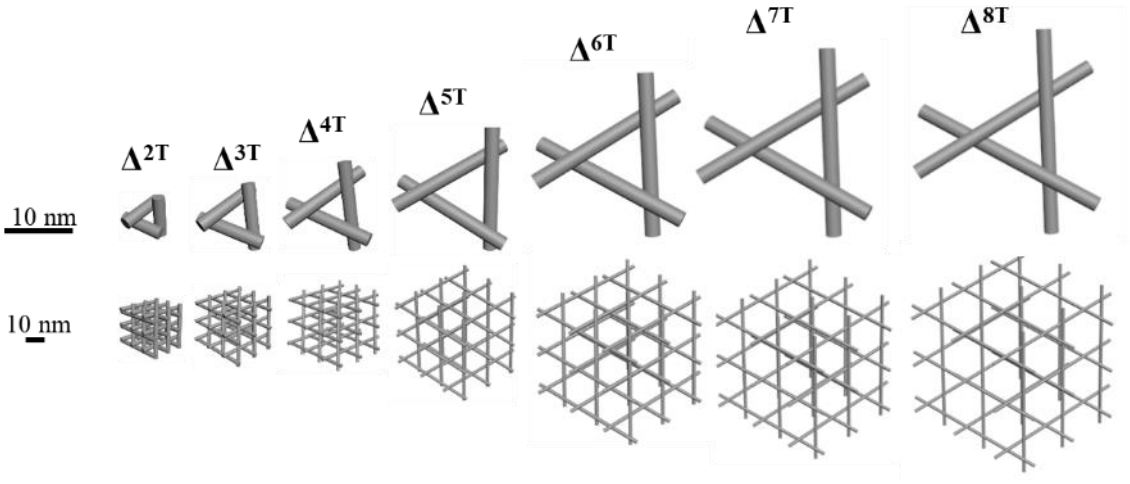

Figure 3-1 Rod Model of DNA Triangle and DNA Crystal Lattice (3×3×3) from 2-turn to 8-turn Helical Length

The macroscopic DNA crystals are generally too thick for TEM imaging, and we used cryo-loop to crush crystals into fine pieces before applying on the TEM grid for imaging. We also developed a fast nucleation method for assembling DNA microcrystals. A protocol based on LaMer model[46] is used. DNA motifs are quickly mixed with equal volumes of 5× to 10× TAE/Mg^{2+} buffer to push the DNA motif concentration high above its saturated solubility. Then burst nucleation happens, the motif concentration drops below saturation, and the nuclei continue to grow slowly into microcrystals. By controlling the motif and buffer concentration, we can obtain microcrystals of suitable size for TEM characterization.

3.3 Material and Methods

3.3.1 DNA Oligonucleotides

In addition to 2.3.1, extra strands:

sΔ^{2T}-L, 21 nt: 5'-CGCACCGCGCACCGCGCACCG-3'

sΔ^{2T}-M, 21 nt: 5'- GAAAAACCTGCGCGGACAAAA-3'

sΔ^{2T}-S, 14 nt: 5'- TCTTTTGTGGTTTT-3'

sΔ^{7T}-L, 84 nt: 5'-TAGATGCGGTCAGTAATTCACCACGAGCTAGATGCGGTCAGTAATTCACCACGAGCTAGATGCGGTCAGTAATTCACCACGAGC-3'
sΔ^{7T}-M, 74 nt: 5'-GAGGAGCAAACTTCTAACACTGCCTGAATTACTGACCGCATCTAGCTCGTGGACTGACTCCTTGAAAGACAGAG-3'
sΔ^{7T}-S, 46 nt: 5'- CTCCTCTGTCTTTCAAGGAGTCAGTGGCAGTGTTAGAAGTTTGCTC-3'

3.3.2 TEM Imaging

Microcrystals of DNA triangle crystals were obtained by mixing an equal volume of 2 μM DNA triangles in 0.2×TAE/Mg^{2+} with 10×TAE/Mg^{2+}. The mixture was incubated overnight at room temperature. Crushed crystals were prepared by diluting the crystal drop with 5×TAE/Mg^{2+} and crushing the crystals into small pieces by cryoloop under the microscope. 5 μL of microcrystals or crushed crystals were then incubated on glow discharged TEM grid (Formvar/Carbon 400 mesh Cu grid) for 10~15 mins for sufficient sample attachment. The grid was blotted by filter paper from the side and stained by 3 μL 0.8% uranium formate. Then the grid was quickly blotted again and stained with another 3 μL 0.8% uranium formate for 20 s. The grid was finally blotted and dried in air. The grids were characterized on FEI Tecnai T20 transmission electron microscope at Purdue microscope facility.

3.3.3 Rigid Rod Model for DNA Crystal Lattice

Rigid rod models for DNA crystals were built in 3dsmax software. All the DNA duplex are represented by cylinders of 2 nm diameter, regardless of sequence and nicks. According to the design, the duplexes will extend along the three dimensions of DNA crystal. The sites at the rod connections and the angles between rods are all calculated from X-ray diffraction data in the previous publication[17]. For the triangles with the same inter-junction length, the relative angles between duplexes are assumed to be the same. The models are presented with 3×3×3 and 5×5×5 unit cells.

3.3.4 CanDo Model for DNA Crystal Unit Cell

CanDo off-lattice prediction[48,49] was used to generate atomic models for the unit cells of designed DNA tensegrity triangle crystals. CanDo uses a mechanical model of DNA, where the model assumes that the double-helix is a homogeneous elastic rod with axial stretching, twisting, and bending stiffnesses. The DNA crystal unit cell was firstly drawn by Tiamat[50], and then used as input for CanDo prediction. The Holliday junction angles were all set as 60°. The generated PDB files were viewed in UCSF Chimera[51] with surface representation.

3.4 Results and Discussions

3.4.1 Characterization of DNA sΔ^{4T} Crystal

DNA sΔ^{4T} crystals with and without ligation both can only diffract to around 15 Å (Figure 3-2) on a home source X-ray diffractor. There is little change in the crystallographic symmetry and unit cell parameters before and after ligation, from the index of one X-ray diffraction frame. However, from these low-resolution diffraction data, we can hardly extract more detailed DNA crystal structure information.

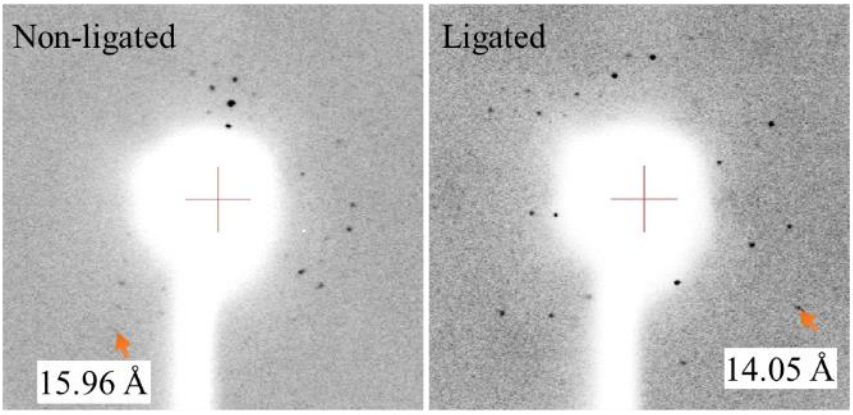

	Symmetry	a / Å	α / °	resolution/ Å
Non-ligated	Rhombohedral	134.9	110.9	~16
Ligated	Rhombohedral	135.6	110.2	~14

Figure 3-2 X-Ray Diffraction Resolution and Index of DNA sΔ^{4T} Crystal

From the X-ray diffraction information, rod models were constructed in 3ds max. An atomic model was also predicted by CanDo from only DNA sequence and cohesion information.

By comparison, we can see these two models demonstrated almost the same crystal arrangement (Figure 3-3). These crystal models were rotated in 3D space to correlate with the TEM images of DNA crystals viewed from different perspectives.

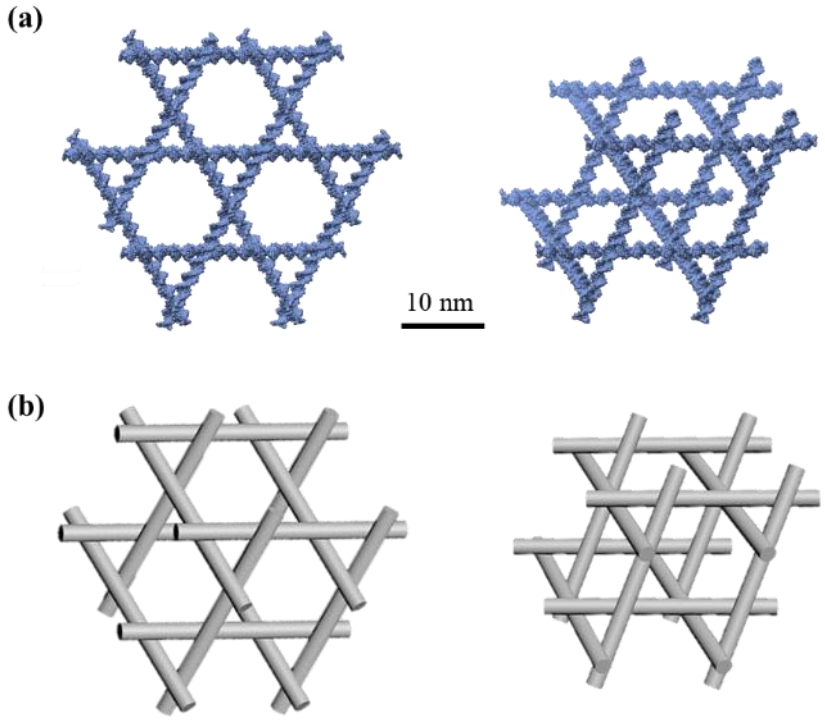

Figure 3-3 CanDo Model and Rod Model of DNA $s\Delta^{4T}$ Crystal

In the TEM imaging of crushed DNA $s\Delta^{4T}$ crystals, crystal pieces of around 200 nm can be found (Figure 3-4). In the zoom-in images, we can observe hexagonal-shaped patterns in the crystalline arrays. The repeating distance is very close to CanDo model. By imaging the $s\Delta^{4T}$ microcrystals, we were able to image on different regions of a 3D DNA single crystal (Figure 3-5). It was found that the exposing facets in the microcrystals are all <100> planes in the rhombohedral shape, and the three duplex orientations in the tensegrity triangle motif are on the same direction as the crystallographic axes of the crystal. Different patterns observed in TEM images can be correlated with the projection of the crystal model from different perspectives (Figure 3-6). $S\Delta^{4T}$ crystal was also imaged after ligation and no change was observed to the crystal lattice (Figure 3-7). The crushed crystals were also characterized by TEM tomography to show the internal channels (Figure 3-8) and by cryo-EM imaging (Figure 3-9).

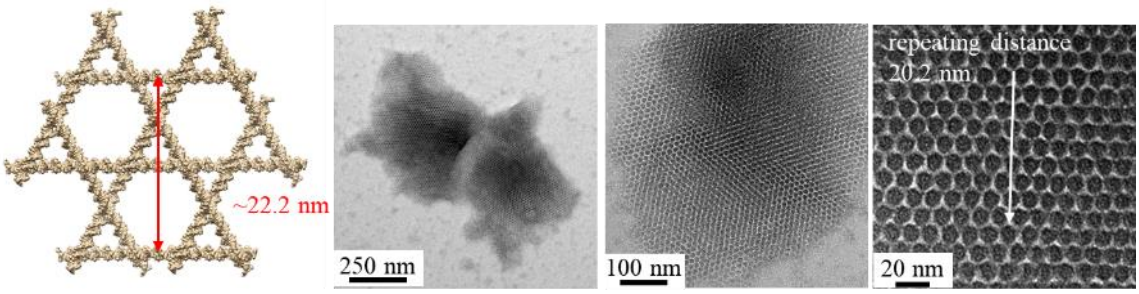

Figure 3-4 Atomic Model and TEM Imaging of DNA $s\Delta^{4T}$ Crystals

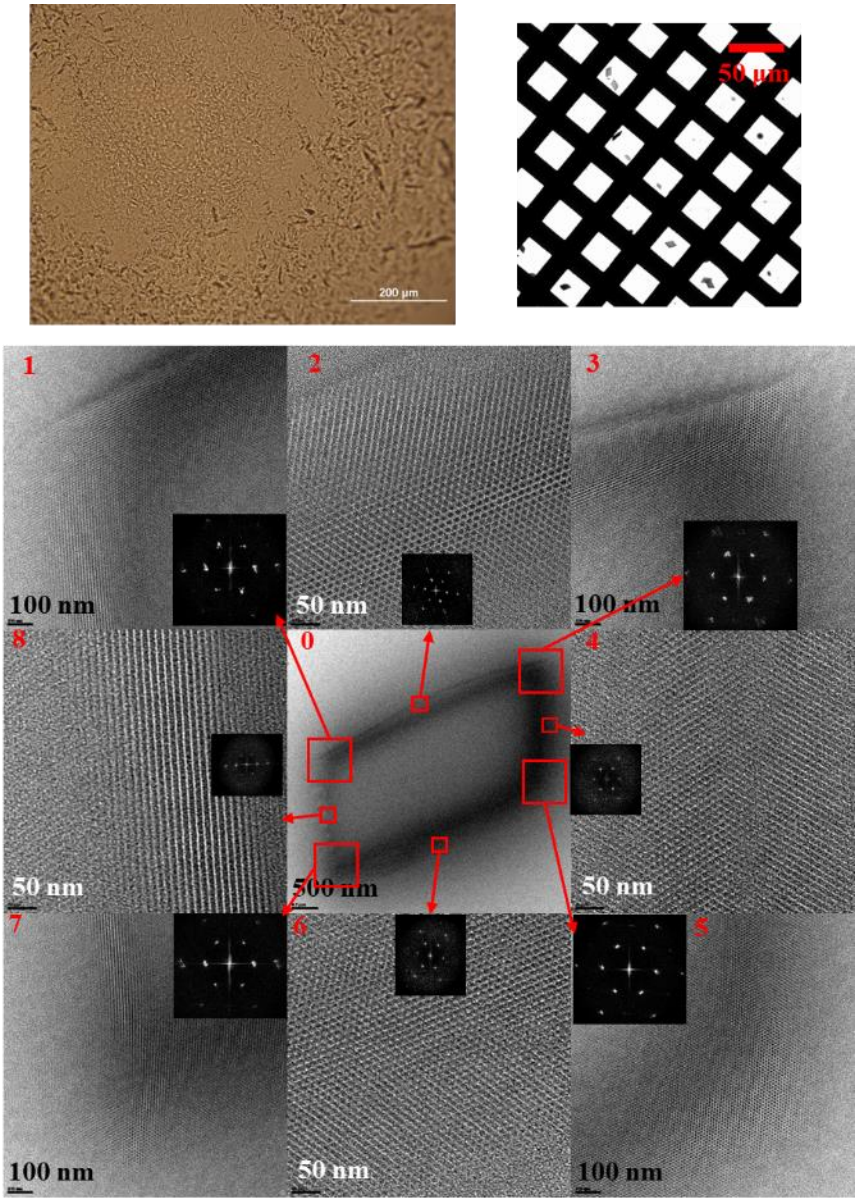

Figure 3-5 Optical Imaging and Negative-Stained TEM Imaging of DNA $a\Delta^{4T}$ Microcrystals

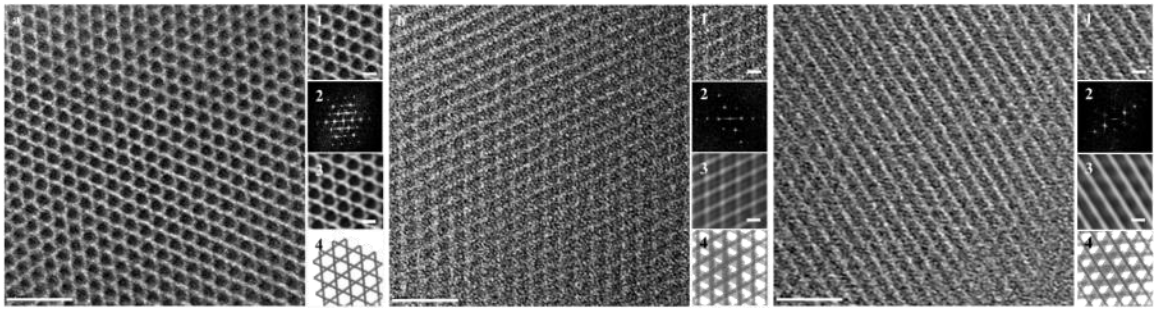

Figure 3-6 Zoom-in and FFT Reconstructed TEM Images of DNA aΔ^{4T} Crystals

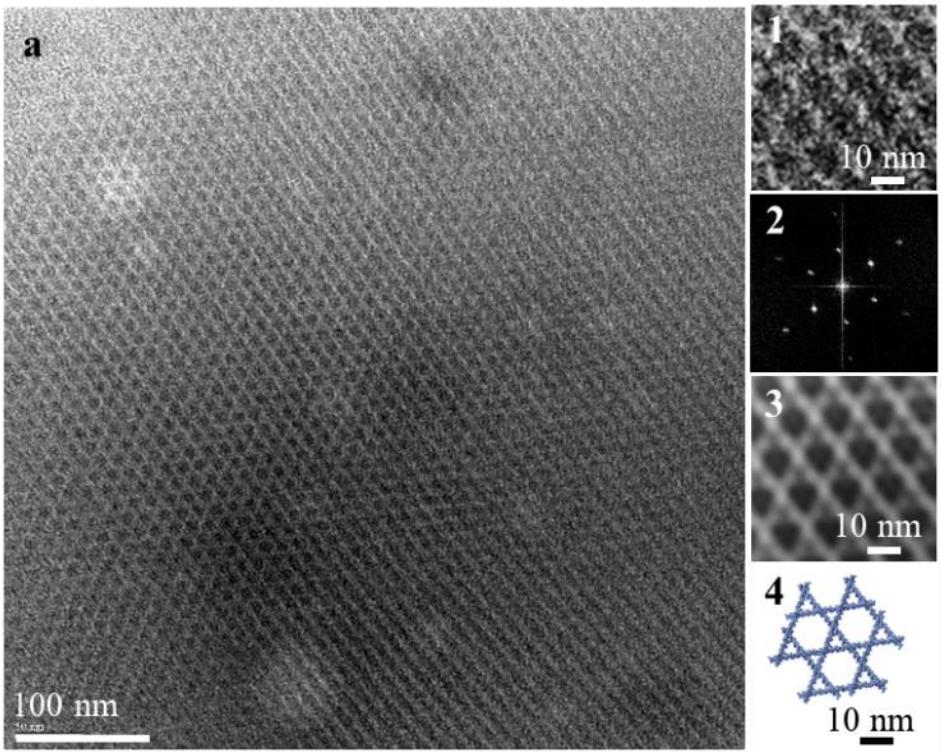

Figure 3-7 Negative-Stained TEM Imaging of DNA sΔ^{4T} Crystals after Ligation

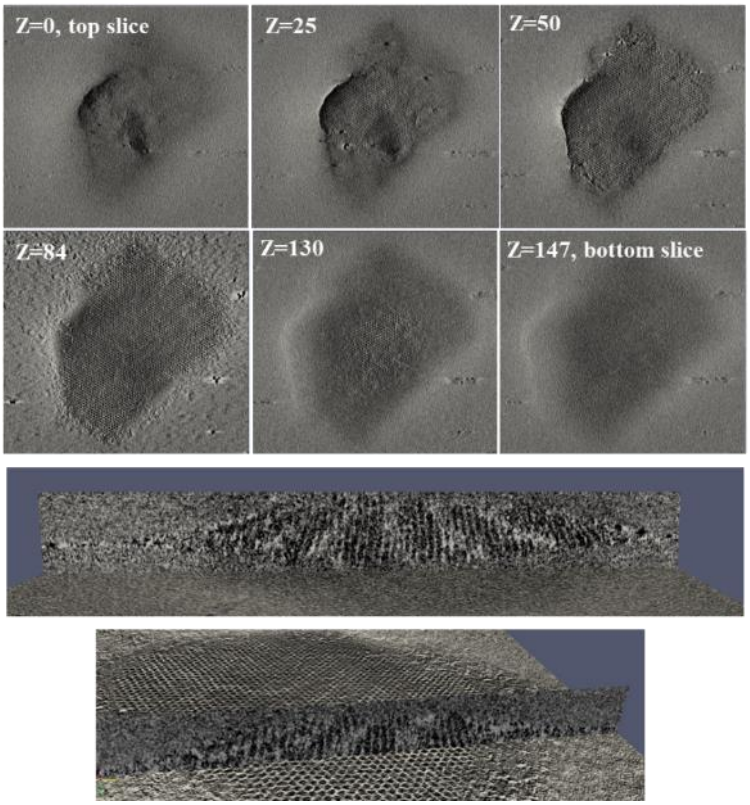

Figure 3-8 TEM Tomography Analysis of DNA $s\Delta^{4T}$ Crystals

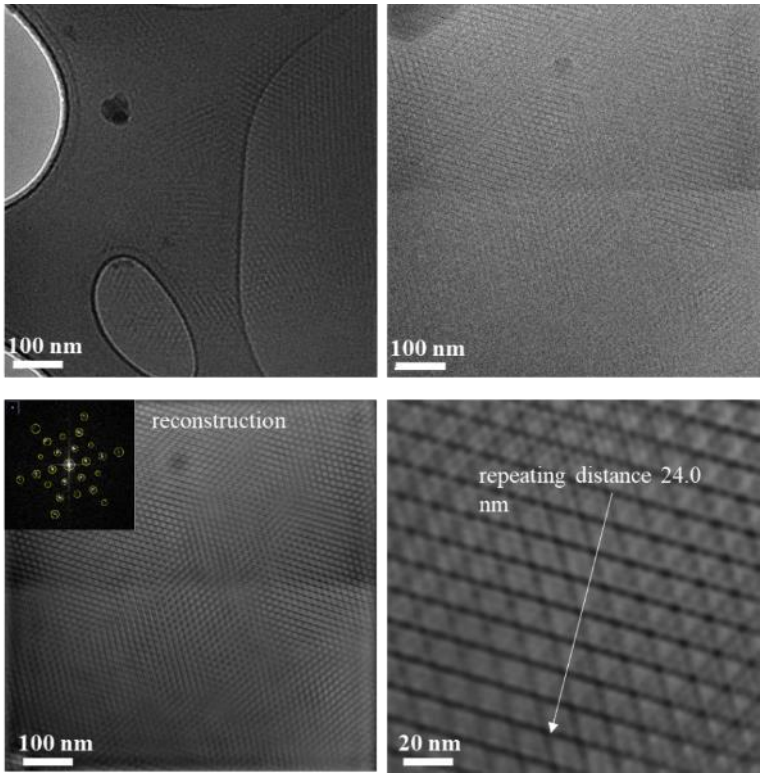

Figure 3-9 CryoEM Imaging and FFT Reconstruction of DNA $s\Delta^{4T}$ Crystals

3.4.2 Characterization of DNA sΔ^{2T} to sΔ^{8T} Crystal

Using the same characterization workflow, we characterized DNA triangle crystals from DNA triangles of increasing edge length, including 2-turn (Figure 3-10, 11), 3-turn (Figure 3-12, 13), 5-turn (Figure 3-14,15,16), 7-turn (Figure 3-17, 18, 19) and 8-turn triangles (Figure 3-20, 21,22). For each type of crystal, the atomic model was built for the crystal unit cell, and the theoretical repeating distance was compared with the distance measured from TEM images. For larger single crystalline lattice in a microcrystal, the rod model with extended lattice was used to correlate with different regions on the microcrystal. At last, we put the TEM images of all designs at the same length scale, and the significant increase in pore size from ~5 nm to ~20 nm can be observed (Figure 3-23).

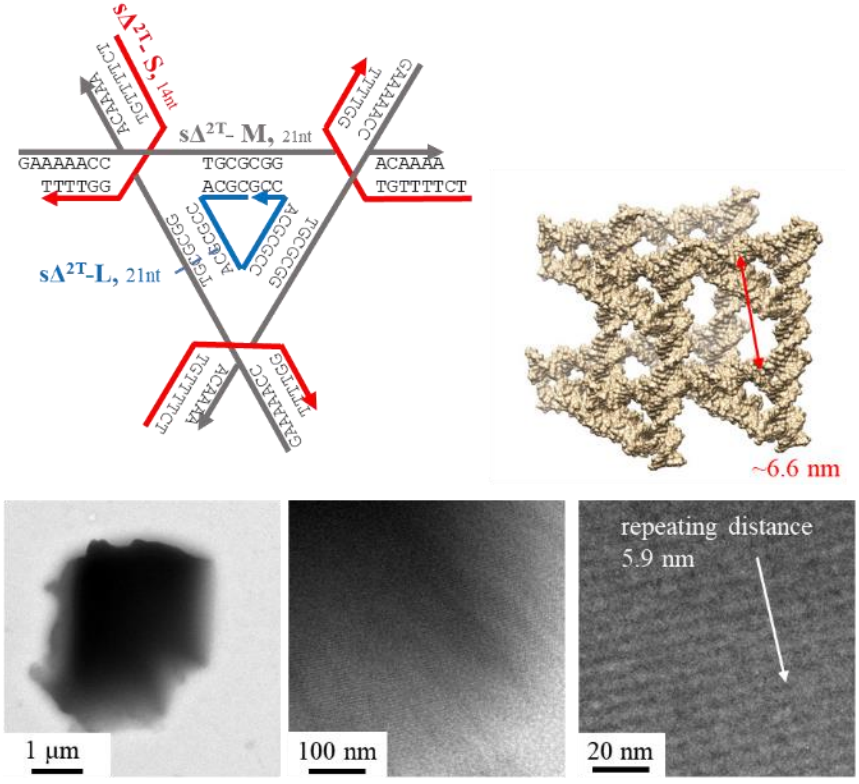

Figure 3-10 Design Scheme, Atomic Model and TEM Imaging of DNA sΔ^{2T} Crystals

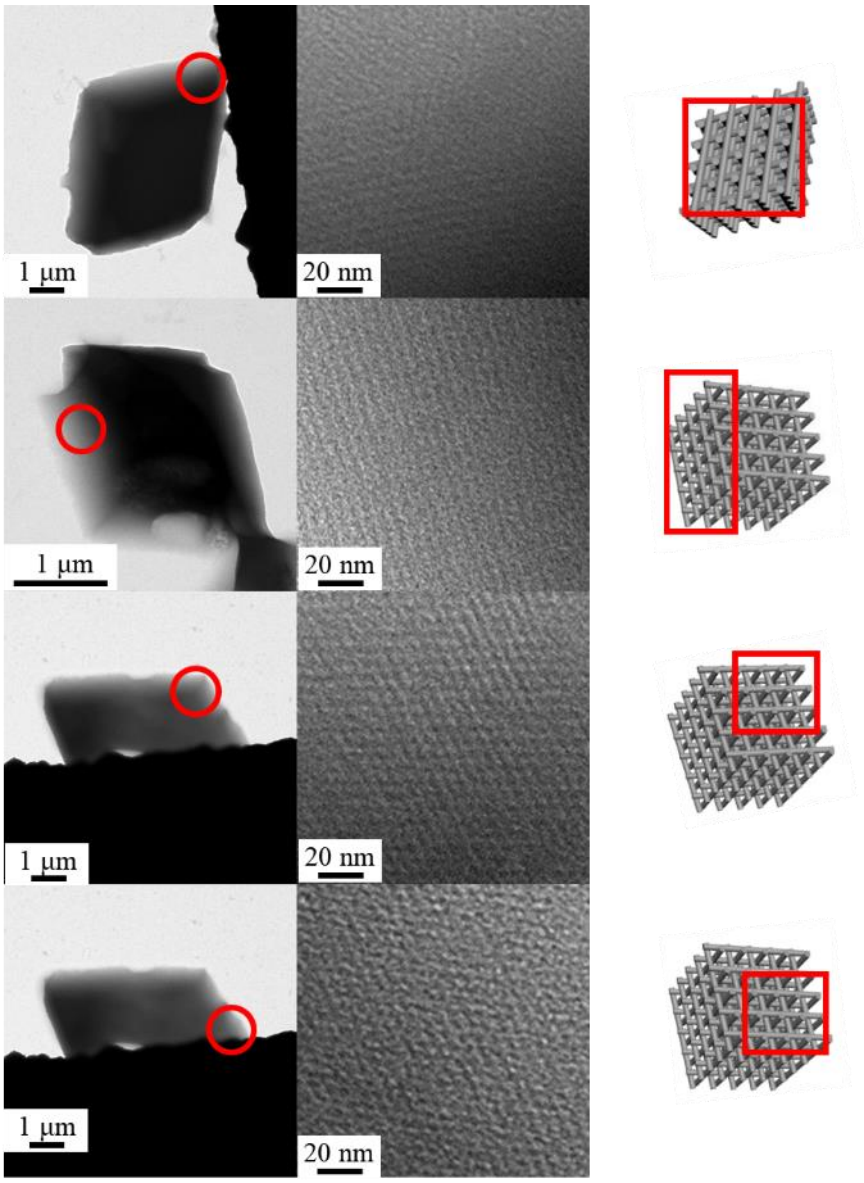

Figure 3-11 TEM Imaging of DNA $s\Delta^{2T}$ Crystals Compared with Rod Model

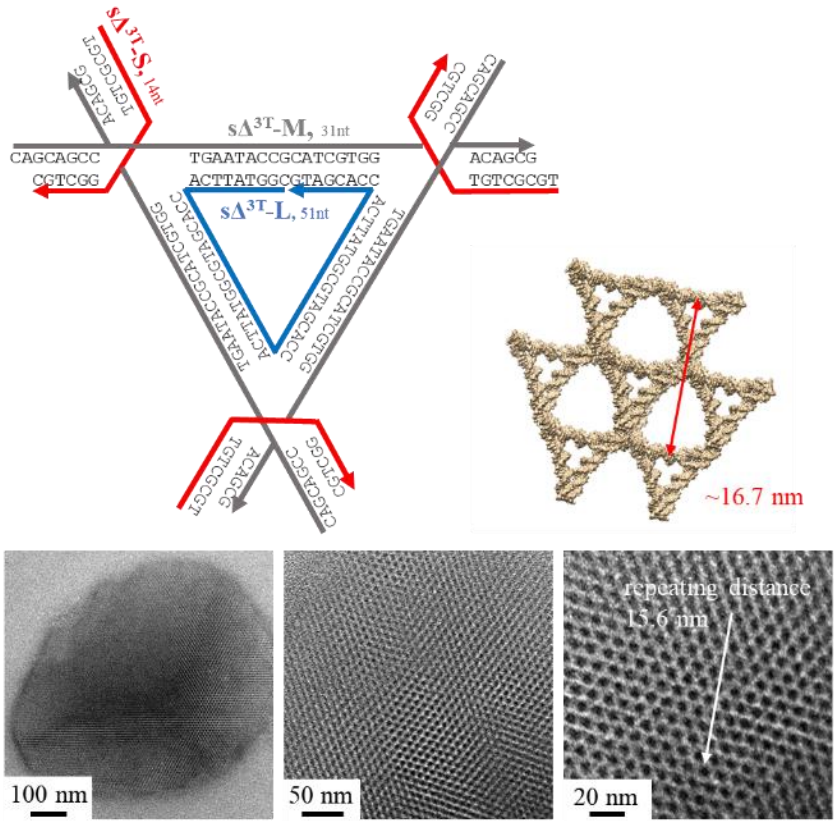

Figure 3-12 Design Scheme, Atomic Model and TEM Imaging of DNA sΔ^{3T} Crystals

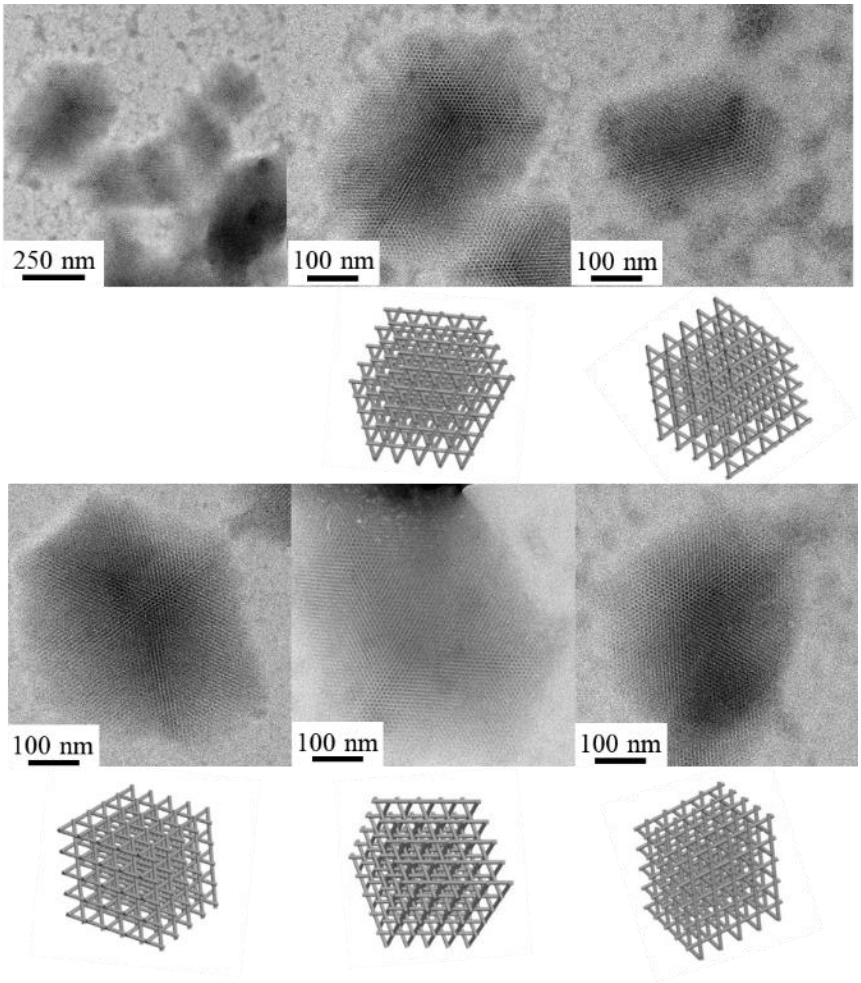

Figure 3-13 TEM Imaging of DNA $s\Delta^{3T}$ Crystals Compared with Rod Model

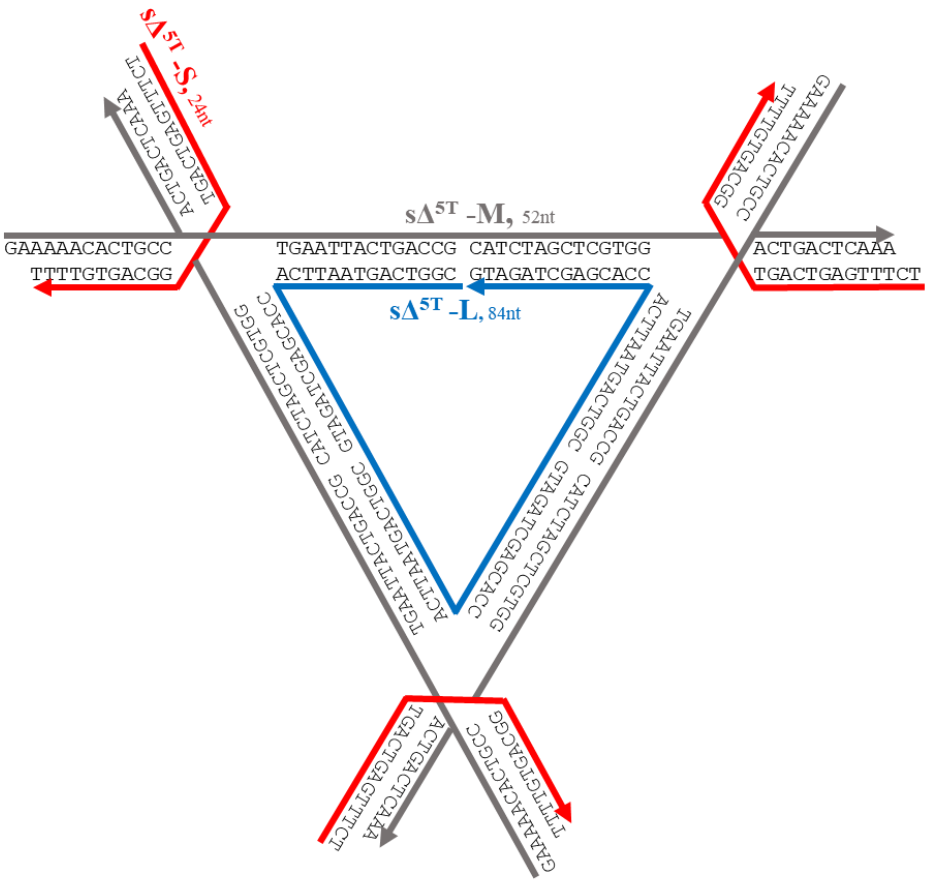

Figure 3-14 Design Scheme of DNA sΔ^{5T}

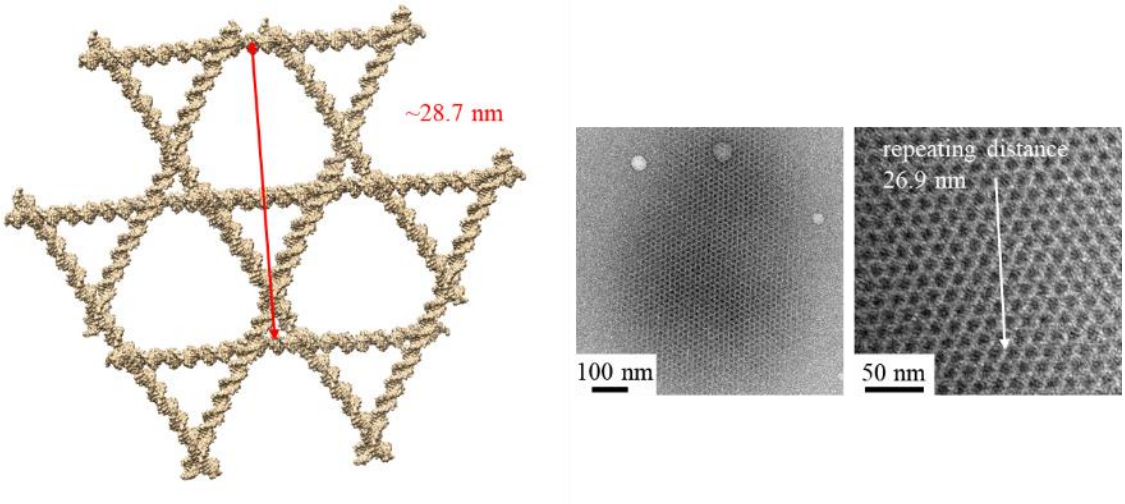

Figure 3-15 Atomic Model and TEM Imaging of DNA sΔ^{5T} Crystals

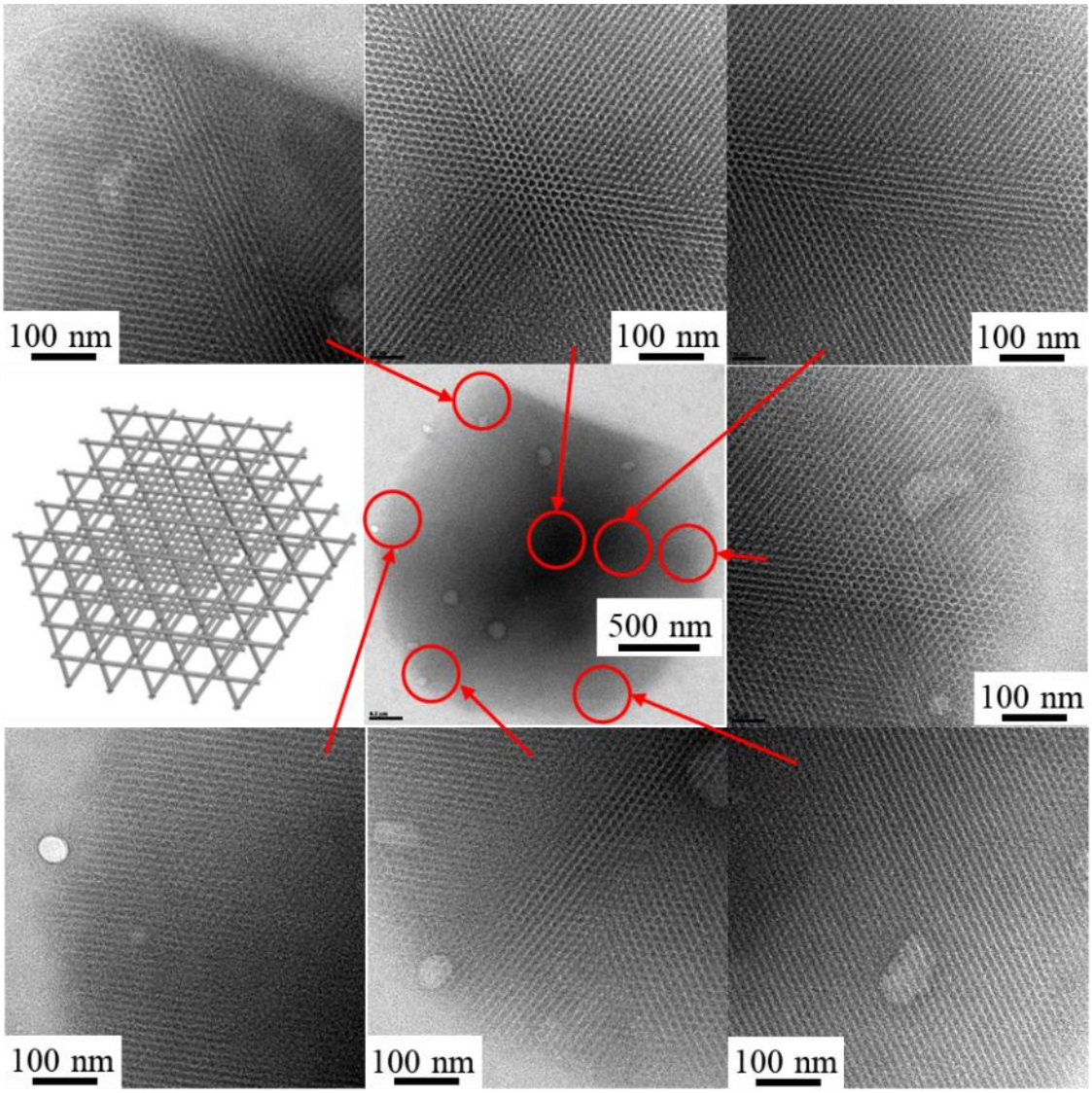

Figure 3-16 TEM Imaging of DNA $s\Delta^{5T}$ Crystals Compared with Rod Model

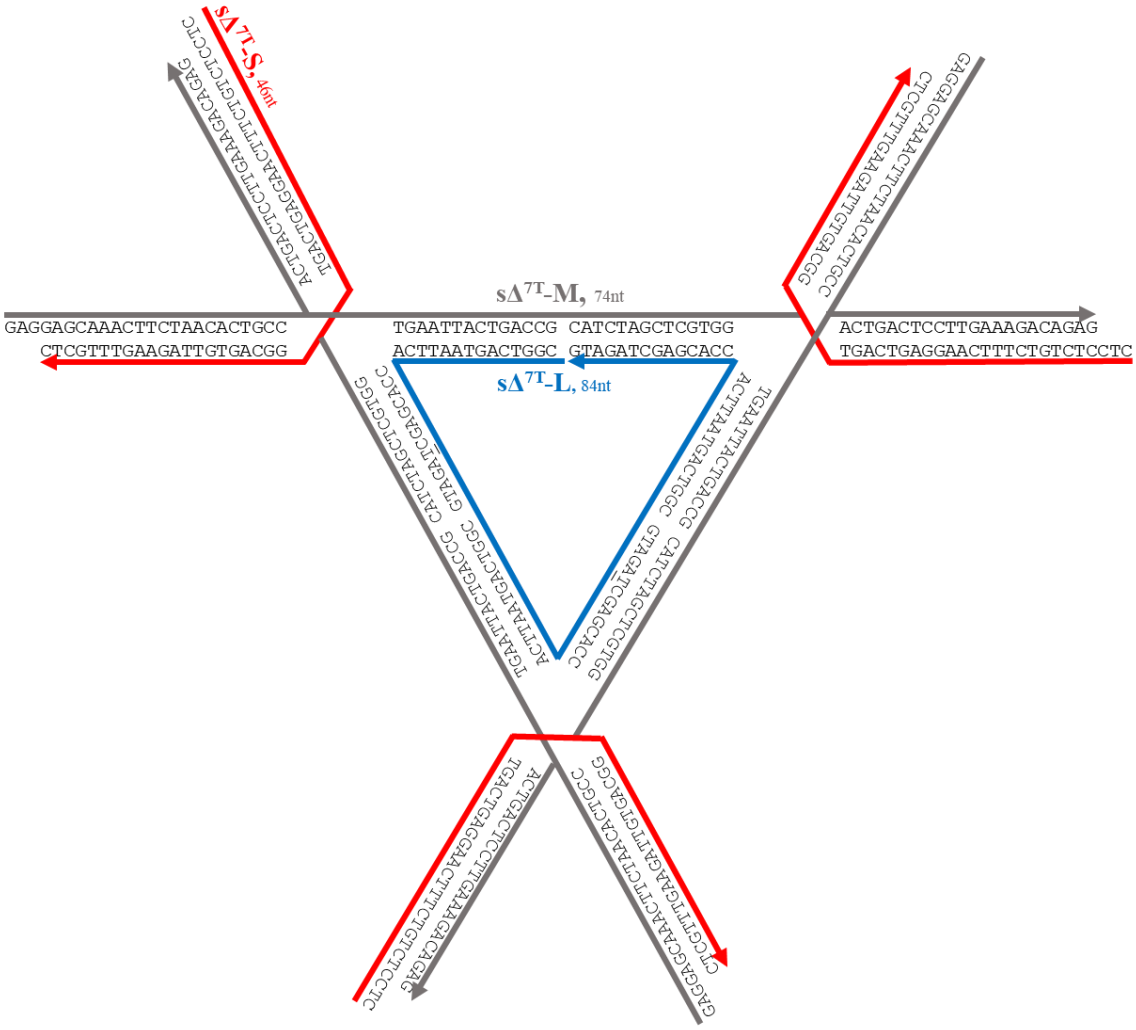

Figure 3-17 Design Scheme of DNA sΔ^{7T}

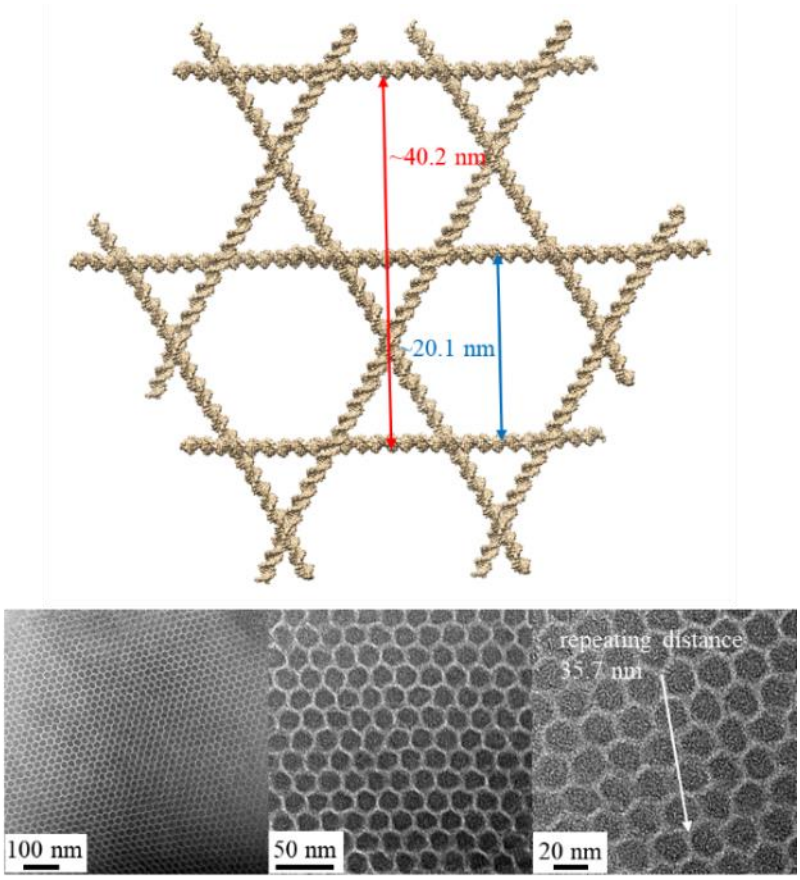

Figure 3-18 Atomic Model and TEM Imaging of DNA $s\Delta^{7T}$ Crystals

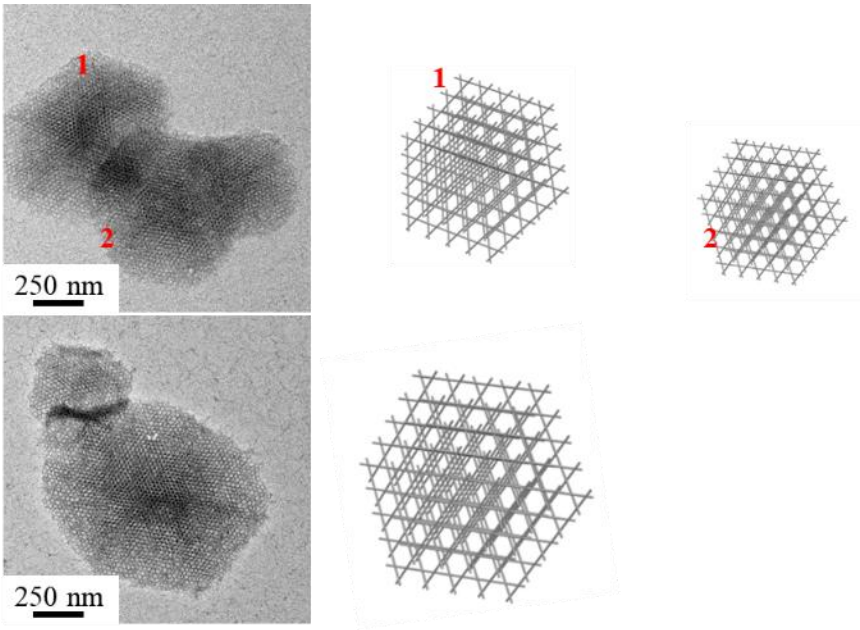

Figure 3-19 TEM Imaging of DNA $s\Delta^{7T}$ Crystals Compared with Rod Model

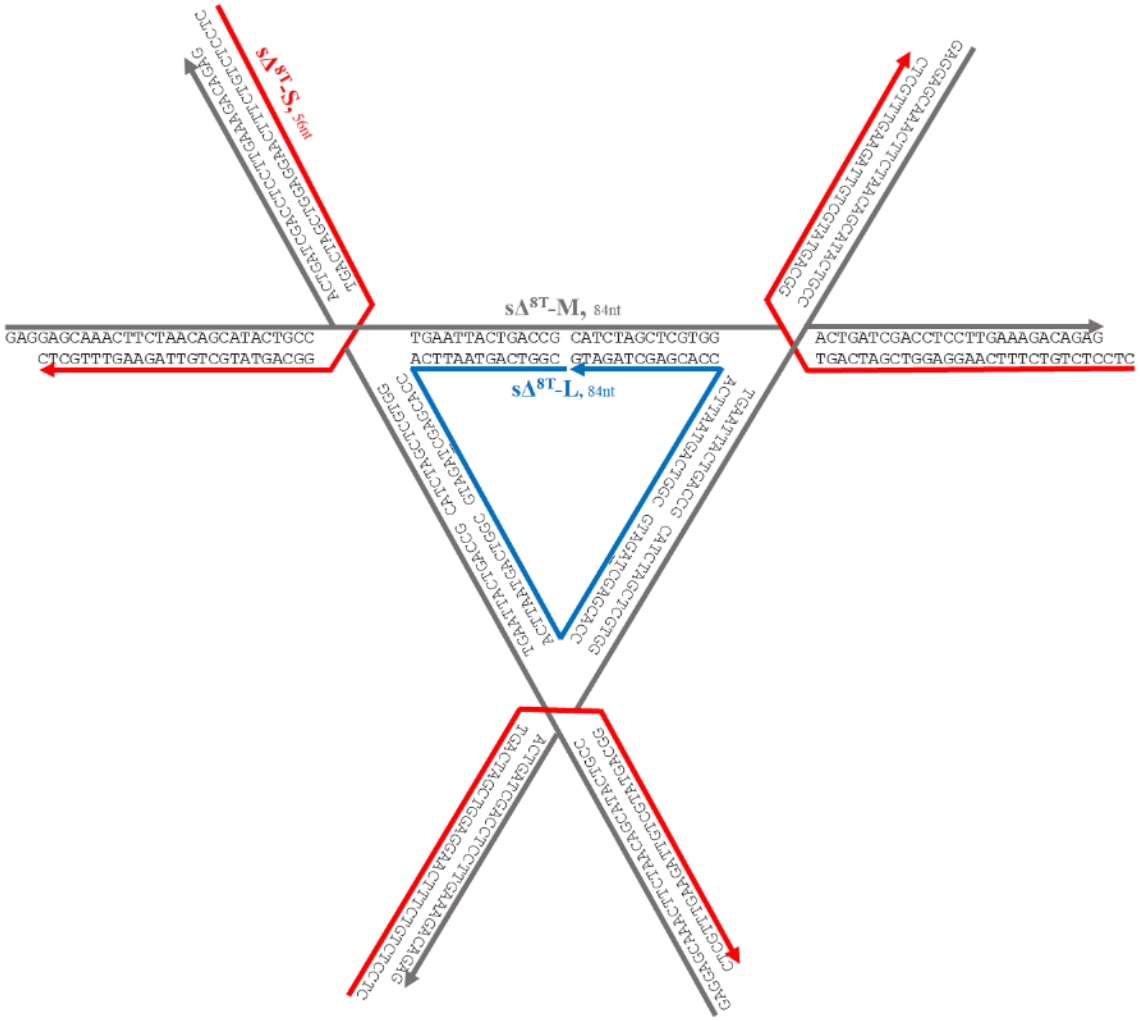

Figure 3-20 Design Scheme of DNA $s\Delta^{8T}$

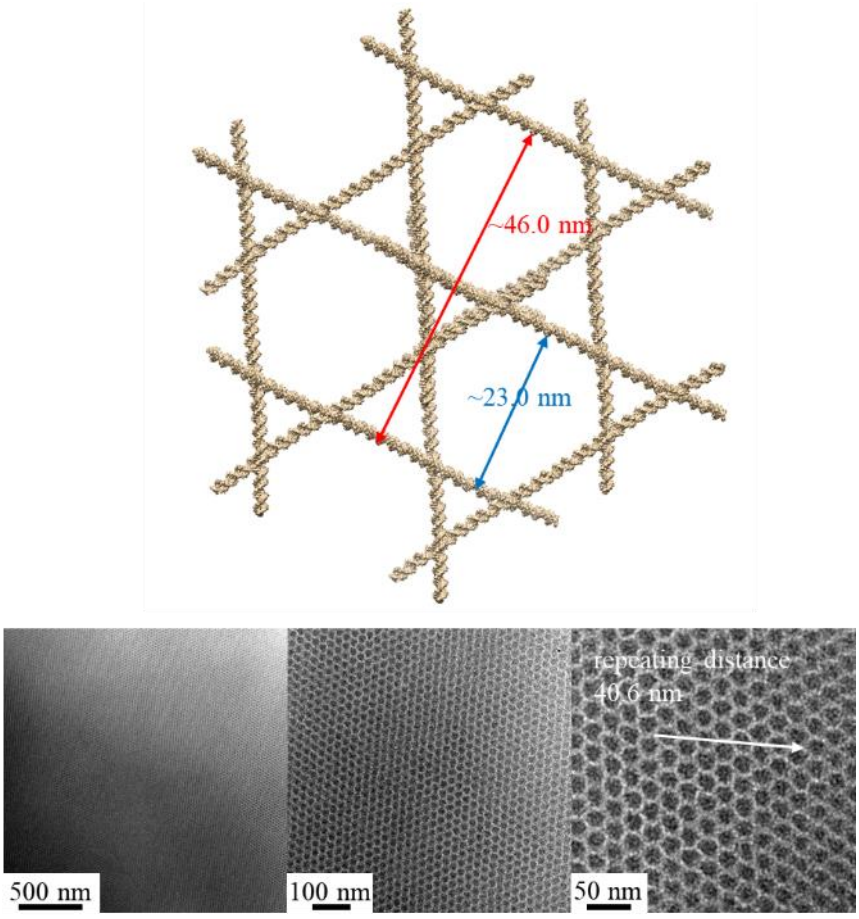

Figure 3-21 Atomic Model and TEM Imaging of DNA $s\Delta^{8T}$ Crystals

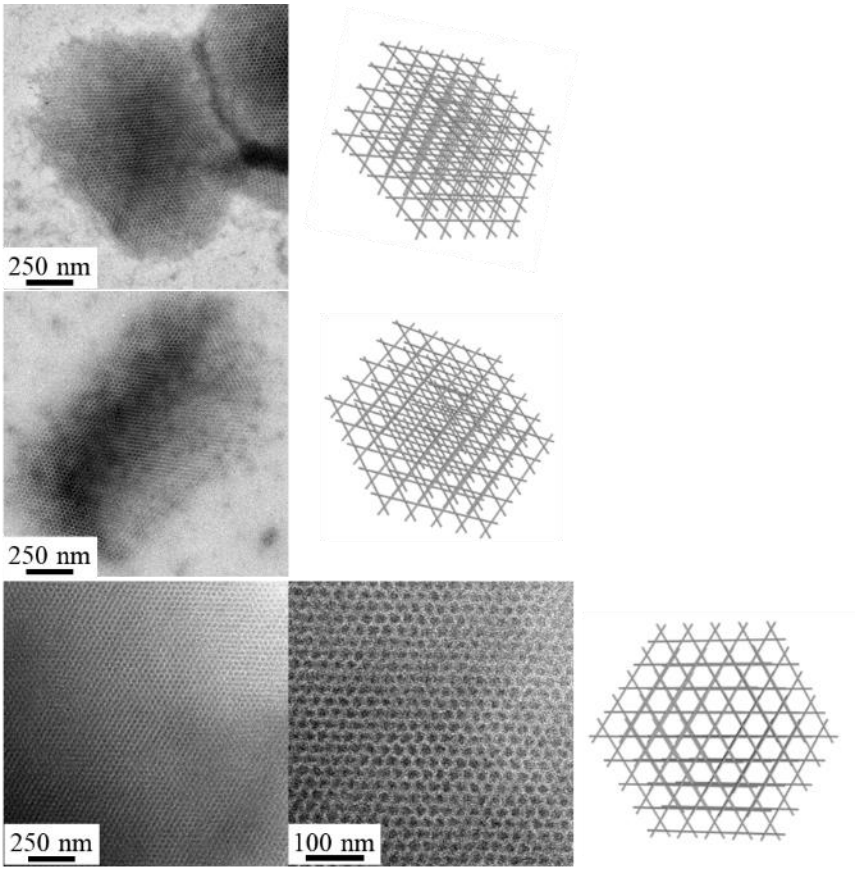

Figure 3-22 TEM Imaging of DNA $s\Delta^{8T}$ Crystals Compared with Rod Model

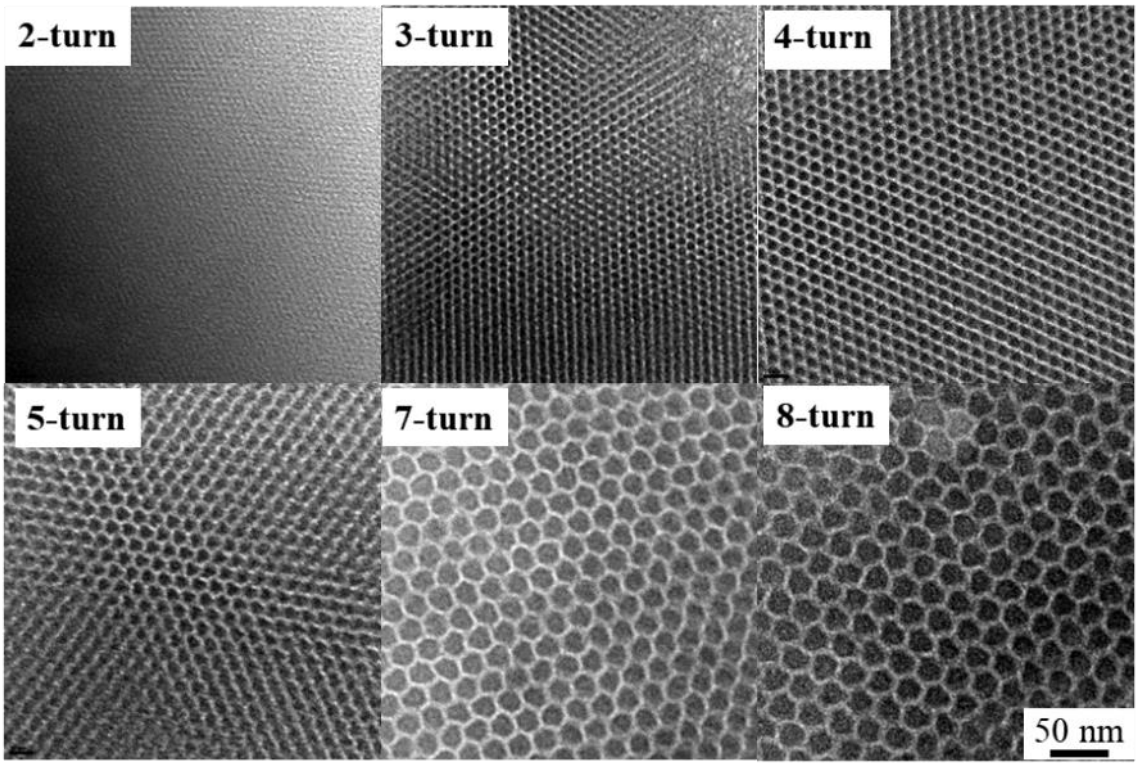

Figure 3-23 Comparison of DNA $s\Delta^{2T}$, $s\Delta^{3T}$, $s\Delta^{4T}$, $s\Delta^{5T}$, $s\Delta^{7T}$and $s\Delta^{8T}$ Crystal Pore Size by TEM Images at the Same Scale

3.5 Conclusions

Combining DNA structure modeling and TEM imaging, we solved the problem for the characterization of engineered DNA crystals with limited X-ray diffraction resolution. Our strategy will be highly applicable to other DNA crystal designs, such as non-equilateral DNA triangle crystals. Our work also facilitated the characterization during downstream functionalization of DNA crystals, such as arranging inorganic nanoparticles and enzymes inside the DNA crystal lattice.

CHAPTER 4. CONTROLLED LIGATION OF ENGINEERED 3D DNA CRYSTALS FOR NOVEL DNA MATERIALS

4.1 Introduction

In Chapter 2, we demonstrated that enzymatic ligation is an efficient post-assembly method to create covalent linkages at DNA crystal contacts and make robust crystals, and ligation enabled us to convert the weak, reversible sticky-ended cohesions into strong, covalent bonds. In nature, there are molecular crystals and covalent crystals, and there are also condensed matters with a coexistence of weak and strong interactions. One example is graphite, which has a layered structure: strong covalent bonds hold carbon atoms into honeycomb lattices in the same layers, while weak van der Waals forces stacked the layers onto one another. These materials inspired us to apply our ligation approach in a controlled manner to prepare similar material from engineered 3D DNA crystals, by selectively converting specific regions of the 3D crystal into covalent bonds. Here we show that the post-assembly ligation can be applied with directional control and spatial control in a 3D DNA crystal, and this leads to the preparation of a series of new DNA-based materials, including DNA chains and microtubes, DNA crystals with shelled morphology, as well as a reversibly expandable DNA crystal responsive to ionic strength. These DNA materials are inaccessible from other approaches.

4.2 Designs and Schemes

The first part of the design is to ligate the DNA crystal at the crystal contacts only in predesigned directions (Figure 4-1, first row). In a DNA tensegrity triangle, the three pairs of sticky ends are along the three crystallographic axises of the macroscopic crystal. Therefore, we can individually control each sticky end pair, for example, by their phosphorylation states, to make ligation only happen at the selected pairs, and this will lead to the ligation of selected directions in the macroscopic crystals. A DNA tensegrity triangle with asymmetric sequence was designed for this purpose (Figure 4-2). The triangle has three different pairs of sticky ends. For example, if we only want to ligate the direction of the GT/AC sticky ends, we will only phosphorylate M1 and S3 strands when assembling the DNA crystal. We can select either to ligate in only one dimension or

in two dimensions. Further dissociation process can break apart sticky-ended cohesion on other dimensions and extract low-dimensional structures from the 3D crystal.

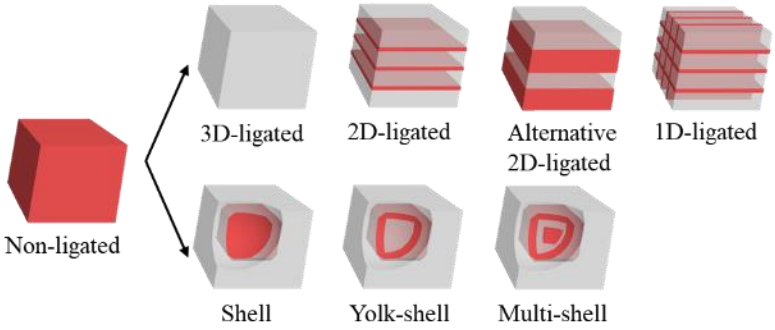

Figure 4-1 Dimensional and Spatial Controlled Ligation of DNA Crystals

We can also control ligation in 3D space by modulating the ligation kinetics and dose. It has also been observed in protein crystals that controlled crosslinking can result in "crystal containers" with a shell morphology[32]. Moreover, if this is combined with macro-seeding[23], which enables the self-assembly of extra crystal layers around the periphery of an existing crystal seed, we expect to obtain even more complicated crystal morphologies such as yolk-shell and multiple shells (Figure 4-1, second row).

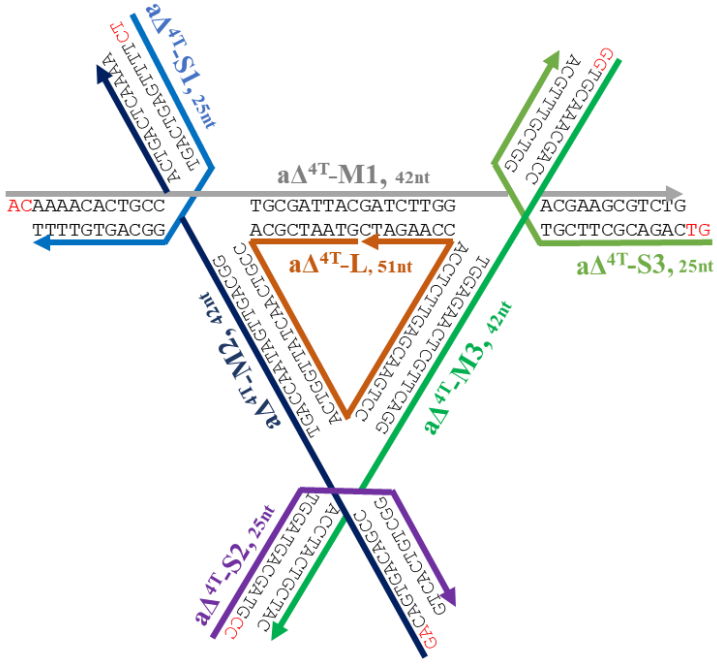

Figure 4-2 Design Scheme of DNA aΔ[4T]

4.3 Materials and Methods

4.3.1 DNA Oligonucleotides

In addition to 2.3.1, extra strands:

aΔ^{4T}-L-6H7, 51 nt: 5'-GTAATCGCACCGTCAACTATTGGTCACCTGAACGAGTTCTCCACCAAGATC-3'

aYΔ^{4T}-M1, 42 nt: 5'-CAAAAACACTGCCTGCGATTACGATCTTGGACGAAGCGTCTG-3'

aYΔ^{4T}-M2, 42 nt: 5'-AGCAGTGACAGCCTGACCAATAGTTGACGGACTGACTCAAAA-3'

aYΔ^{4T}-M3, 42 nt: 5'-CCTGCAAACGACCTGGAGAACTCGTTCAGGACCTACTGCTAC-3'

aYΔ^{4T}-S1, 25 nt: 5'-CTTTTTGAGTCAGTGGCAGTGTTTT-3'

aΔ^{4T}-S2B, 25 nt: 5'-GGGTAGCAGTAGGTGGCTGTCACTG-3'

aYΔ^{4T}-S3, 25 nt: 5'-TGCAGACGCTTCGT GGTCGTTTGCA-3'

4.3.2 Native PAGE Analysis

Native PAGE containing 6% polyacrylamide (19:1 acrylamide/ bisacrylamide) was run in Hoefer SE 600 electrophoresis unit at 250 V at room temperature in 1×TAE/Mg^{2+} buffer for 2-3 hours. After electrophoresis, the gels were stained by stains-all (Sigma), destained by light and scanned by an office HP scanner.

4.3.3 AFM Imaging

AFM images are captured by MultiMode 8 (Bruker) using ScanAsyst-fluid mode with ScanAsyst-fluid+ probes (Bruker) and ScanAsyst-air mode with ScanAsyst-air probes (Bruker). Parameters such as set-point and gains are automatically adjusted by software to optimize imaging conditions. For the 1D DNA triangle chains, 10 μL of exfoliated chains in 50 mM NaCl from a single crystal was applied on polylysine-treated mica, and 50 mM NaCl was used as imaging buffer. For expanded DNA crystal and DNA microtubes, they were fully dried on freshly cleaved mica and imaged in air.

4.3.4 TEM Imaging

TEM grid (Formvar/Carbon 400 mesh Cu grid) were glow discharged for 30 s, and DNA samples were incubated in the grid for 10~15 mins for sufficient sample attachment. The grid was blotted by filter paper from the side and stained by 3 μL 0.8% Uranium Formate. Then the grid

was quickly blotted again and stained with another 3 μL 0.8% Uranium Formate for 20 s. The grid was finally blotted and dried in air. The grids were characterized on FEI Tecnai T20 transmission electron microscope at Purdue microscope facility.

4.3.5 Fluorescence Imaging

The crystals were stained by 0.5~1 μM YOYO-1 for 1~2 min and then examined by optical microscopy (OLYMPUS, BX51) at 460~490 nm excitation wavelength.

4.4 Results and Discussions

4.4.1 Assembly of DNA aΔ^{4T}

The self-assembly of DNA aΔ^{4T} with different phosphorylation sites was checked by native PAGE. They all result in high assembly yield of the triangle product with minimal partial assemblies, as compared with the sΔ^{4T} assembly for control.

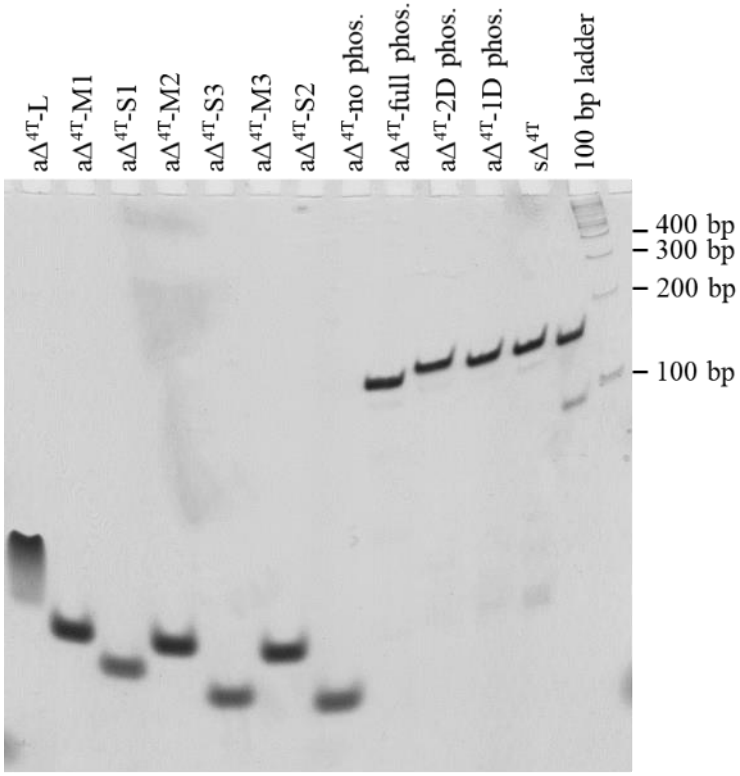

Phos.-Phosphorylated
2D phos.: L, M1, S1, M2, S3 phosphorylated
1D phos.: L, M1, S3 phosphorylated

Figure 4-3 Native PAGE (6%) Analysis of DNA aΔ^{4T}

4.4.2 Preparation of 1D DNA Nanochains

DNA aΔ^{4T} crystals were ligated at GT/AC sticky ends, washed, and then dissociated at low ionic strength (Figure 4-4 a). The crystal fully dissolved in water but remained intact in 100 mM NaCl even after overnight incubation. 50 mM NaCl was selected as a mild condition to dissociate the 3D crystals into 1D chains. The chains are about 1.5 nm high, 15 nm wide and about 1 μm in length (Figure 4-4 b). Their length did not reach the dimension of the 3D crystal because of the restriction from ligation yield, where any single sticky ends not ligated will break a continuous chain.

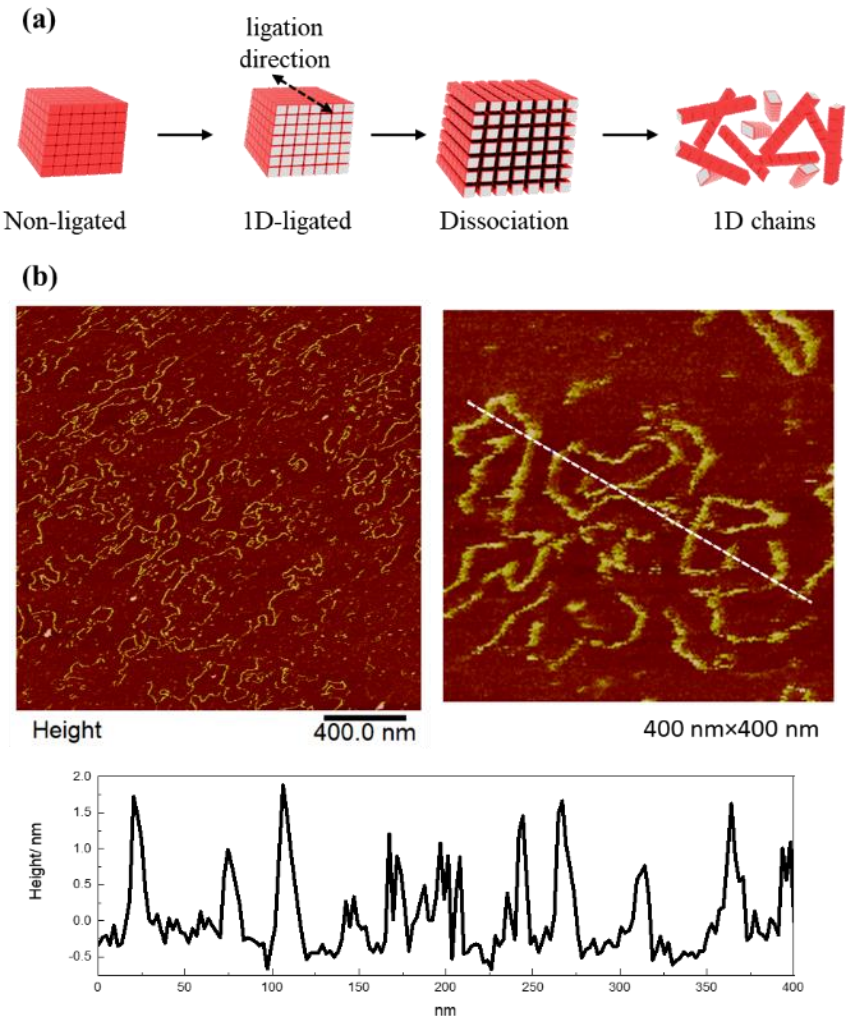

Figure 4-4 1D Chains Prepared from 1D Ligated DNA aΔ^{4T} Crystals

4.4.3 1D-reversibly Expandable DNA Crystal

DNA aΔ^{4T} crystals were ligated at GT/AC and GA/TC sticky ends, which will turn the crystal into a very similar structure as graphite: the covalently ligated 2D arrays were connected layer by layer with sticky ends into a 3D crystal. Our initial purpose was to exfoliate the 2D DNA arrays from the 3D crystal, which is an analog to the exfoliation of graphene from graphite. However, when the crystal was exposed to low ionic strength, instead of exfoliation, we observed an unexpected expansion along the exfoliation direction. The crystal expansion was highly reversible by controlling with EDTA and Mg^{2+} for seven cycles (Figure 4-5). During the expansion and contraction, wrinkles and large cracks formed during the transition, and then self-healed at the fully expanded or contracted state. The critical ionic strength for crystal exfoliation to happen was found to be 30~50 mM NaCl.

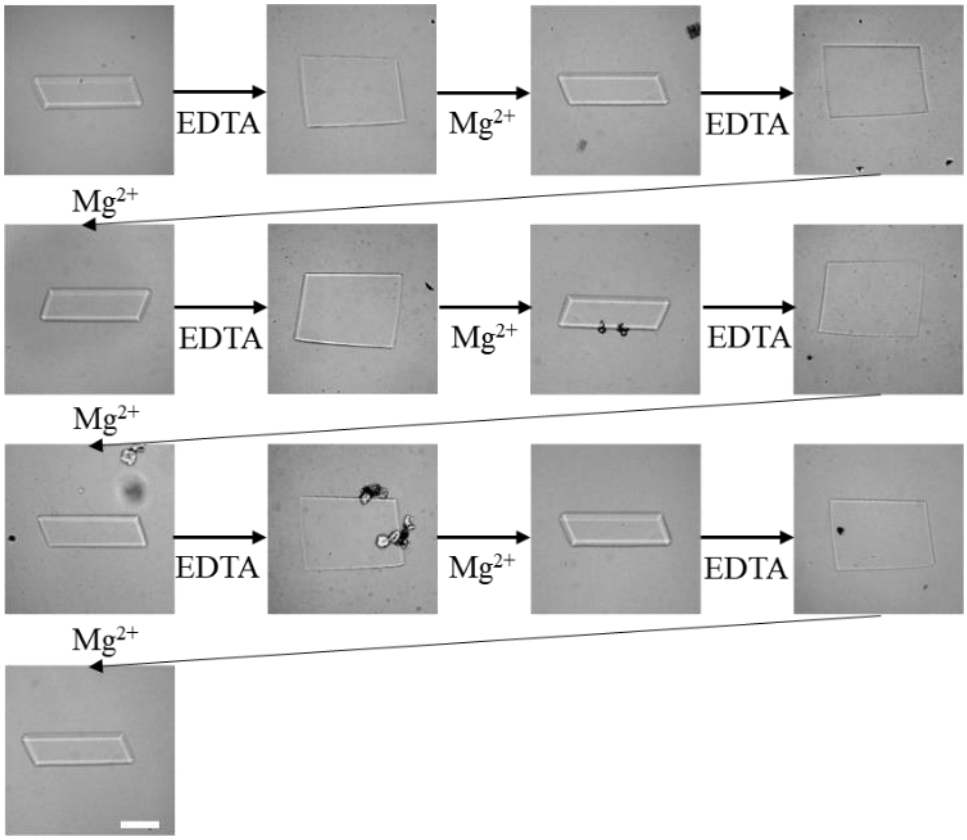

Figure 4-5 Expansion of 2D Ligated DNA aΔ^{4T} Crystals in Response to Ionic Strength. Scale bar: 100 μm.

Based on our observation, we proposed a “crack formation” hypothesis and attributed the expansion as a result of abundant nano-sized cracks from the stochastic breaking of sticky end

interaction (Figure 4-6). The crack formation mechanism consists of several steps. 1: Original 2D ligated crystal at high ionic strength (> 50 mM NaCl); 2: At low ionic strength (<30 mM NaCl), cracks formed in the crystal because of the weakening of sticky end interaction and the electronic repulsion from DNA phosphate backbone; 3. Cracks grow large until they meet with each other, and bump up the meeting region; 4: Along the vertical direction, cracks shift and rearrange to release the strain from neighboring cracks; 5: Cracks gradually rearrange to optimal positions where strain is released and the "bumped up" regions self-heal to be smooth and flat. Crystals continue to expand until the elastic force to restrict cracking and electrostatic repulsion reach a force equilibrium. The cracks arrangement may end up being similar to a "kirigami" pattern (a Japanese paper art) where the strain can be minimized. From 5 back to 1, the cracks are healed when the sticky ends between layers are reannealed at enough ionic strength. By AFM imaging, we found cracked layers as proposed on the expanded crystal (Figure 4-7).

Similar to the interaction between DNA origami structures[52], it is reasonable that the interactions between neighboring ligated 2D layers have been strengthened by the millions of 2-bp sticky ends. The strong multivalent interactions make the 2D layers hard to fully dissociate. Compared with previously reported expandable ferritin crystals transfused with polymer gels[37], our expandable DNA crystal is basing on very different expansion mechanism, and the expansion can specifically happen along the designed dimension of the crystal.

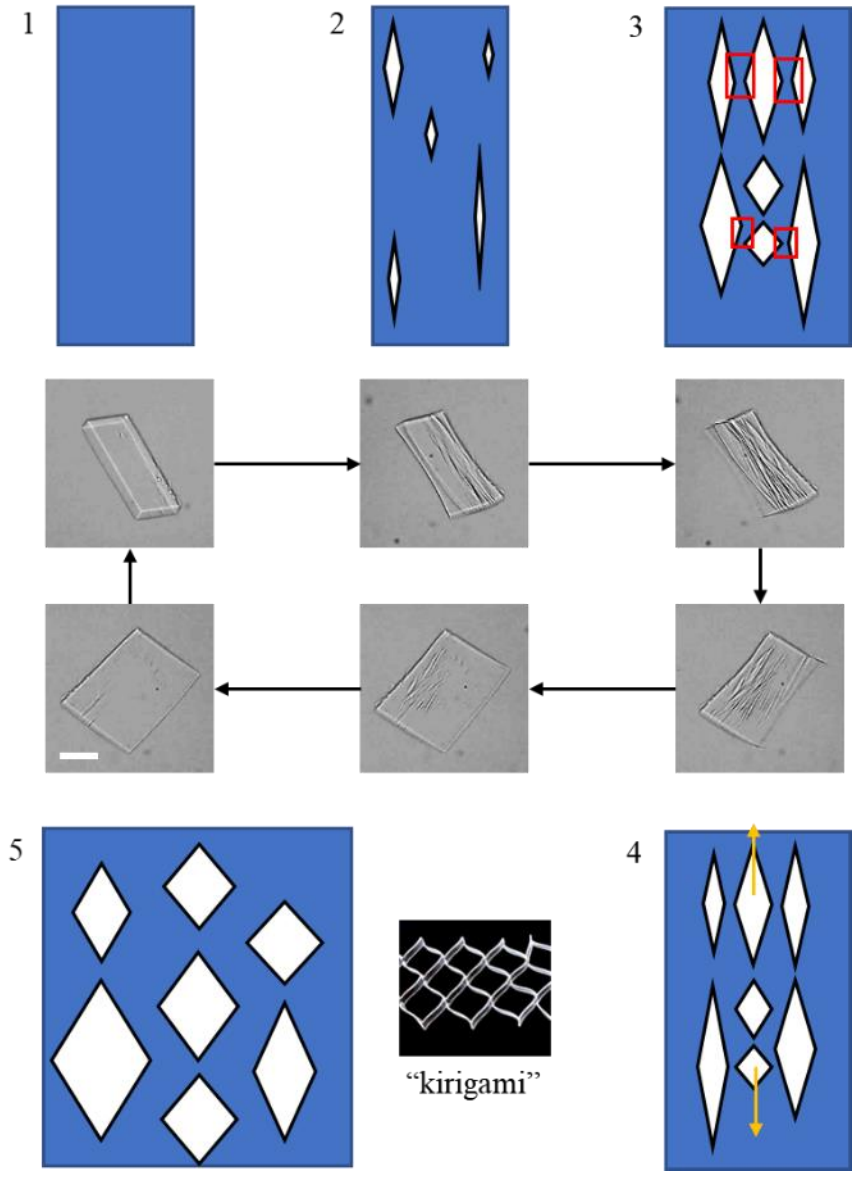

Figure 4-6 Crack Formation Mechanism for the Expansion of 2D Ligated DNA $a\Delta^{4T}$ DNA Crystal. Scale bar: 100 µm.

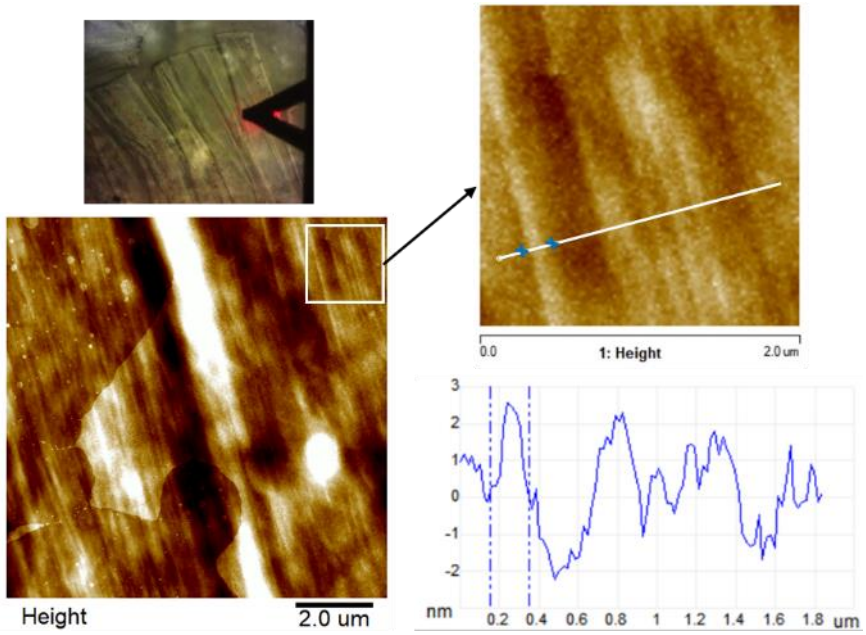

Figure 4-7 AFM Characterization of Expanded DNA Crystal

4.4.4 Exfoliation of Microtubes from 3D DNA Crystal

A revised crystal design which consists of two different DNA triangle layers was used for exfoliation study (Figure 4-8). In the design, the triangle EX can be ligated along two directions, while triangle EY cannot be ligated at any sticky ends. We hypothesize that when such a crystal is dissociated at low ionic strength, EY triangles can easily dissociate into the solution because of entropy, leaving the 2D layers covalently linked from EX layers exfoliated. Moreover, since the sticky ends above and below the EX 2D layers are not compatible with each other, they will not stick to each other as in the design from single DNA triangle. In experiment, when the crystal was looped into water, it opened up into countless slices as an open book (Figure 4-9). Some pipetting was applied to mechanically help the dissociation, and bunches of linear structures of similar length were obtained. By TEM and AFM imaging we further confirmed that these are microtubes coiled from DNA 2D layers (Figure 4-10, 4-11). The results demonstrated that exfoliation was successfully achieved, and the 2D layers possibly coiled up because of the internal strain when motifs were covalently linked.

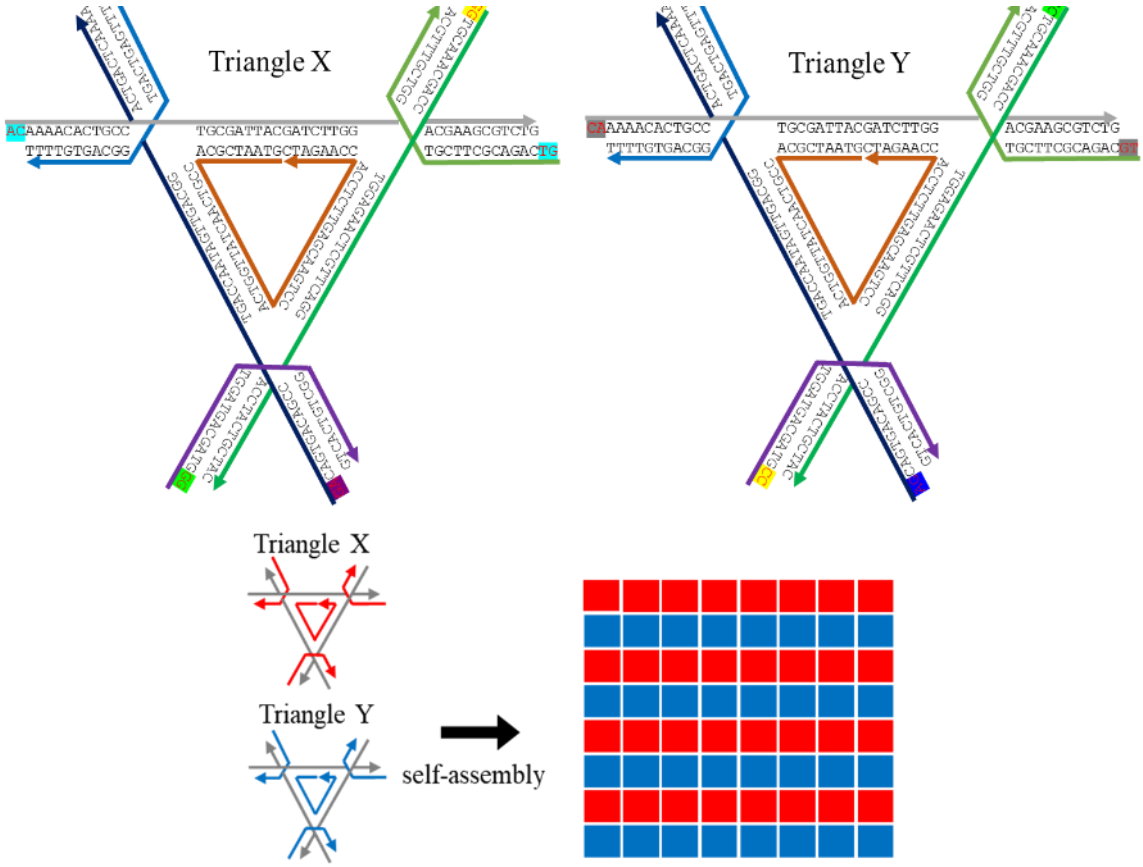

Figure 4-8 Schematic Design of DNA Triangles X, Y for 2D Alternative Self-assembly of DNA Crystals

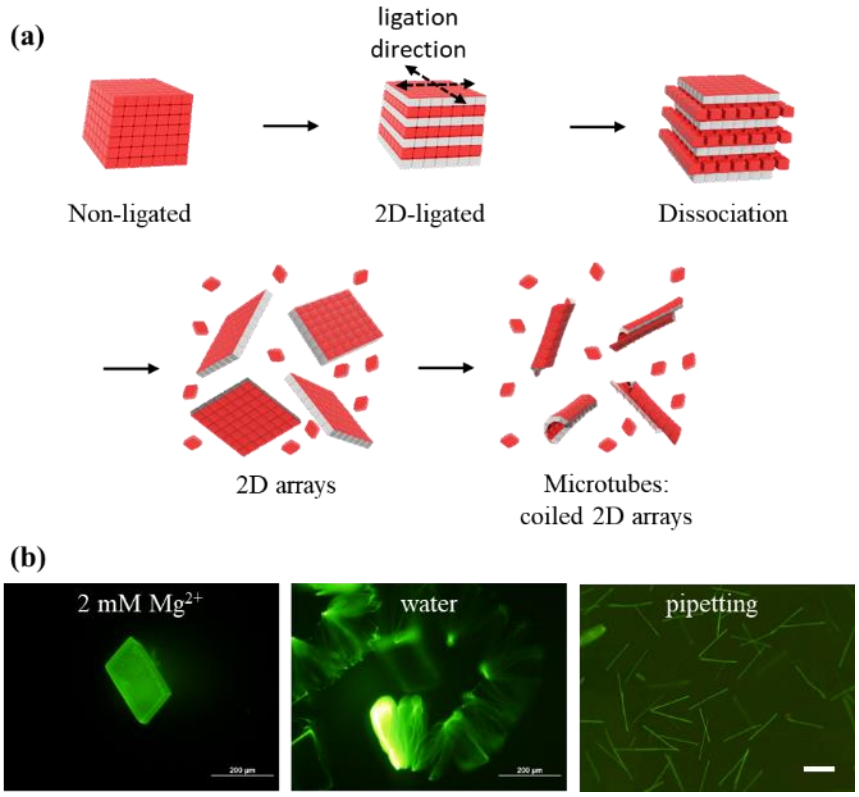

Figure 4-9 Schematic Drawing and Fluorescence Images of DNA Microtubes Exfoliated from 2D Ligated DNA $a\Delta^{4T}$ Crystals. Scale bar: 100 μm.

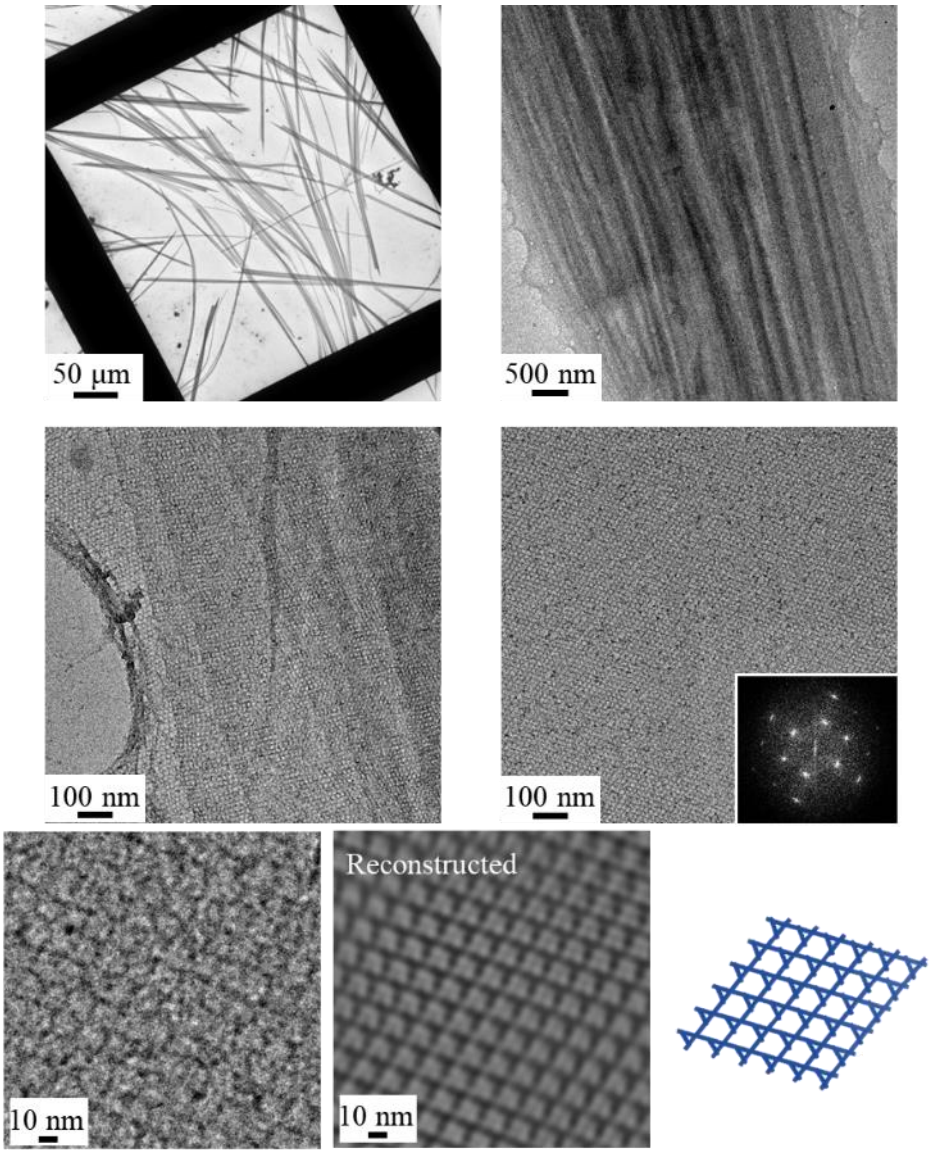

Figure 4-10 TEM Imaging of Exfoliated DNA Microtubes

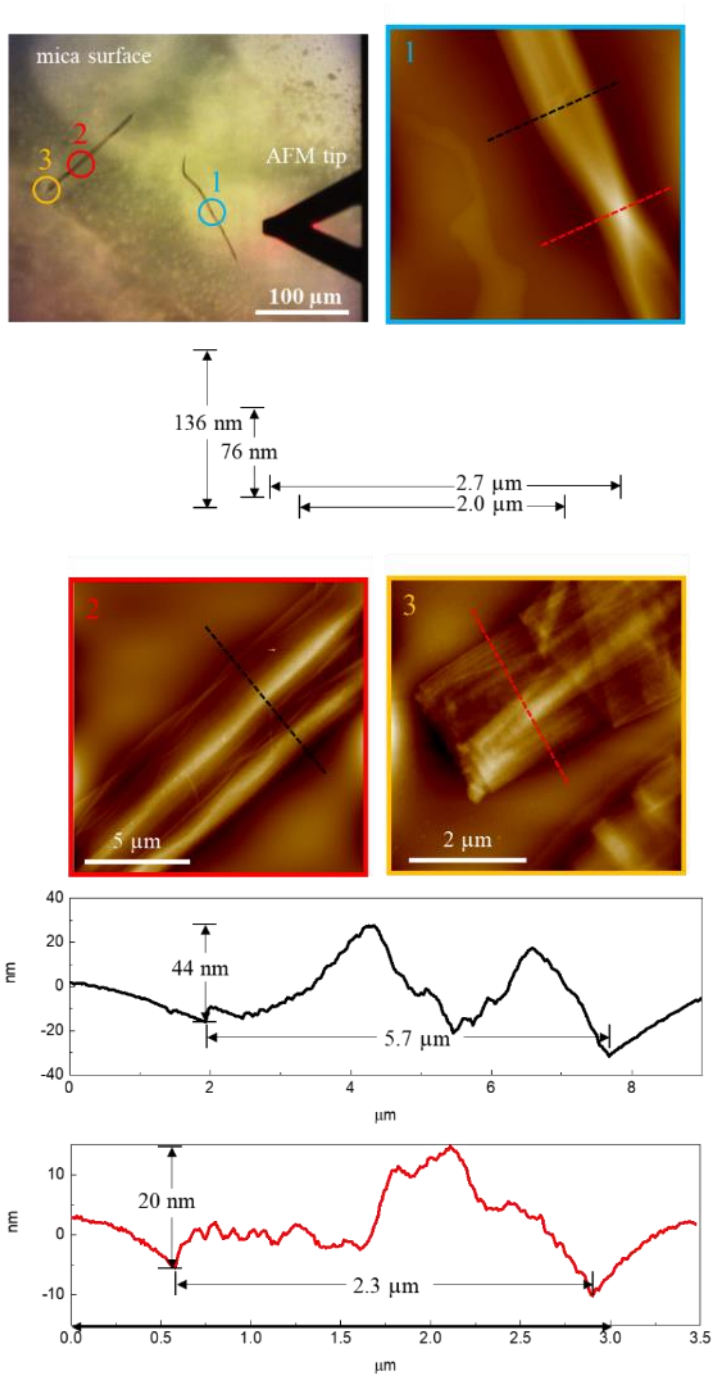

Figure 4-11 AFM Images in Air of Exfoliated DNA Microtubes

4.4.5 Preparation of DNA Crystals with Shell Morphology

Ligation was controlled spatially for producing crystals with complex morphologies. For the ligation of DNA $s\Delta^{4T}$ crystals under current conditions, if the ligation time is shortened to 8~10 mins of ligation, followed by quick dissolution in water for regions that are not yet ligated, the morphology of a DNA crystal shell can be obtained. The inner spherical profile of the crystal shell is potentially the diffusion front of DNA ligase when they go inside the crystal from the periphery. Combing this spatially selective ligation and macros-seeding, we successfully prepared more complicated crystal morphologies such as yolk-shell and multi-shell crystals. This is the first time that these morphologies have been realized for DNA crystals.

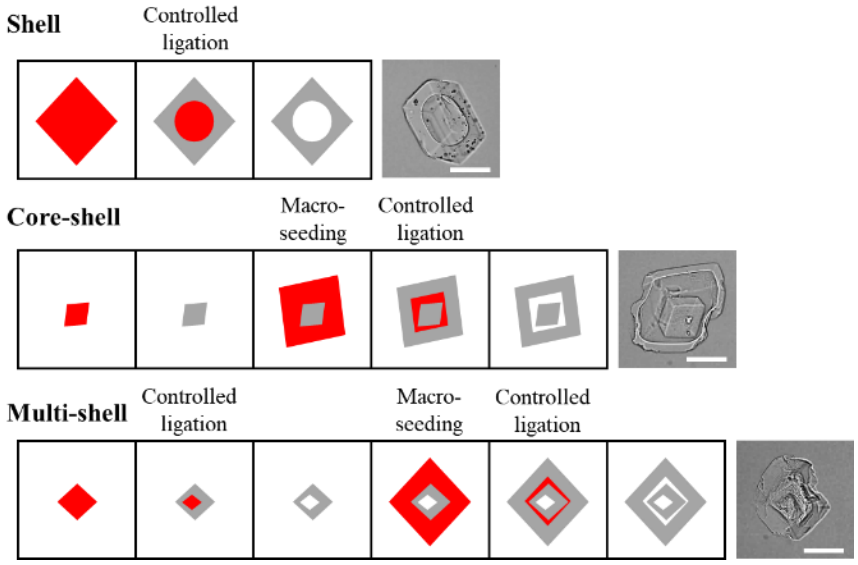

Figure 4-12 Preparation of DNA Crystals with Shell Morphology. Scale bar: 100 μm.

4.5 Conclusions

We demonstrated the preparation of new DNA nanomaterials by directional and spatial post-assembly ligation in engineered 3D DNA crystals. The combination of weak sticky-ended cohesions and the strong covalent bonds is the key for such preparation. 1D DNA chains, DNA microtubes, 3D DNA crystals with complex architectures, as well as reversibly expandable, self-healing DNA crystals were obtained. These new DNA materials derived from engineered 3D DNA crystals are promising candidates for applications such as drug delivery, drug encapsulation and release, and chemical switches.

CHAPTER 5. MODULATING THE SELF-ASSEMBLY OF DNA CRYSTALS BY 5'-PHOSPHORYLATION

5.1 Introduction

With recent successful designs of 3D DNA crystals[17–20], there is a strong need for the development of approaches to control their crystallization habit, such as the required ionic strength for crystallization, crystallization kinetics and the crystal morphology, to meet complicated applications. One current approach is to design specific blocking strands to slow down the crystallization kinetics of the DNA crystals[24,25]. This approach has obtained different crystal morphologies as well as larger crystals with modestly higher resolution. In contrast to slowing down the crystallization, here we report another approach to speed up DNA crystallization kinetics. We found that 5'-phosphorylation of DNA sticky ends at the crystal contacts can speed up the self-assembly process in multiple DNA crystal designs, including DNA tensegrity triangle crystals as well as a crystal from DNA duplex. With 5'-phosphorylation, the crystallization of DNA tensegrity triangle crystals can happen at much lower ionic strength, and the crystal morphologies can be finely tuned by selectively enhancing the crystallization kinetics on certain directions. With this approach, we can now better tune the kinetics of DNA crystallization.

5.2 Designs and Schemes

Previously, it was reported that 5'-phosphorylation of DNA tensegrity triangle could improve the X-ray diffraction resolution of the DNA crystals[53]. During the development of the post-assembly ligation, we unexpectedly observed an enhanced crystallization kinetics of the phosphorylated DNA triangle $s\Delta^{4T}$ in the TAE/Mg^{2+} buffer system (Figure 5-1). Therefore, based on our observation, we hypothesized that 5'-phosphorylation could promote the self-assembly of DNA triangular motifs. We further tested this idea by the crystallization kinetics of DNA crystal $s\Delta^{2T}$ and $s\Delta^{3T}$ (design schemes in Figure 3-10 and Figure 3-12). In an asymmetric DNA crystal $a\Delta^{4T}$ (Figure 4-2), we hypothesized that selective phosphorylation in certain directions of the crystal can promote the crystal self-assembly along selected directions, which will in turn change the crystal morphology.

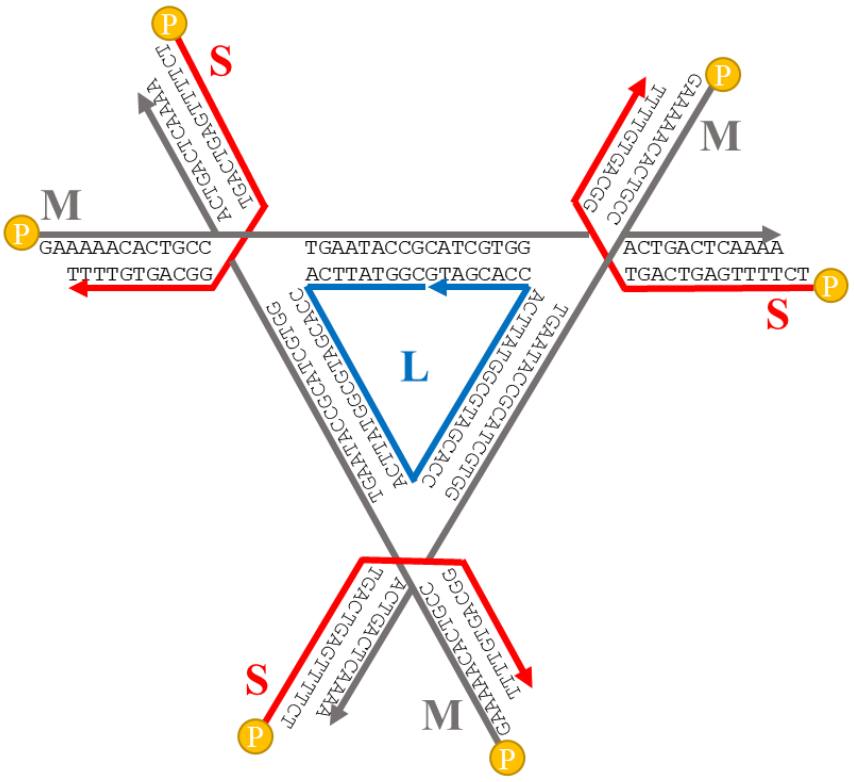

Figure 5-1 Design Scheme of DNA $s\Delta^{4T}$ and Potential Phosphorylation Sites

5.3 Materials and Methods

5.3.1 DNA Oligonucleotides

In addition to 4.3.1, extra strands:

309D, 10 nt: 5'- CGACGATCGT-3'

5.3.2 Crystallization of DNA Triangle Crystals

For the crystallization of $s\Delta^{4T}$, DNA strands were combined at designed ratio in 0.2×, 0.5, or 1×TAE/Mg^{2+} buffer by slowly cooling the DNA solution from 95 ºC to 22 ºC in 2 hours. The final triangle motif concentration is 2 μM. 5 μL of assembled DNA triangle solution was incubated against 600 μL of 1× to 10 ×TAE/Mg^{2+} solution in a hanging-drop setup at 22 °C for two weeks. For other designs, different drop buffers and reservoir buffers are specified in the discussion section. The crystal morphology was examined by optical microscopy (OLYMPUS, BX51).

5.3.3 Crystallization of DNA Duplex Crystal

The 10-nt self-complementary DNA strand 309D (PDB: 309D) was diluted to 0.5~2 mM in water, and then mixed with equal volume of Natrix/Natrix2 crystallization screens (Hampton) for the hanging drop crystallization setup. The corresponding precipitants according to Natrix/Natrix2 formulations were applied as reservoir buffer. Crystallization states were examined by optical microscopy (OLYMPUS, BX51).

5.4 Results and Discussions

5.4.1 Crystallization Diagram of DNA sΔ^{4T} Crystal

We used the sΔ^{4T} crystal as a system to extensively explore the crystallization diagram. Results revealed that 5'- phosphorylation can promote the crystallization at low ionic strength where original triangle motifs cannot crystallize. Three different motifs to buffer ratios were used in the hanging drop, while they were incubated against a sequence of increasing concentration of reservoir buffer. Four combinations were screened: no phosphorylation (T-0), only phosphorylation on M strand (T-pM), only phosphorylation on S strand (T-pS) and phosphorylation on both L and S (T-pMS). The aim is to find out the critical condition for crystallization to happen, thus the solubility line. The results of the screening are presented in crystallization diagrams as shown in Figure 5-2. For the samples starting from identical drop condition, their representing data points will end up on the same line in the diagram. The solubility line is conceptually demonstrated by crossing the gaps between crystallization and clear drop conditions. From the diagrams, we can observe a clear trend that the solubility line is moving towards lower motif and buffer concentration from T-0 to T-pM /T-pS and T-pMS. While the lowest motif and buffer concentration are identified as 32 μM and 5×TAE/Mg^{2+} for the crystallization of T-0, after 5'-phosphorylation of M and S, the crystallization of T-pMS can happen at 2 μM concentration in 1×TAE/Mg^{2+} buffer (Figure 5-3). The phosphorylation of the L strand has very little effect on the crystallization kinetics, possibly because the modification site is far away from crystal contacts.

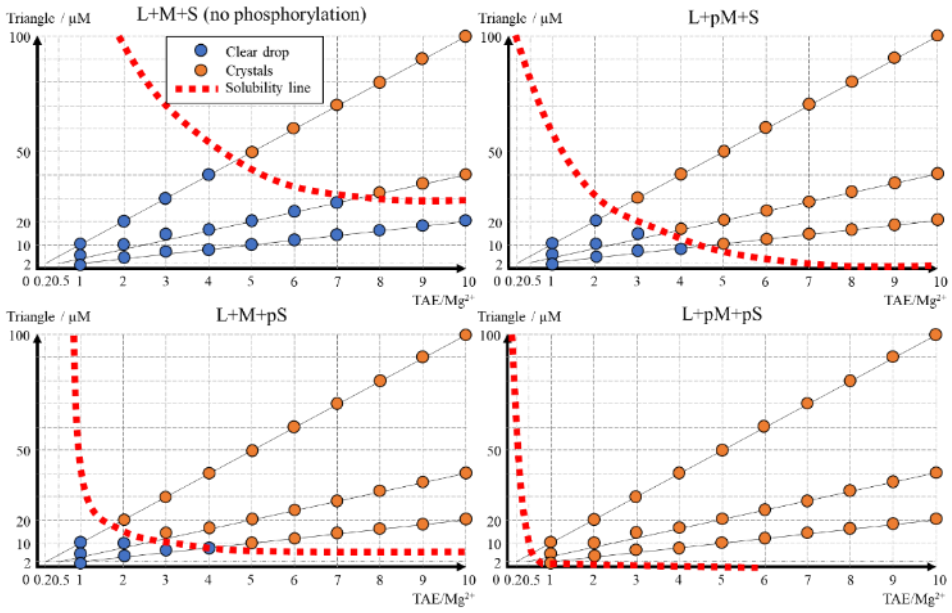

Figure 5-2 Crystallization Diagram of DNA sΔ^{4T} with Different Phosphorylation Sites

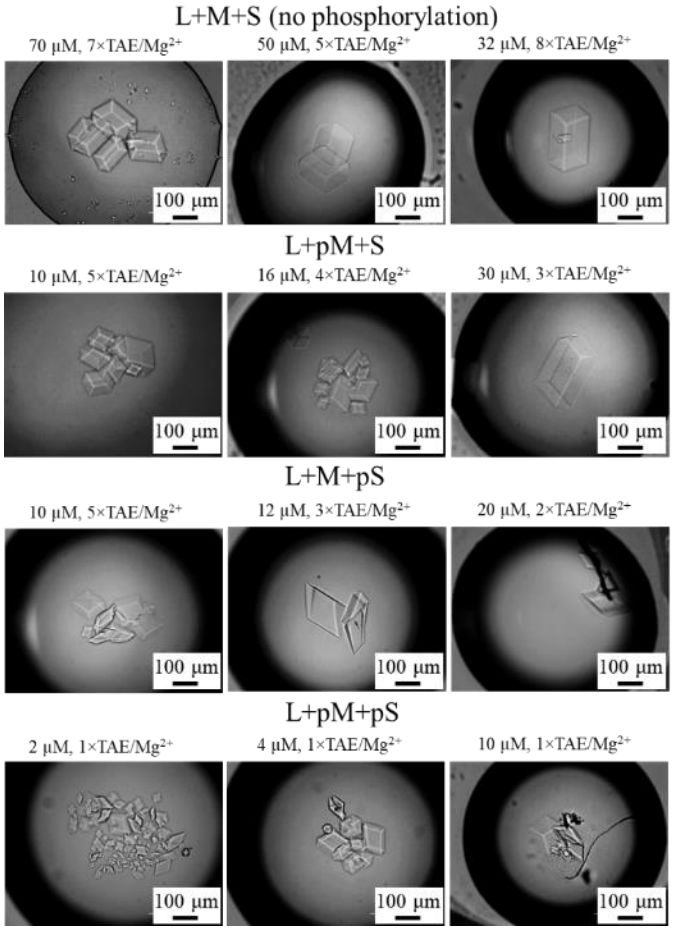

Figure 5-3 Optical Images of DNA sΔ^{4T} Crystals with Different Phosphorylation Sites

5.4.2 Selectively Phosphorylation in DNA aΔ^{4T} Crystal

Nucleation and crystal growth are two major steps in crystallization. The experiments in DNA sΔ^{4T} Crystal demonstrates that the crystal nucleation can be promoted by 5'phosphorylation. Here we used the DNA aΔ^{4T} crystal to study the effect of phosphorylation on crystal growth. 5'phosphorylation was applied in selected pairs of sticky ends, and we did observe evident change in DNA crystal morphology with different combinations of phosphorylation sites (Figure 5-4). The crystals maintain the angles in rhombohedral morphology, while the relative length on the three crystallographic axes changed sharply.

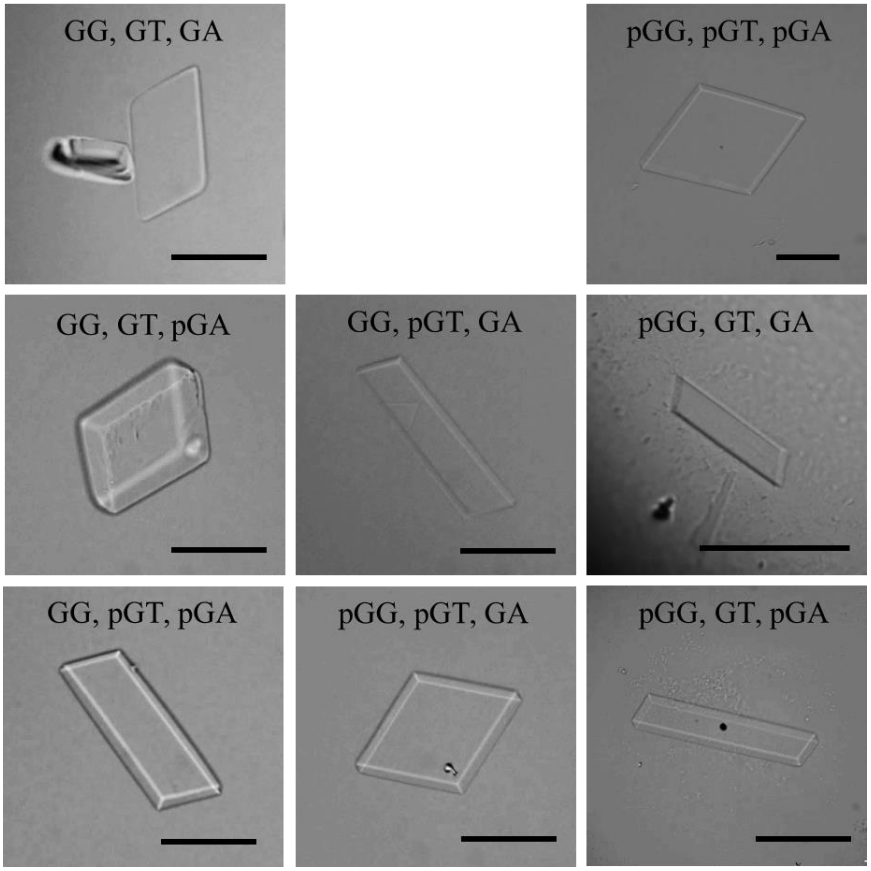

Figure 5-4 Optical Images of DNA aΔ^{4T} Crystals with Different Phosphorylation Sites. Scale bar: 100 μm. The three pairs of sticky ends are marked on images, and the "p" prefix means the sticky ends are phosphorylated.

Data analysis of the crystal morphology proved that crystal growth is also enhanced by 5'-phosphorylation. Since we have no evidence how the sticky ends correspond to the crystal axes, we measured the crystal dimension in each design, and mathematically fit the length to the growth

rate of each sticky end. We assume that there are 6 different growth rates for the six different sticky ends: GG, GT, GA, pGG, pGT, pGA (The sticky ends are represented by only one overhang, and "p" prefix means phosphorylated). Then their values were tried as integers from 1:1:1:1:1:1 to 20:20:20:20:20:20, and the set of value that can best fit the experimental data was selected. The best fitting result turns out as GG:GT:GA:pGG:pGT:pGA=6:4:3:20:18:2. Further macro-seeding experiment proved that the shortest dimension in aΔ^{4T} crystals is from GA base pairs, which is consistent with the fitting results. Moreover, we can also tell from the value that the crystal growth along GG and GT directions were speeded up for 3~4 times after phosphorylation. This agrees with our hypothesis. The trend is not clear for GA and pGA sticky ends, possibly because of the dimension is very short and there is significant variance in measurement. Based on these results we demonstrate a morphology evolution process for the aΔ^{4T} crystal with stepwise increase of phosphorylated strands. We found that when only one overhang in the sticky end is phosphorylated, the crystallization kinetics fall between no phosphorylation and full phosphorylation. This result can be applied for the fine-tuning of crystal growth kinetics.

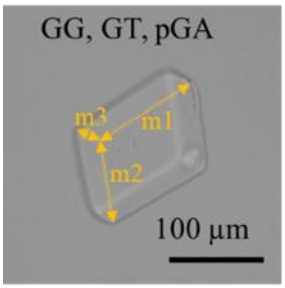

$$l1 = m1$$
$$l2 = m2$$
$$l3 = \frac{m3}{\cos(50°)}$$

Crystal Type	length 1/ µm	length 2/ µm	length 3/ µm
GG, GT, GA	127	75	5
GG, GT, pGA	116	90	39
GG, pGT, GA	193	46	12
pGG, GT, GA	86	23	8
GG, pGT, pGA	173	61	20
pGG, pGT, GA	117	111	19
pGG, GT, pGA	180	33	16
pGG, pGT, pGA	172	158	17

Figure 5-5 Measurement of DNA aΔ^{4T} Crystals Dimensions from Optical Images

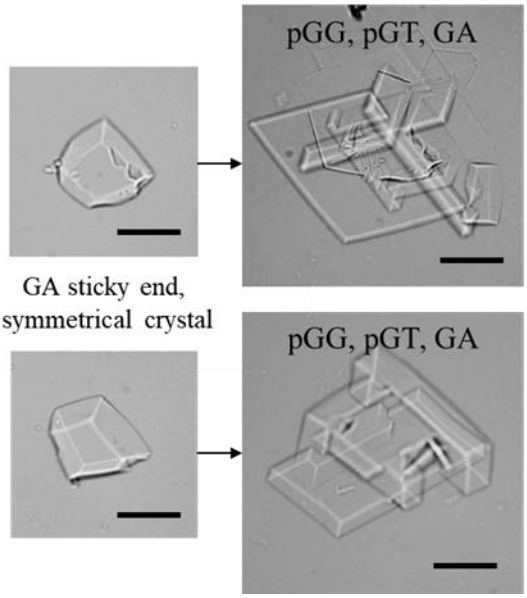

Figure 5-6 Macro-seeding Experiment to Identify Sticky End Direction. Scale bar: 100 μm.

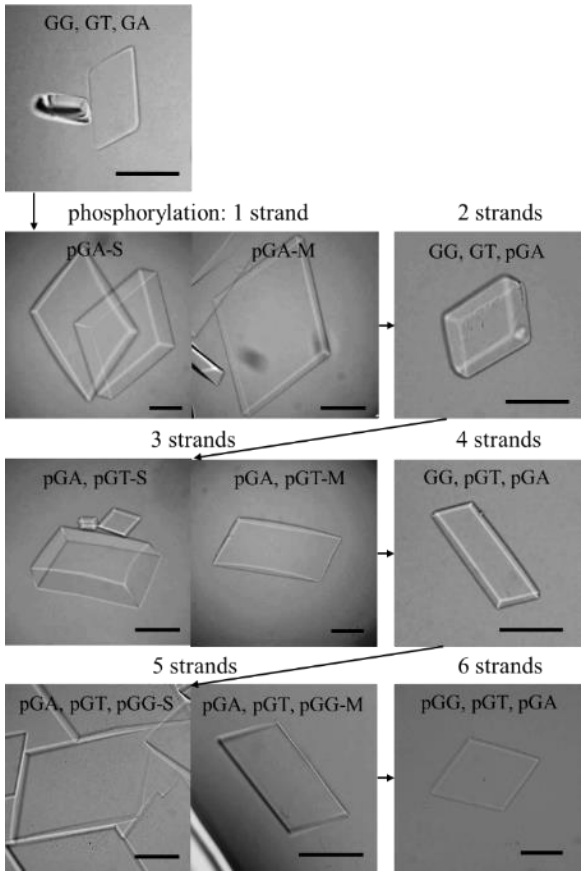

Figure 5-7 Morphology Evolution of DNA aΔ^{4T} Crystals with Stepwise Increased Phosphorylation Sites. Scale bar: 100 μm.

5.4.3 5’-Phosphorylation in Other DNA Crystals

Similar modulation in crystallization kinetics was also observed for DNA $s\Delta^{2T}$ and $s\Delta^{3T}$ crystals (Figure 5-8, Figure 5-9). For example, original $s\Delta^{2T}$ triangles did not crystallize when the reservoir buffer concentration was lower than 10×TAE/Mg^{2+}, and the phosphorylated $s\Delta^{2T}$ crystallized when the reservoir buffer was only 3×TAE/Mg^{2+}.

Reservoir buffer: TAE/Mg^{2+}	3×	5×	10×	20×
Native	clear	clear	clear	crystals, ~50 μm
Phosphorylation	crystals, ~10 μm	crystals, ~10 μm	crystals, ~10 μm	crystals, ~10 μm

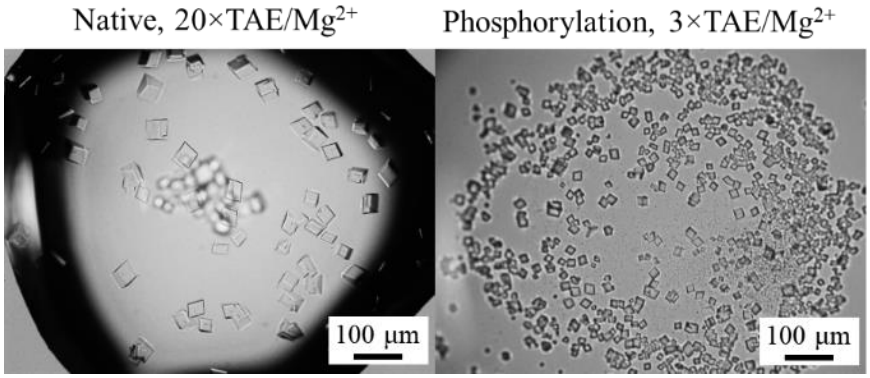

Figure 5-8 Crystallization Screening for DNA $s\Delta^{2T}$ with and without Phosphorylation

Reservoir buffer: TAE/Mg^{2+}	1.5×	2×	3×	5×
Native	clear	clear	clear	crystals
Phosphorylation	crystals	crystals	crystals	crystals

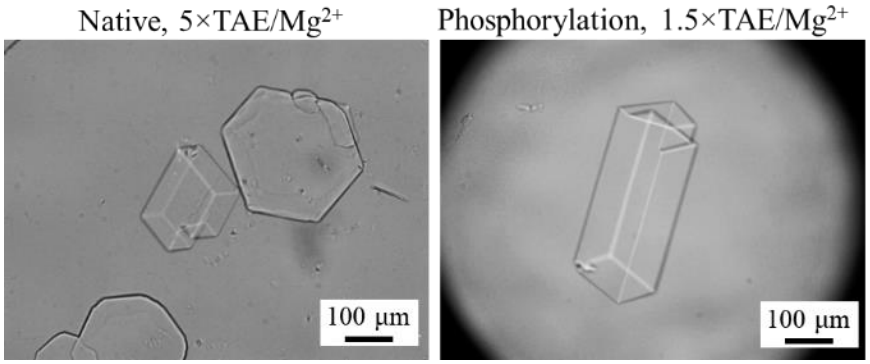

Figure 5-9 Crystallization Screening for DNA $s\Delta^{3T}$ with and without Phosphorylation

In a DNA crystal assembled from from DNA duplex by sticky-ended cohesion, 5'-phosphorylation can also modulate its crystallization behavior (Figure 5-10). In a crystallization screening, 309DP, the duplex with 5'-phosphorylation, demonstrated much stronger tendency to interact than the 309D duplex without phosphorylation. The comparison can be made for the two versions at the same crystallization buffer condition. Despite the conditions where both strands behaved similarly, 309DP strand aggregated while 309D formed crystals, and 309DP formed crystals or aggregated while the 309D drop was still clear. From the screening results, we can conclude that 5'-phosphorylation has enhanced the interaction between DNA duplex motifs.

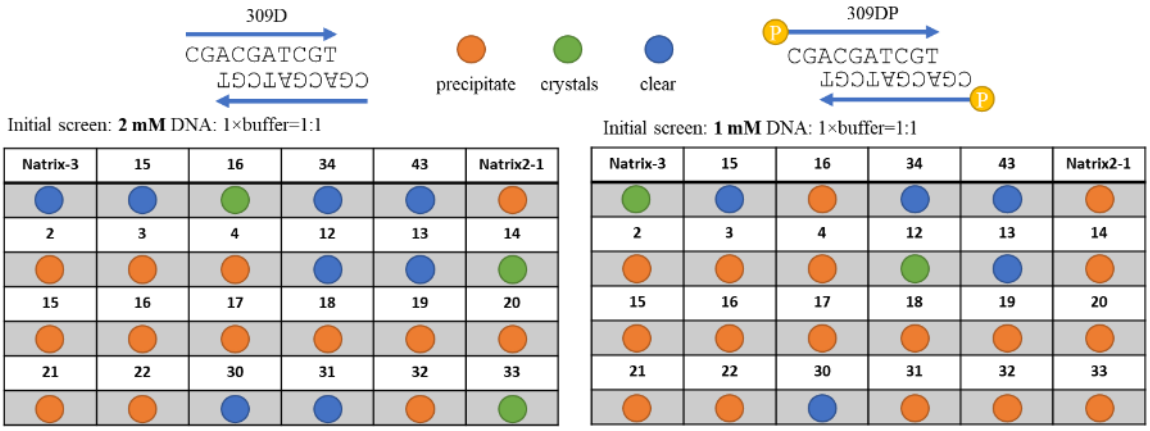

Figure 5-10 Crystallization Screening for DNA Duplex Crystals with and without Phosphorylation

5.5 Conclusions

5'-phosphorylation can speed up the crystallization kinetics of DNA tensegrity triangle motifs. Experimental data showed that both the crystal nucleation and the crystal growth were promoted after the sticky ends at the crystal contacts were phosphorylated. With such modulation, we can now obtain DNA crystals at much lower ionic strength, and finely tune the crystal morphology by selective phosphorylation (Figure 5-11). Our finding will serve a useful tool to engineer the self-assembly kinetics of DNA crystals.

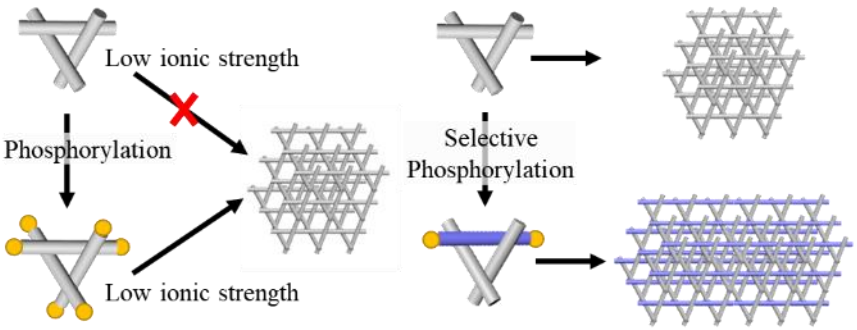

Figure 5-11 Scheme of Modulated DNA Crystal Self-assembly by 5'-Phosphorylation

REFERENCES

(1) Seeman, N. C. *Structural DNA Nanotechnology*; Cambridge University Press, 2015.

(2) Seeman, N. C. Nanomaterials Based on DNA. *Biochemistry* **2010**, *79*, 65–87.

(3) Kallenbach, N. R.; Ma, R.-I.; Seeman, N. C. An Immobile Nucleic Acid Junction Constructed from Oligonucleotides. *Nature* **1983**, *305* (5937), 305829a0.

(4) Wang, X.; Seeman, N. C. Assembly and Characterization of 8-Arm and 12-Arm DNA Branched Junctions. *J. Am. Chem. Soc.* **2007**, *129* (26), 8169–8176.

(5) Seeman, N. C. DNA Nicks and Nodes and Nanotechnology. *Nano Lett.* **2001**, *1* (1), 22–26.

(6) Winfree, E.; Liu, F.; Wenzler, L. A.; Seeman, N. C. Design and Self-Assembly of Two-Dimensional DNA Crystals. *Nature* **1998**, *394* (6693), 539.

(7) Seeman, N. C. DNA in a Material World. *Nature* **2003**, *421* (6921), 427–431.

(8) He, Y.; Chen, Y.; Liu, H.; Ribbe, A. E.; Mao, C. Self-Assembly of Hexagonal DNA Two-Dimensional (2D) Arrays. *J. Am. Chem. Soc.* **2005**, *127* (35), 12202–12203.

(9) He, Y.; Tian, Y.; Ribbe, A. E.; Mao, C. Highly Connected Two-Dimensional Crystals of DNA Six-Point-Stars. *J. Am. Chem. Soc.* **2006**, *128* (50), 15978–15979.

(10) Zhang, C.; Su, M.; He, Y.; Zhao, X.; Fang, P. A.; Ribbe, A. E.; Jiang, W.; Mao, C. Conformational Flexibility Facilitates Self-Assembly of Complex DNA Nanostructures. *PNAS* **2008**, *105* (31), 10665–10669.

(11) He, Y.; Ye, T.; Su, M.; Zhang, C.; Ribbe, A. E.; Jiang, W.; Mao, C. Hierarchical Self-Assembly of DNA into Symmetric Supramolecular Polyhedra. *Nature* **2008**, *452* (7184), 198–201.

(12) Zhang, C.; Wu, W.; Li, X.; Tian, C.; Qian, H.; Wang, G.; Jiang, W.; Mao, C. Controlling the Chirality of DNA Nanocages. *Angew. Chem. Int. Ed.* **2012**, *51* (32), 7999–8002.

(13) Chandrasekaran, A.; Zhuo, R. A 'Tile' Tale: Hierarchical Self-Assembly of DNA Lattices. *Appl. Mater. Today* **2016**, *2*.

(14) Rothemund, P. W. Folding DNA to Create Nanoscale Shapes and Patterns. *Nature* **2006**, *440* (7082), 297–302.

(15) Wei, B.; Dai, M.; Yin, P. Complex Shapes Self-Assembled from Single-Stranded DNA Tiles. *Nature* **2012**, *485* (7400), 623–626.

(16) Seeman, N. A Conversation with Prof. Ned Seeman: Founder of DNA Nanotechnology. Interview by Paul S. Weiss. *ACS nano* **2008**, *2* (6), 1089–1096.

(17) Zheng, J.; Birktoft, J. J.; Chen, Y.; Wang, T.; Sha, R.; Constantinou, P. E.; Ginell, S. L.; Mao, C.; Seeman, N. C. From Molecular to Macroscopic via the Rational Design of a Self-Assembled 3D DNA Crystal. *Nature* **2009**, *461* (7260), 74–77.

(18) Zhang, F.; Simmons, C. R.; Gates, J.; Liu, Y.; Yan, H. Self-Assembly of a 3D DNA Crystal Structure with Rationally Designed Six-Fold Symmetry. *Angew. Chem. Int. Ed.* **2018**. *57* (38), 12504-12507.

(19) Simmons, C. R.; Zhang, F.; MacCulloch, T.; Fahmi, N.; Stephanopoulos, N.; Liu, Y.; Seeman, N. C.; Yan, H. Tuning the Cavity Size and Chirality of Self-Assembling 3D DNA Crystals. *J. Am. Chem. Soc.* **2017**, *139* (32), 11254–11260.

(20) Hong, F.; Jiang, S.; Lan, X.; Narayanan, R.; Šulc, P.; Zhang, F.; Liu, Y.; Yan, H. Layered-Crossover Tiles with Precisely Tunable Angles for 2D and 3D DNA Crystal Engineering. *J. Am. Chem. Soc.* **2018**, *140* (44), 14670–14676.

(21) Paukstelis, P. J.; Nowakowski, J.; Birktoft, J. J.; Seeman, N. C. Crystal Structure of a Continuous Three-Dimensional DNA Lattice. *Chemistry & Biology* **2004**, *11* (8), 1119–1126.

(22) Brady, R.; Brooks, N. J.; Cicuta, P.; Michele, L. Crystallization of Amphiphilic DNA C-Stars. *Nano Lett.* **2017**, *17* (5), 3276-3281.

(23) McNeil, R.; Paukstelis, P. J. Core-Shell and Layer-by-Layer Assembly of 3D DNA Crystals. *Adv. Mater.* **2017**, *29* (28), 1701019.

(24) Zhang, D.; Paukstelis, P. J. Designed DNA Crystal Habit Modifiers. *J. Am. Chem. Soc.* **2017**, *139* (5), 1782–1785.

(25) Zhao, J.; Zhao, Y.; Li, Z.; Wang, Y.; Sha, R.; Seeman, N. C.; Mao, C. Modulating Self-Assembly of DNA Crystals with Rationally Designed Agents. *Angew. Chem. Int. Ed.* **2018**, *57* (50), 16529–16532.

(26) Zhao, J.; Chandrasekaran, A.; Li, Q.; Li, X.; Sha, R.; Seeman, N. C.; Mao, C. Post-Assembly Stabilization of Rationally Designed DNA Crystals. *Angew. Chem. Int. Ed.* **2015**, *54* (34), 9936–9939.

(27) Abdallah, H. O.; Ohayon, Y. P.; Chandrasekaran, A. R.; Sha, R.; Fox, K. R.; Brown, T.; Rusling, D. A.; Mao, C.; Seeman, N. C. Stabilisation of Self-Assembled DNA Crystals by Triplex-Directed Photo-Cross-Linking. *Chem. Comm.* **2016**, *52* (51), 8014–8017.

(28) Zhang, D.; Paukstelis, P. J. Enhancing DNA Crystal Durability through Chemical Crosslinking. *Chembiochem* **2016**, *17* (12), 1163–1170.

(29) Paukstelis, P. J.; Seeman, N. C. 3D DNA Crystals and Nanotechnology. *Crystals* **2016**, *6* (8), 97.

(30) Yan, E.-K. K.; Lu, Q.-Q. Q.; Zhang, C.-Y. Y.; Liu, Y.-L. L.; He, J.; Chen, D.; Wang, B.; Zhou, R.-B. B.; Wu, P.; Yin, D.-C. C. Preparation of Cross-Linked Hen-Egg White Lysozyme Crystals Free of Cracks. *Sci. Rep.* **2016**, *6*, 34770.

(31) Kowalski, A. E.; Huber, T. R.; Ni, T. W.; Hartje, L. F.; Appel, K. L.; Yost, J. W.; Ackerson, C. J.; Snow, C. D. Gold Nanoparticle Capture within Protein Crystal Scaffolds. *Nanoscale* **2016**, *8* (25), 12693–12696.

(32) Huber, T. R.; Hartje, L. F.; McPherson, E. C.; Kowalski, A. E.; Snow, C. D. Programmed Assembly of Host-Guest Protein Crystals. *Small* **2016**, *13* (7), 1602703.

(33) Kowalski, A. E.; Johnson, L. B.; Dierl, H. K.; Park, S.; Huber, T. R.; Snow, C. D. Porous Protein Crystals as Scaffolds for Enzyme Immobilization. *Biomater. Sci.* **2019**. Advance Article.

(34) Hartje, L. F.; Bui, H. T.; Andales, D. A.; James, S. P.; Huber, T. R.; Snow, C. D. Characterizing the Cytocompatibility of Various Cross-Linking Chemistries for the Production of Biostable Large-Pore Protein Crystal Materials. *ACS Biomater. Sci. Eng.* **2018**, *4* (3), 826–831.

(35) Guli, M.; Lambert, E. M.; Li, M.; Mann, S. Template-Directed Synthesis of Nanoplasmonic Arrays by Intracrystalline Metalization of Cross-Linked Lysozyme Crystals. *Angew. Chem. Int. Ed.* **2010**, *49* (3), 520–523.

(36) England, M. W.; Lambert, E. M.; Li, M.; Turyanska, L.; Patil, A. J.; Mann, S. Fabrication of Polypyrrole Nano-Arrays in Lysozyme Single Crystals. *Nanoscale* **2012**, *4* (21), 6710–6713.

(37) Zhang, L.; Bailey, J. B.; Subramanian, R. H.; Groisman, A.; Tezcan, A. F. Hyperexpandable, Self-Healing Macromolecular Crystals with Integrated Polymer Networks. *Nature* **2018**, *557* (7703), 86–91.

(38) Abe, S.; Maity, B.; Ueno, T. Design of a Confined Environment Using Protein Cages and Crystals for the Development of Biohybrid Materials. *Chem. Comm.* **2016**, *52* (39), 6496–6512.

(39) Geng, C.; Paukstelis, P. J. DNA Crystals as Vehicles for Biocatalysis. *J. Am. Chem. Soc.* **2014**, *136* (22), 7817–7820.

(40) Hao, Y.; Kristiansen, M.; Sha, R.; Birktoft, J. J.; Hernandez, C.; Mao, C.; Seeman, N. C. A Device That Operates within a Self-Assembled 3D DNA Crystal. *Nat. Chem.* **2017**, *9* (8), 824–827.

(41) Wang, X.; Sha, R.; Kristiansen, M.; Hernandez, C.; Hao, Y.; Mao, C.; Canary, J. W.; Seeman, N. C. An Organic Semiconductor Organized into 3D DNA Arrays by "Bottom-up" Rational Design. *Angew. Chem. Int. Ed.* **2017**, *56* (23), 6445–6448.

(42) Um, S. H.; Lee, J. B.; Park, N.; Kwon, S. Y.; Umbach, C. C.; Luo, D. Enzyme-Catalysed Assembly of DNA Hydrogel. *Nat. Mater.* **2006**, *5* (10), 797–801.

(43) Otwinowski, Z.; Minor, W. Processing of X-Ray Diffraction Data Collected in Oscillation Mode. *Methods Enzymol.* **1997**, *276*, 307–326.

(44) Kielar, C.; Xin, Y.; Shen, B.; Kostiainen, M. A.; Grundmeier, G.; Linko, V.; Keller, A. On the Stability of DNA Origami Nanostructures in Low-Magnesium Buffers. *Angew. Chem. Int. Ed.* **2018**, *57* (30), 9470–9474.

(45) Zhang, T.; Hartl, C.; Frank, K.; Heuer-Jungemann, A.; Fischer, S.; Nickels, P. C.; Nickel, B.; Liedl, T. 3D DNA Origami Crystals. *Adv. Mater.* **2018**, *30* (28), e1800273.

(46) Ke, Y.; Ong, L. L.; Sun, W.; Song, J.; Dong, M.; Shih, W.; Yin, P. DNA Brick Crystals with Prescribed Depths. *Nat. Chem.* **2014**, *6* (11), 994–1002.

(47) Brady, R. A.; Brooks, N. J.; Foderà, V.; Cicuta, P.; Michele, L. An Amphiphilic-DNA Platform for the Design of Crystalline Frameworks with Programmable Structure and Functionality. *J. Am. Chem. Soc.* **2018**, *140* (45), 15384–15392.

(48) Doyle, S. A.; Murphy, M. B. The Regents of the University of California, assignee. **2008**. Aptamers and Methods for Their in Vitro Selection and Uses Thereof. United States Patent 7329742.

(49) LaMer, V. K.; Dinegar, R. H. Theory, Production and Mechanism of Formation of Monodispersed Hydrosols. *J. Am. Chem. Soc.* **1950**, *72* (11), 4847–4854.

(50) Kim, D.-N. N.; Kilchherr, F.; Dietz, H.; Bathe, M. Quantitative Prediction of 3D Solution Shape and Flexibility of Nucleic Acid Nanostructures. *Nucleic Acids Res.* **2012**, *40* (7), 2862–2868.

(51) Pan, K.; Kim, D.-N. N.; Zhang, F.; Adendorff, M. R.; Yan, H.; Bathe, M. Lattice-Free Prediction of Three-Dimensional Structure of Programmed DNA Assemblies. *Nat. Comm.* **2014**, *5*, 5578.

(52) Williams, S.; Lund, K.; Lin, C.; Wonka, P.; Lindsay, S.; Yan, H. DNA Computing, 14th International Meeting on DNA Computing, DNA 14, Prague, Czech Republic, June 2-9, 2008. Revised Selected Papers. **2009**, 90–101.

(53) Pettersen, E. F.; Goddard, T. D.; Huang, C. C.; Couch, G. S.; Greenblatt, D. M.; Meng, E. C.; Ferrin, T. E. UCSF Chimera—A Visualization System for Exploratory Research and Analysis. *J. Comput. Chem.* **2004**, *25* (13), 1605–1612.

(54) Wang, P.; Gaitanaros, S.; Lee, S.; Bathe, M.; Shih, W. M.; Ke, Y. Programming Self-Assembly of DNA Origami Honeycomb Two-Dimensional Lattices and Plasmonic Metamaterials. *J. Am. Chem. Soc.* **2016**, *138* (24). 7733–7740.

(55) Sha, R.; Birktoft, J. J.; Nguyen, N.; Chandrasekaran, A.; Zheng, J.; Zhao, X.; Mao, C.; Seeman, N. C. Self-Assembled DNA Crystals: The Impact on Resolution of 5′-Phosphates and the DNA Source. *Nano Lett.* **2013**, *13* (2), 793–797.

PUBLICATIONS

1. Song, J.*; Li, Z.*; Wang, P.*; Meyer, T.; Mao, C.; Ke, Y. Reconfiguration of DNA Molecular Arrays Driven by Information Relay. *Science* **2017**, *357*, eaan3377. (*Contributed equally)
2. Li, Z.; Liu, L.; Zheng, M.; Zhao, J.; Seeman, N.; Mao, C. Making Engineered 3D DNA Crystals Robust. (*submitted*)
3. Liu, L.; Li, Z.; Li, Y.; Mao, C. Rational Design and Self-Assembly of Two-Dimensional, Dodecagonal DNA Quasicrystals. *J. Am. Chem. Soc.* **2019**, Article ASAP
4. Zhao, J.; Zhao, Y.; Li, Z.; Wang, Y.; Sha, R.; Seeman, N.; Mao, C. Modulating Self-Assembly of DNA Crystals with Rationally Designed Agents. *Angew. Chem. Int. Ed.* **2018**, *57*, 16529-16532.
5. Liu, L.; Zheng, M.; Li, Z.; Li, Q.; Mao, C. Patterning Nanoparticles with DNA Molds. *ACS Appl. Mater. Interfaces* **2019**, Article ASAP

RESEARCH ARTICLE SUMMARY

DNA NANOTECHNOLOGY

Reconfiguration of DNA molecular arrays driven by information relay

Jie Song,*† Zhe Li,* Pengfei Wang,* Travis Meyer, Chengde Mao,† Yonggang Ke†

INTRODUCTION: Information relay at the molecular level is an essential phenomenon in numerous chemical and biological processes. A key challenge in synthetic molecular self-assembly is to construct artificial structures that imitate these complex dynamic behaviors in controllable systems. One promising route is DNA self-assembly, a potent approach for the design and construction of arbitrary-shaped artificial nanostructures with increasing complexity and precision. Nonetheless, despite recent progress in the construction of reconfigurable DNA nanostructures that undergo tailored post-assembly transformations in response to different physical or chemical cues, the dynamic behaviors of massive, complex DNA structures remain limited. The existing systems typically exhibit relatively simple dynamic behaviors that involve a single step or a few steps of transformation. Moreover, many of these structures contain mainly static segments joined by a few small reconfigurable domains.

RATIONALE: Here, we demonstrated prescribed, long-range information relay in artificial molecular arrays assembled from modular DNA antijunction units. The small dynamic antijunction unit contains four DNA double-helix domains of equal length and four dynamic nicking points, and can switch between two stable conformations, through an intermediate open conformation. In an array, the driving force of information relay is base stacking: The conformational switch of one antijunction unit will cause the interface between the transformed unit and its neighboring units to become a high-energy conformation with weakened base stacking, leading to transformations in the neighboring units. The array transformation is equivalent to a molecular "domino array": Once initiated at a few selected units, the transformation then propagates, without the addition of extra "trigger strands," to neighboring units and eventually the entire array. The specific information pathways by which this transformation occurs can be controlled by adding trigger strands to specific units, or by altering the design of individual units, the connections between units, and the geometry of the array.

RESULTS: The reconfigurable DNA relay arrays were constructed by using both origami and single-strand–brick approaches. In one-pot assembly, we observed that the arrays built from antijunction units exhibited a spectrum of shapes to accommodate different combinations of antijunction conformations. With the incorporation of set strands, we could lock the arrays into prescribed conformations. The more set strands were added, the greater the assembly shifted toward the corresponding array conformation. Other factors, including the size and aspect ratio of an array, the connecting pattern of an array, DNA sequences of an array, cation concentration, and temperature, have been shown to affect the result of one-pot assembly.

ON OUR WEBSITE

Read the full article at http://dx.doi.org/10.1126/science.aan3377

The transformation cascade was demonstrated with preassembled arrays. When starting from one conformation, addition of the trigger strand at selected locations of the array initiates structural transformation from the selected sites and propagates to the rest of the array in a stepwise manner without additional trigger strands at other locations. Releasing the old trigger strands and adding new ones can transform the array back to its initial conformation—a reversible process that can be repeated multiple rounds. In addition, we were able to control the propagation pathway to follow prescribed routes, as well as to stop and then resume propagation by mechanically decoupling the antijunctions or introducing "block strands." The kinetics of array transformation can be enhanced by elevated temperature or formamide. These assembly and transformations were studied mainly by atomic force microscopy and native agarose gel electrophoresis.

CONCLUSION: Our work demonstrates controlled, multistep, long-range transformation in DNA nanoarrays, assembled by interconnected modular dynamic units that can transfer their structural information to neighbors. The array's dynamic behavior can be regulated by external factors, the shapes and sizes of arrays, the initiation of transformation at selected units, and the engineered information propagation pathways. We expect that the DNA relay arrays will shed new light on how to construct nanostructures with increasing size and complex dynamic behaviors, and may enable a range of applications, such as the construction of molecular devices to detect and translate molecular interactions to conformational changes in DNA structures, to remotely trigger subsequent molecular events. ■

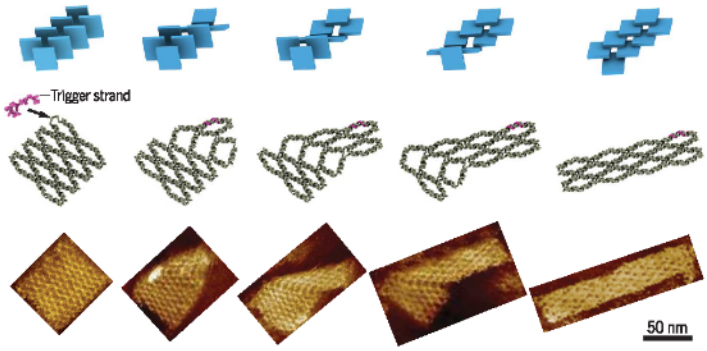

Information relay in DNA "domino" nanoarrays. In a manner similar to that of domino arrays (top), the molecular DNA nanoarray transforms in a step-by-step relay process, initiated by the hybridization of a trigger strand to a single unit (middle). Different stages of nanoarray transformation were confirmed by AFM (bottom). Scale bar, 50 nm.

The list of author affiliations is available in the full article online.
*These authors contributed equally to this work.
†Corresponding author. Email: yonggang.ke@emory.edu (Y.K.); sjie@sjtu.edu.cn (J.S.); mao@purdue.edu (C.M.)
Cite this article as J. Song *et al.*, *Science* **357**, eaan3377 (2017). DOI: 10.1126/science.aan3377

RESEARCH ARTICLE

DNA NANOTECHNOLOGY

Reconfiguration of DNA molecular arrays driven by information relay

Jie Song,[1,2]*† Zhe Li,[3]* Pengfei Wang,[1]* Travis Meyer,[1]
Chengde Mao,[3]† Yonggang Ke[1,4]†

Information relay at the molecular level is an essential phenomenon in numerous chemical and biological processes, such as intricate signaling cascades. One key challenge in synthetic molecular self-assembly is to construct artificial structures that imitate these complex behaviors in controllable systems. We demonstrated prescribed, long-range information relay in an artificial molecular array assembled from modular DNA structural units. The dynamic DNA molecular array exhibits transformations with programmable initiation, propagation, and regulation. The transformation of the array can be initiated at selected units and then propagated, without addition of extra triggers, to neighboring units and eventually the entire array. The specific information pathways by which this transformation occurs can be controlled by altering the design of individual units and the arrays.

Molecular self-assembly has played a crucial role in bottom-up fabrication of materials across many length scales. Structural DNA nanotechnology (*1*) has proved to be a potent approach for the design and construction of arbitrarily shaped artificial nanostructures, including static and dynamic structures, largely because of the programmability of this versatile biomolecule. The field has produced diverse, custom-shaped DNA nanostructures, including one-dimensional (1D) ribbons (*2*–*4*) and tubes (*2*, *4*–*10*), 2D lattices (*5*, *10*–*16*), and finite 2D and 3D objects with prescribed shapes (*14*, *17*–*30*).

The basic principle of DNA nanostructure design is to engineer structural information into the DNA sequences by programming complementarity between component DNA strands (*1*). The present approaches for constructing DNA nanostructures largely fall into two major categories: DNA origami and DNA tiles. DNA origami is a "folding" method, in which a long "scaffold" strand (often M13 viral genomic DNA) is folded into a prescribed shape via interactions with hundreds of short, synthetic "staple" strands (*20*). The DNA tile method assembles DNA structures by connecting small structural units, typically consisting of a small number of strands (*11*). The DNA origami approach has produced fully addressable structures up to several thousands of base pairs (bp) (*7*). Similar-sized, fully addressable structures have also been fabricated with special types of DNA tiles, such as single-stranded tiles (*4*, *26*) or DNA bricks (*27*).

Besides engineering intricate static structures, DNA has also been used to fabricate dynamic structures with tailored postassembly transformations—another important advantage of self-assembly from information-rich biomolecules. Many dynamic DNA devices have been demonstrated, including tweezers (*31*–*34*), walkers (*35*–*40*), reconfigurable arrays assembled from simple DNA tile units (*41*), and other complex devices (*14*, *42*, *43*). These devices can sense a range of physical or chemical cues. Nonetheless, the dynamic behaviors of massive, complex DNA structures are still limited. The existing systems typically exhibit relatively simple dynamic behaviors that involve a single step or a few steps of transformation. Moreover, despite their massive size, many dynamic DNA origami structures were designed to contain mainly static segments joined by a few small dynamic regions (*14*, *42*, *43*).

Here we demonstrate programmable molecular information cascades formed by DNA arrays, which simulate some of the key aspects of complex biological signaling cascades, such as initiation, propagation, and regulation observed in signaling cascades initiated by T cell receptor binding. (*44*) Our large, scalable DNA array is analogous to a molecular "domino array": the step-by-step transformation propagates through the interconnected DNA units via specifically prescribed pathways (fig. S1). We show that the reversible transformation of a DNA array can be initiated at designated locations, and follows pathways precisely controlled by programming the shape of the array or by adding molecular switches that block and then resume the information relay between units.

Design of DNA relay arrays

We used small dynamic DNA units called "antijunctions" (*45*) to build large, scalable, reconfigurable DNA structures. An antijunction contains four DNA duplex domains of equal length and four dynamic nicking points (Fig. 1, A and B; note that the strand in gray contains a static nick, which does not change during reconfiguration). This small construct can switch between two stable conformations—"red" and "green," driven by base-stacking, through an unstable open (including partially open) conformation—"orange." Each duplex is $0.5 \times n$ turns (n = 1, 2, 3, 4...) in length (fig. S2A). An antijunction is classified by the distance between two opposite dynamic nicking points (i.e., a 42-bp antijunction).

In a connected network, the conformational information of an antijunction can pass to its closest neighbors, introducing subsequent conformational change of the neighboring antijunctions (Fig. 1C). The transformation of an individual antijunction unit (e.g., from red to green) can be induced by adding a trigger DNA strand that forms a continuous duplex on one edge of the unit (fig. S3A). The key design feature of trigger strands is that each trigger strand removes a mobile nick point from an antijunction unit. After the conformational switch from red to green of the triggered unit, the interface between the two neighboring units becomes a high-energy open conformation, leading to a transformation in the neighboring unit to the same conformation (green) as the already transformed unit. This process is driven by the reduction of free energy, caused by the formation of an additional base-stacking interaction at the connection point (see fig. S3B for more details).

We built 2D molecular DNA relay array via self-assembly of the antijunctions (Fig. 1D). A relay array can transform from one array conformation (e.g., all antijunctions are in the red conformation) to another array conformation (e.g., all antijunctions are in the green conformation). The array transformation follows specific pathways, depending on the array's geometry and binding locations of trigger strands (fig. S4). For instance, if the trigger strands were added to the units (Fig. 1, D and E) at a corner, the relay would undergo a step-by-step conversion from a red array conformation to a green array conformation via a diagonal pathway.

DNA relay arrays can be constructed with both noncanonical DNA bricks (single-stranded modular DNA units) and DNA origami (further discussion is in figs. S5 to S8). Owing to the constraint of the continuous scaffold, a DNA-origami antijunction must be an odd-number-turn antijunction (e.g., 32-bp antijunction; figs. S5 and S7). In comparison, a DNA-brick antijunction can be either an odd-number-turn antijunction (e.g., 32-bp antijunction; figs. S5 and S7) or an even-number-turn antijunction (e.g., 42-bp antijunction; figs. S6 and S8). One of the array conformations of the DNA-brick arrays is arbitrarily assigned as

[1]Coulter Department of Biomedical Engineering, Emory University and Georgia Institute of Technology, Atlanta, GA 30322, USA. [2]Department of Instrument Science and Engineering, School of Electronic Information and Electrical Engineering, Shanghai Jiaotong University, Shanghai 200240, China. [3]Department of Chemistry, Purdue University, West Lafayette, IN 47907, USA. [4]Department of Chemistry, Emory University, Atlanta, GA 30322, USA.
*These authors contributed equally to this work. †Corresponding author. Email: yonggang.ke@emory.edu (Y.K.); sjie@sjtu.edu.cn (J.S.); mao@purdue.edu (C.M.)

the red array conformation, and the other is assigned as the green array conformation (fig. S5, B and D). For DNA-origami relay arrays, the conformation where the scaffold does not cross between DNA helices within the array is assigned as the red array conformation, and the other conformation is assigned as the green conformation (fig. S5, C and E).

One-pot assembly of DNA-brick relay arrays

The transformation pathway of a DNA relay array is expected to be dictated by the stable conformations corresponding to local energy minima. To investigate these local energy-minimum states, we first studied the self-assembly of rectangular 42-bp DNA-brick relay arrays via one-pot isothermal assembly. The results revealed that the most dominant conformations were the red array conformation and the green array conformation. In addition to the two dominant conformations, which should correspond to the two lowest-energy states, we observed many mixed-conformation arrays that consist of both regions of red antijunctions and regions of green antijunctions. We observed that the red antijunction regions and the green antijunction regions were always bridged by a diagonal seam(s) that contains open orange antijunctions. These orange antijunctions are unstable by themselves, but can exist in an array structure when they are flanked by red antijunctions and green antijunctions (Fig. 2A). These arrays with mixed antijunction conformations are called "mixed array" conformations, which correspond to local energy minima in the assembly (Fig. 2B). Further discussion of these stable mixed array conformations is in fig. S9.

Native agarose gel electrophoresis of a rectangular 20 unit by 4 unit (20 × 4) 42-bp DNA-brick relay array revealed two product bands that correspond to the red array conformation and the green array conformation, respectively (Fig. 2C). The green array conformation showed greater mobility than the red array conformation, likely due to its elongated geometry. The mixed array conformations contain many different shapes that do not migrate as a single band, but were observed in atomic force microscopy (AFM) images of unpurified samples (Fig. 2D).

An 11 × 4 42-bp DNA-brick relay array was used to test optimal assembly conditions (fig. S10). The best yield was observed when the array was assembled at 51.3°C isothermally, in a Tris-EDTA (TE) buffer containing 10 mM $MgCl_2$. Addition of single-stranded poly-T extensions around the boundary of the array further improved the yield (fig. S11), presumably due to the poly-T's function of mitigating unwanted aggregation (*20*).

Regulation of assembly of DNA-brick relay arrays

To understand how size and aspect ratio affect the assembly of DNA relay array, we tested the one-pot assembly of a group of rectangular 42-bp DNA-brick relay arrays. The largest structure is a 20 × 8 DNA-brick array consisting of randomly generated ~14,000 bp (Fig. 2E). In total, 16 DNA-brick relay arrays with different sizes and aspect ratios were generated by using the 20 × 8 relay array as a molecular canvas (Fig. 2F and fig. S12). Native agarose gel electrophoresis and AFM images

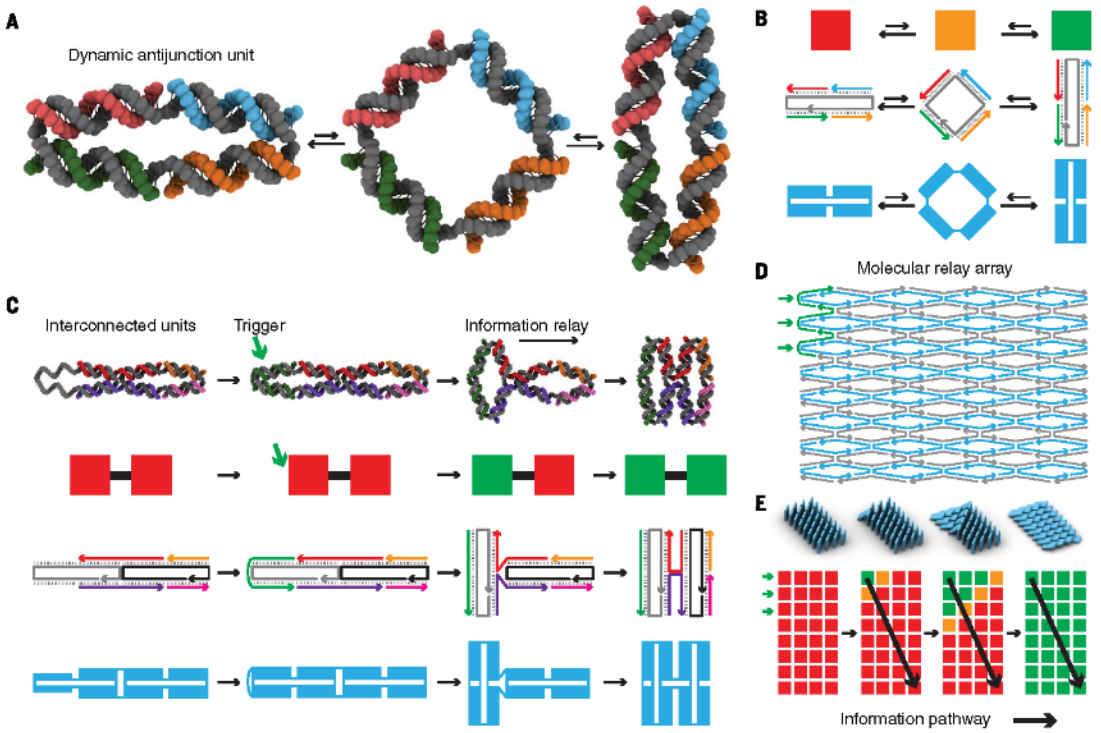

Fig. 1. Molecular relay arrays assembled by DNA. (**A**) A dynamic DNA antijunction can switch between two stable conformations, through an unstable open conformation. (**B**) Different diagrams for a DNA antijunction: stable conformations "red" and "green," and unstable conformation "orange." (**C**) Transformation of an antijunction unit can be induced by addition of a trigger strand. The information is passed from the converted unit to its closest neighbors, causing them to undergo subsequent transformation. (**D**) Strand diagram of an interconnected 2D DNA relay array with 4 units by 8 units. Three trigger strands (green) are added to three units in the upper-left corner of the array to initiate the transformation (**E**) The information of transformation propagates along prescribed pathways, causing the units to convert sequentially in this molecular array.

(figs. S13 and S14) were used to analyze the percentages of the red array conformation, the green array conformation, and the mixed array conformation of the 16 structures (Fig. 2F, fig. S15, and table S1). All relay arrays produced a large amount of both the red arrays and the green arrays, except for the $n \times 2$ arrays, whose assembly appeared to favor the larger-aspect ratio green array conformation, suggesting that aspect ratios play a more important role for this group of structures. Our analysis, using a simple proximity model (fig. S16) that considered only the energy between the closest neighboring helices, showed that the array's aspect ratios had a larger effect on the $n \times 2$ arrays, consistent with the above observation.

We then studied how the one-pot assembly of arrays was affected by the presence of trigger strands, connection patterns between units, and the DNA sequences. In the first test, the addition of a few trigger strands in the one-pot assembly clearly altered the R/G ratios for the 11 × 4 42-bp DNA-brick relay array (Fig. 2G and table S2). As expected, the more trigger strands were added to the one-pot assembly, the further the assembly shifted toward the corresponding array conformation.

Changing the connectivity between antijunction units also affects the assembly of the 11 × 4 42-bp DNA-brick relay array (Fig. 2H and fig. S17). When antijunction units were removed from the 11 × 4 42-bp DNA-brick relay array, the assembly shifted to more green array conformations (Fig. 2H), probably because of the increasing narrow (1.5 units in width) areas, which favor a green array conformation.

In comparison to the results in Fig. 2G, assembly of the 11×4 42-bp DNA brick relay array with missing units in the presence of eight red trigger strands resulted in a more mixed array conformation, likely because the reduced connectivity also diminishes the effectiveness of trigger strands (Fig. 2I). This effect is particularly pronounced with the 11 × 4 42-bp DNA brick relay array with two holes—about half of the arrays formed a "mask"-shaped mixed array conformation (fig. S18). Statistics of the 11 × 4 42-bp DNA brick relay array with modified connectivity are shown in table S3, and additional studies on controlling the one-pot assembly of DNA-brick relay arrays are included in fig. S19.

Considering that the change of base stacking occurs only at each four-way junction, the DNA sequences at the junctions may play an important role in determining the assembly results. To verify this hypothesis, we tested two versions of the 11 × 4 42-bp DNA-brick relay arrays with modified sequences at the junctions (fig. S20). The two arrays (design I and II) have the same sequences, except for the eight DNA bases at

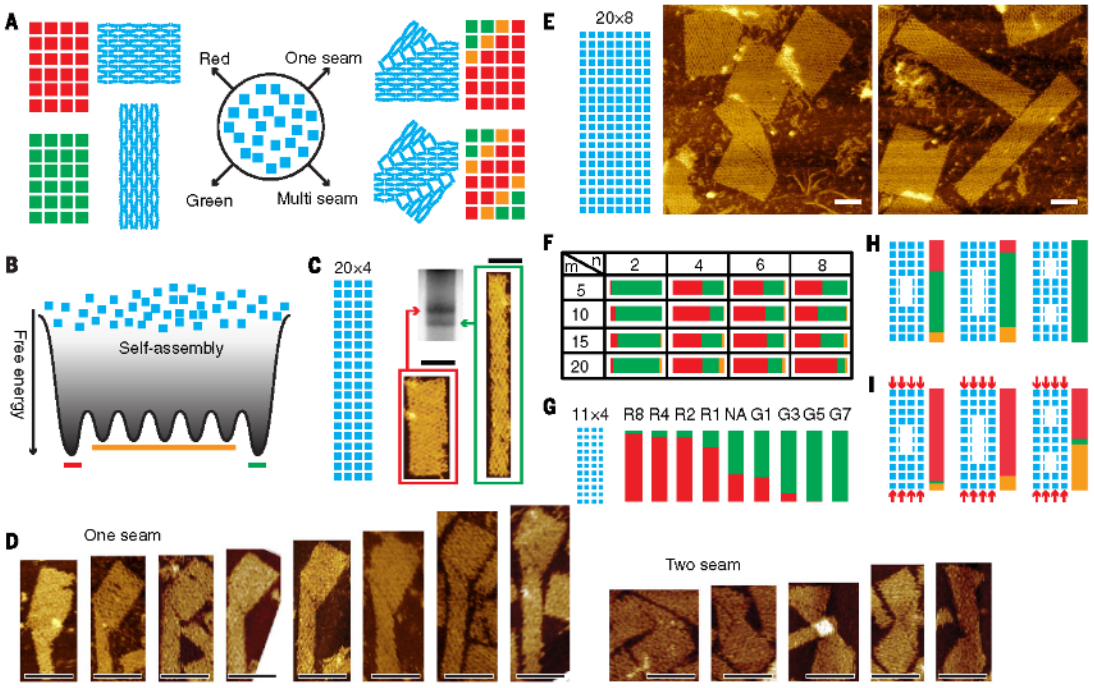

Fig. 2. One-pot assembly of 42-bp DNA-brick relay arrays. (**A**) Multiple conformations result from assembly of a DNA-brick relay array: "red array" conformation, "green array" conformation, and "mixed array" conformations, which contains units with red conformation, green conformation, and orange conformation. The orange units (corresponding to a higher-energy, unstable state) form diagonal seams that bridge together the red units and the green units. (**B**) Proposed, simplified energy landscape of assembly. The units assemble into the two global energy minima corresponding to the red array conformation and the green array conformation, and local energy minima corresponding to the mixed array conformations. (**C**) Assembly of the 20 × 4 42-bp DNA-brick relay array results in two (red array and green array) dominant products in the agarose gel. (**D**) AFM images of mixed array conformations of the 20 × 4 42-bp DNA-brick relay array. (**E**) The 20 × 8 42-bp DNA-brick relay array is used as a "canvas" to generate relay arrays of different sizes and aspect ratios. (**F**) Percentages of red array conformation, green array conformation, and mixed array conformation of $m \times n$ relay arrays. (**G**) Numbers (n) of red triggers (Rn) and green triggers (Gn) shift the assembly result of the 11 × 4 42-bp DNA-brick relay array. (**H**) Removal of units from the 11 × 4 42-bp DNA-brick relay array alters the assembly result. (**I**) A combination of unit removal and addition of eight red triggers affects the assembly result. Scale bars, 50 nm.

each four-way junction. The assembly results showed a strong correlation between the junction sequences (and thus the base stacking) and the red/green (R/G) ratios. In good agreement with our estimate, the green array was the dominant conformation (R/G = 0.24) for design I, while the red array was the dominant conformation (R/G = 3.0) for design II.

Transformation of DNA-origami relay array

To identify a suitable design for our study of DNA array transformation, we compared different DNA-brick relay arrays and DNA-origami relay arrays. Overnight room-temperature incubation of red trigger strands with a preassembled 11 × 4 42-bp DNA-brick relay array, an 8 × 5 52-bp DNA-brick relay array, and a 10 × 4 64-bp DNA-brick relay array (fig. S21) did not convert a noticeable

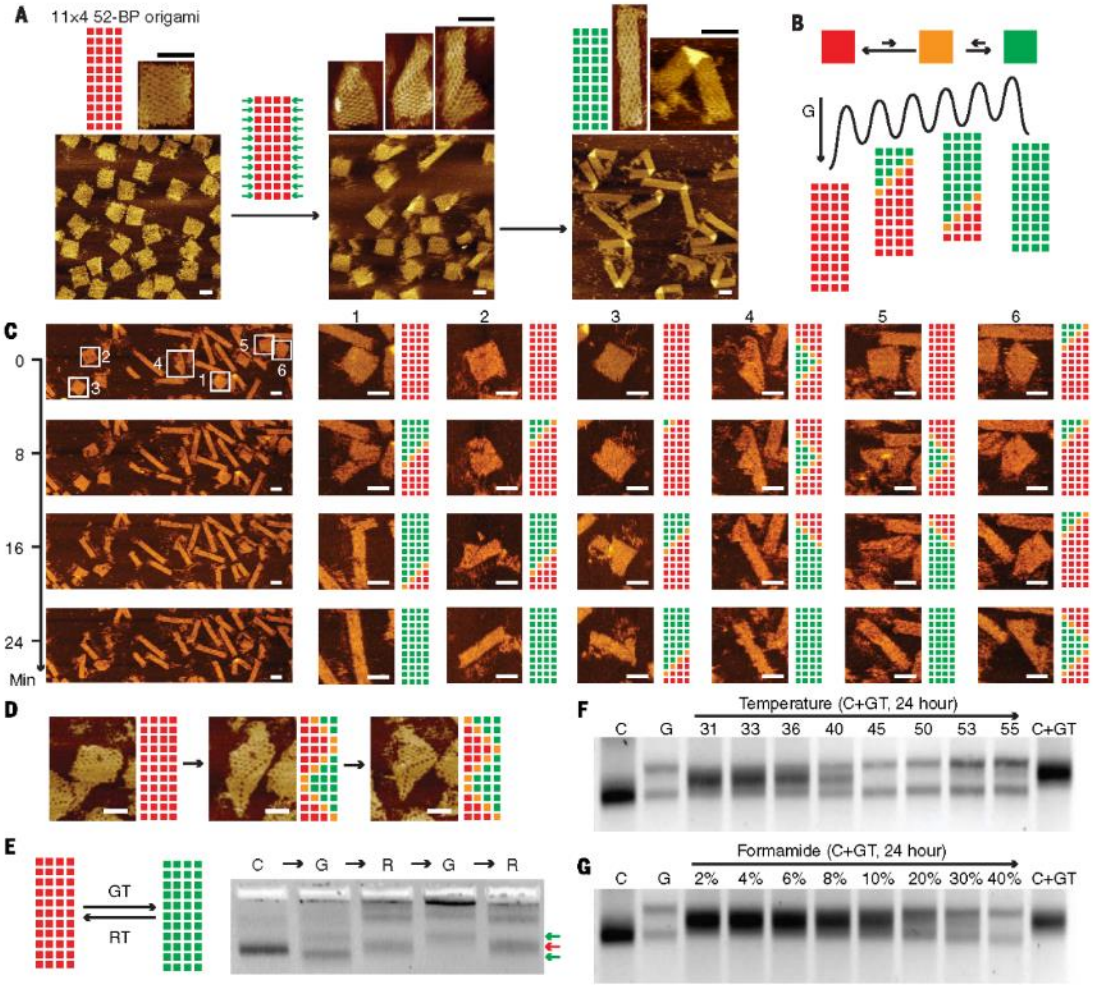

Fig. 3. Transformation of DNA-origami relay arrays. (**A**) An 11 × 4 52-bp DNA-origami relay array forms predominantly red array conformations. Subsequent addition of 22 green triggers converted the red array conformation to the mixed array conformation, then to the green array conformation. Some of the green arrays are folded because of the tension generated by the free scaffold. (**B**) The 52-bp DNA-origami relay array showed a greater tendency to form red array conformations than green array conformations. (**C**) AFM images (4-min scan time per frame) show real-time transformation of the relay array from red array conformations to green array conformations in the presence of 22 green triggers. The transformation was mostly initiated at a corner, although sometimes from the middle section of an edge, and followed the diagonal pathways. (**D**) Occasionally the transformation was initiated at separate, multiple locations. (**E**) The red/green array transformation is a reversible process, which can be repeated multiple times by removal of previous triggers and addition of new triggers. Arrows indicate the product bands. Note that the green array conformation has two bands. (**F** and **G**) The kinetics are accelerated by elevated temperature (F) or formamide concentration (G) for the transformation from the red array conformation to the green array conformation. Lane C: Relay array assembled without trigger. Lane G: Relay array assembled with 22 green triggers. The slower-mobility band corresponds to the folded green array conformation in (A). Lane C+GT: 22 green triggers (GT) were added to a preassembled relay array (C), and immediately loaded into the gel. It appears that the triggers quickly bind to the array, causing a shift of mobility. Scale bars, 50 nm.

percentage of green array conformation to red array conformation. The arrays were then incubated at higher temperatures or in solutions containing higher concentrations of formamide to accelerate the transformation kinetics, but the DNA-brick relay array started to show damage at 55°C or 40% formamide before noticeable transformation was observed.

We then turned our attention to DNA-origami relay arrays, which may be more resilient to denaturing conditions because of the long scaffold strand. We assembled an 11 × 7 32-bp DNA-origami relay array (fig. S22) and an 11 × 4 52-bp DNA-origami relay array with a p7560 scaffold. Both arrays resulted in only the red array conformation. It is unknown how the scaffold (about half the molecular weight of the whole array) might affect the formation and transformation of the DNA-origami relay array, and the scaffold dependence of the DNA-origami relay array requires further study. We eventually chose the 52-bp DNA-origami relay array for real-time transformation, as subsequent studies revealed that this relay array is easiest to transform and is convenient for image analysis.

Transformation of preassembled 11×4 52-bp DNA-origami relay array in the red conformation was initiated by the addition of 22 green trigger strands. The arrays initially transformed to mixed conformations at 45°C, then to ~100% green array conformations at 55°C (Fig. 3A). Analysis of the mixed array conformations revealed that the dominant pathway of transformation is diagonal, consistent with the results for DNA-brick relay arrays. Based on the results of the transformation from the red array conformation to the green array conformation, we made the assumption that the red unit conformation was slightly favored over the green unit conformation in the p7560 DNA-origami relay array, resulting in a tilted energy landscape for the transformation process (Fig. 3B and fig. S23).

Real-time AFM was used to study the in situ single-molecule transformation of the DNA relay arrays (Fig. 3C and fig. S24). Within a 30-min scan, multiple array transformations were observed. The transformation appeared to be a stochastic process: Most of the transformations started from a corner and propagated through a diagonal pathway, while a smaller number of transformations were initiated from the edges and propagated along a "swallowtail" pathway. In rare cases, transformation of an array was also observed being initiated at multiple locations (Fig. 3D).

The transformation of the 52-bp DNA-origami relay array is reversible. Using modified trigger strands with toehold extensions and corresponding release strands, we demonstrated multiple conversions between the red array conformation and the green array conformation (Fig. 3E and fig. S25). The green array conformation has two product bands: The upper band and the lower band correspond to the folded structure [due to the tension generated by the free scaffold (*46*)] and open structure, respectively, in Fig. 3A. We observed that the "open" green conformation is more dominant than the "folded" green conformation after the initial assembly. However, after the array's transformation to red, and then back to green, nearly 100% of arrays turned into the folded green conformation. The underlying reason for this conversion needs further investigation.

The kinetics of the transformation can be accelerated by either increasing temperatures (Fig. 3F) or using higher concentrations of formamide (Fig. 3G), likely because of the reduced energy needed to break the base-stacking interactions under these denaturing conditions [e.g., increasing the temperature reduces the base-stacking energy from an average of −5.2 kJ/mol at 32°C to −2.9 kJ/mol at 52°C (*47*)]. The real-time transformation in Fig. 3C was acquired by using DNA-origami relay arrays in a 10% formamide solution. We also observed real-time transformation of an 11 × 4 32-bp DNA origami array at 65°C using a temperature-controlled AFM (*48*) (fig. S26). However, the AFM images are much noisier at such a high temperature. The kinetics of transformation can also be increased by the mechanical disturbance induced by the AFM tip, as shown in fig. S27. The transformations occurred at higher frequencies when the sample was subjected to the contact force from the AFM tip. This AFM tip–enhanced transformation was confined to only the scanned area. This phenomenon may provide a means to manipulate our dynamic DNA arrays at specific locations.

Regulation of transformation in DNA relay arrays

With a better understanding of the factors affecting transformation, we extended our study to control the transformation of the DNA-origami relay arrays. We demonstrated that transformation could be initiated at selected locations, blocked, and controlled using arrays with different shapes.

The transformation can be initiated at prescribed locations on the 11 × 4 52-bp DNA origami relay array. Using real-time AFM, we demonstrated initiation of transformation from a corner or from the middle of an edge with five green trigger strands and subsequent propagation of the new conformation (Fig. 4A and fig. S28). Both the number and locations of trigger strands affect the initiation of array transformation and the degree of transformation. A detailed study is included in fig. S29. With three or fewer trigger strands added in a corner, the transformation process could not be initiated. Increasing the number of trigger strands to six or eight triggered partial conversion to mixed array conformations, with a small number of green array conformations. The addition of 11 green trigger strands led to full transformation to the green conformation for most of the arrays. Adding trigger strands to the corners appeared to be more effective at inducing transformation than adding the same number of triggers to the edges (fig. S29B). In addition, adding both red trigger and green trigger strands can lead to transformation to specific mixed array conformations (fig. S29C). We also compared the transformation efficiency of preassembled arrays using a one-pot assembly in the presence of triggers. As expected, the results showed that conversion was typically more complete under the one-pot assembly condition (fig. S30).

We also explored two strategies to turn off or turn on transformation at selected locations by blocking or resuming the information pathways between units. In the first approach, we created an "off" function by removing one unit from the relay array, which creates a local energy minimum (Fig. 4B and fig. S31) that traps the array transformation. Reintroduction of the missing unit enables the transformation to escape the trap and proceed (Fig. 4B). We further demonstrated the blocking and resuming of transformation at different locations on the array using this strategy (Fig. 4C and fig. S32). In the second approach, we showed that this "off" function can also be achieved by using a "lock" strand (Fig. 4D). This strand binds to single-stranded DNA extensions from two neighboring units, effectively locking the units into a fixed conformation (fig. S33).

Information relay in an DNA relay array can also be programmed by removal or addition of antijunction units. Using the 11 × 4 52-bp DNA-origami relay array as a canvas, we demonstrated a "2" shaped array by removing eight units. (Fig. 4E and fig. S34). After the initiation of transformation at the top corner, this array transformed in a three-step process: The addition of two initial corner triggers transferred the array only up to the top-right corner; five additional triggers were added to the top-right corner to push the transformation about halfway through the array; finally, the array transformation was completed after the subsequent addition of another five triggers. Each step was verified in AFM images.

Spontaneous transformation of both DNA-brick relay array and DNA-origami relay array without addition of triggers was occasionally observed during the AFM scan in the presence of 10 to 30% formamide (fig. S35), but an in-depth study of this rare and random phenomenon was not pursued in this work.

We then studied how the transformation of DNA-origami relay arrays is influenced by connecting the arrays into monomer tubes, and into oligomer 1D chains and tubes. We substituted the red triggers for connector strands that link the top and bottom edges of the 11 × 4 52-bp DNA-origami relay array (fig. S36). The relay array assembly with the connectors resulted in a red-conformation nanotube, which could convert to a green-conformation tube after addition of 22 green trigger strands (Fig. 4F). In comparison to the 2D relay arrays, unit conversion in the nanotube was more cooperative. A two-step process was observed: first, the tube was converted to a stable state in which most units appeared partially open at 40°C (Fig. 4F and 4G, top); then, the tube was fully converted to a green-conformation tube at 50°C (Fig. 4F and 4G, bottom). Further discussion, AFM images, and transmission electron microscopy (TEM) images are shown in fig. S37A. By contrast, one-pot assembly of the array with both the connectors and green triggers did not produce green-conformation tubes (figs. S37B and S38).

Instead, oligomer tubes and 1D chains of arrays were observed (Fig. 4H and fig. S39). This behavior differs from that of a previous work in which an origami tube design formed two isomers in one-pot assembly (*49*). This is likely because the addition of more green triggers should favor interarray connections over intra-array connections, owing to the increased rigidity (it is harder to bend the green array conformation). With six green triggers, the assembly resulted in red-conformation oligomer tubes and 1D chains. When 10 green triggers were added to the middle of the array, the assembly produced mostly oligomer 1D chains with mixed red and green conformations. When 11 green triggers were added to one side of the array, assembly resulted in green-conformation 1D chains.

Discussion

Our work has demonstrated a general strategy for the construction of large DNA relay arrays with interconnected modular structural components. Each component is a dynamic unit that can transfer its structural information to neighboring components. Through the study of these DNA relay arrays, we have demonstrated controlled, multistep, long-range transformation of the DNA arrays. This dynamic behavior can be regulated by the shapes and sizes of arrays, by external factors (e.g., temperature), by the initiation of transformation at selected units, and by the information propagation pathways.

A next step would be to extend the DNA relay arrays to 3D spaces, larger sizes, more intricately shaped designs, and more complex dynamic

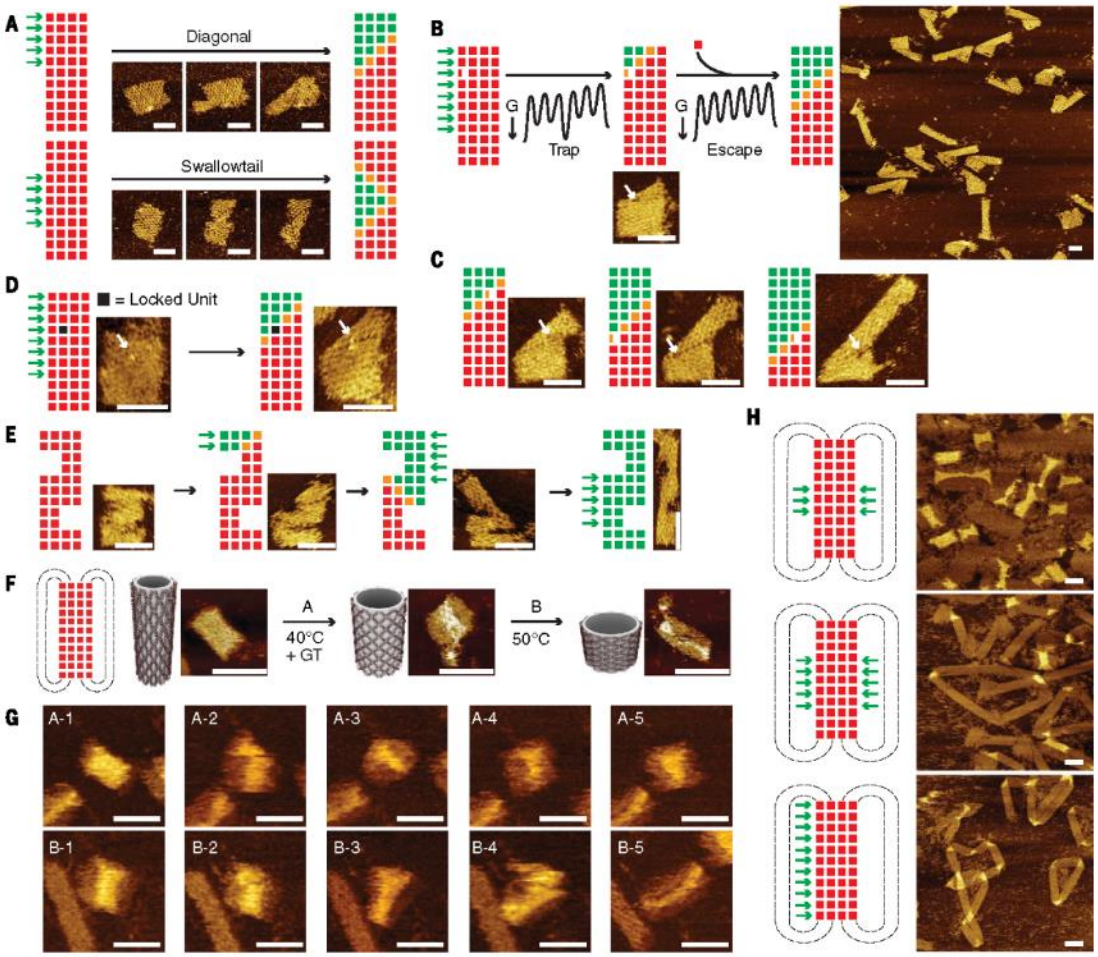

Fig. 4. Controlled transformation of DNA-origami relay arrays. (**A**) Control of the initiation of transformation via selection addition of green triggers (**B**) The transformation pathways can be blocked and resumed by the removal and addition of units. (**C**) The transformation can be blocked at any designated location. (**D**) Blocking of transformation pathways via "lock" strands. (**E**) Control of the transformation pathway using shape design. (**F**) Transformation of a closed design is more cooperative. A stable conformation in which all units are partially open was observed at 40°C. (**G**) Real-time AFM images of transformation from the red array conformation tube to the mixed array conformation tube (A-1 to A-5), and from the mixed array conformation tube to the green array conformation tube (B-1 to B-5). (**H**) Addition of green triggers in one-pot assembly reduced, and eventually eliminated, the red array tube formation. Scale bars, 50 nm.

behaviors. In fig. S40, we show a small 3D DNA-brick relay array design, which consists of two sets of dynamic junctions, perpendicular to each other. As expected, this 3D DNA-brick relay array produced three detectable conformations, confirmed by TEM images. In a previous work, we successfully produced canonical nonreconfigurable 3D DNA-brick structures up to ~12,000 bp (*27*). Assuming that reconfigurable structures with a similar size could be made, the largest structure would contain ~142 42-bp antijunction units. Such large, intricate structures would enable demonstration of complicated transformation in 3D space. Hierarchical assembly of multiple DNA relay arrays may lead to construction of larger and more intricate designs. In addition, more complex information pathways (e.g., multibranched pathways) in DNA relay arrays and sequence-dependent behavior of DNA relay arrays will require further study.

We expect that our new DNA dynamic arrays will shed light on how to construct nanostructures with increasing size and complex dynamic behaviors, and may enable a range of applications using dynamic DNA arrays. For example, the transformation propagation in the DNA relay arrays resembles crucial features of allosteric mechanisms that are observed in biological systems (*50*). Therefore, our artificial arrays may serve as model structures to investigate and validate underlying mechanisms of allostery (*51*, *52*), or be used to design and construct allosteric metamaterials (*53*). The DNA relay arrays may also be used as a platform to analyze biomolecular interactions at a single-molecule level (*46*, *54*–*56*), by translating and amplifying the molecular interactions to conformational changes in the DNA relay arrays or to subsequent molecular events (e.g., chemical reactions, fluorescence resonance energy transfer, etc.). A potential limitation of current DNA relay arrays for biological applications is the slow kinetics of array transformations under mild conditions that are compatible with biomolecules. This challenge may be overcome by the development of next-generation DNA relay arrays through engineering of the structural units and array sequences. In addition, rational sequence design may be used in DNA-brick relay arrays to study the binding energy of the junctions (*57*, *58*), which could enable more sophisticated control of the assembly and transformation of the DNA relay arrays. DNA nanostructures have long been used to construct functional structures and devices by scaffolding the arrangement of proteins, nanoparticles, and other functional materials with nanoscale precision (*59*). The ability to construct large DNA structures with controlled, complex, long-range information relay and dynamic behavior should improve the sophistication and functionality of such hybrid functional structures.

Materials and methods

DNA synthesis

The single-stranded M13 bacteriophage (p7560) scaffold was produced following a published protocol (*23*). Chemically synthesized DNA oligomers were purchased from Integrated DNA Technologies (www.idtdna.com) and were used without further purification. All other reagents were purchased from Sigma-Aldrich (St. Louis, MO).

DNA relay array design

The DNA-origami relay arrays were designed by using caDNAno (*60*). The DNA-brick arrays were designed by using a modified version of software described previously (*27*).

Sample preparation

For 42-bp DNA-brick relay arrays, DNA strands were mixed at equal molar ratio at a final concentration of 100 nM per strand in 1× TE buffer (5 mM Tris, 1 mM EDTA, pH 8.0), supplemented with 5 to 50 mM $MgCl_2$, and then the mixture was subjected to a one-step isothermal-annealing over 18 hours. The optimal isothermal annealing condition was found to be 53°C incubation for 18 hours in 1× TE buffer with 10 mM $MgCl_2$. For 52- and 64-bp DNA-brick relay arrays, DNA strands were mixed at equal molar ratio at a final concentration of 100 nM per strand in 1× TE buffer with 10 mM $MgCl_2$. Then the samples were subjected to a 20-hour thermal annealing protocol: 95°C for 5 min, from 85° to 24°C at a rate of 20 min/°C. For DNA origami relay arrays, the mixture of staple strands (final concentration: 100 nM of each strand) and the scaffold (final concentration: 10 nM) were mixed in 1× TE buffer, supplemented with 12 mM $MgCl_2$. The samples were then annealed for 10 hours using the following thermal annealing protocol: 95°C for 5 min, from 85° to 24°C at a rate of 10 min/°C.

Agarose gel electrophoresis and purification

Samples were subjected to 0.3 to 3% agarose gel electrophoresis at 60 V for 2 to 7 hours in an ice water bath. Gels were prepared with 0.5× TBE buffer containing 10 mM $MgCl_2$ and with 0.005% (v/v) ethidium bromide. For purification, the target gel bands were excised and placed into a Freeze 'N Squeeze column (Bio-Rad Laboratories, Inc.). The gel pieces were crushed into fine pieces with a pestle in the column, and the column was then centrifuged at 7000*g* for 5 min. Samples that were extracted through the column were collected for TEM or AFM imaging.

AFM imaging

For typical AFM imaging, samples were prepared by deposition of a 2 μl DNA array sample onto freshly cleaved mica. The sample area was then filled with ~80 μl of 1× TE buffer with 112 mM $MgCl_2$. Commercial silicon nitride cantilevers with integrated sharpened tips (Bruker, SNL-10) were used. The topographic images were captured by peak force tapping mode experiments on a Multimode VIII system (Bruker Corporation, Santa, Barbara, CA) in liquid.

TEM imaging

To visualize the samples, we deposited 3 μl of purified samples on glow-discharged, carbon-coated TEM grids for 2 min. Samples were then stained for 1 min with 2% uranyl formate solution containing 25 mM NaOH and subsequently imaged using the JEOL JEM-1400 TEM operated at 80 kV.

DNA relay array transformation in solution

For transformation in aqueous solution, excessive trigger strands (~10 to 20 nM) were added to the purified DNA samples (~5 nM). The mixed samples were then incubated at constant temperatures (from room temperature to 60°C) for 5 min to 12 hours. The samples were then subjected to agarose gel electrophoresis assay or deposited on mica for AFM imaging.

Real-time imaging of DNA relay array transformation in solution

For real-time imaging, the purified DNA samples (~5 nM) were first mixed with an excess of trigger strands (generally ~10 to 20 nM) for 1 min and then deposited on mica.

Imaging in formamide: A solution of 80 μl of 1×TE, supplemented with 12 mM MgCl2 and 10 to 30% formamide, was added to the DNA sample on the mica surface. After incubation for ~5 min, the AFM cantilever was brought close to the mica surface at a relatively low force, and started to scan the samples until no further transformation of DNA arrays was observed in the scan area.

Imaging using temperature-controlled AFM: For real-time imaging via thermal control AFM, the images were acquired with a commercial Multimode Microscope V (Digital Instruments, Santa Barbara, CA) in conjunction with a temperature controller. Temperature variation was accomplished via a resistive heating stage (temperature range: ambient temperature to 250°C, resolution: 0.1°C). A cooling water fluid circuit refrigerates the piezo scanner. Then, DNA array samples were scanned at 60°C until no further transformation of DNA arrays was observed in the scan area.

REFERENCES AND NOTES

1. N. C. Seeman, DNA in a material world. *Nature* **421**, 427–431 (2003). doi: 10.1038/nature01406; pmid: 12540916
2. S. H. Park *et al.*, Three-helix bundle DNA tiles self-assemble into 2D lattice or 1D templates for silver nanowires. *Nano Lett.* **5**, 693–696 (2005). doi: 10.1021/nl050108i; pmid: 15826110
3. R. Schulman, E. Winfree, Synthesis of crystals with a programmable kinetic barrier to nucleation. *Proc. Natl. Acad. Sci. U.S.A.* **104**, 15236–15241 (2007). doi: 10.1073/pnas.0701467104; pmid: 17881584
4. P. Yin *et al.*, Programming DNA tube circumferences. *Science* **321**, 824–826 (2008). doi: 10.1126/science.1157312; pmid: 18687961
5. H. Yan, S. H. Park, G. Finkelstein, J. H. Reif, T. H. LaBean, DNA-templated self-assembly of protein arrays and highly conductive nanowires. *Science* **301**, 1882–1884 (2003). doi: 10.1126/science.1089389; pmid: 14512621
6. D. Liu, S. H. Park, J. H. Reif, T. H. LaBean, DNA nanotubes self-assembled from triple-crossover tiles as templates for conductive nanowires. *Proc. Natl. Acad. Sci. U.S.A.* **101**, 717–722 (2004). doi: 10.1073/pnas.0305860101; pmid: 14709674
7. P. W. K. Rothemund *et al.*, Design and characterization of programmable DNA nanotubes. *J. Am. Chem. Soc.* **126**, 16344–16352 (2004). doi: 10.1021/ja044319l; pmid: 15600335
8. F. Mathieu *et al.*, Six-helix bundles designed from DNA. *Nano Lett.* **5**, 661–665 (2005). doi: 10.1021/nl050084f; pmid: 15826105

9. J. Sharma *et al.*, Control of self-assembly of DNA tubules through integration of gold nanoparticles. *Science* **323**, 112–116 (2009). doi: 10.1126/science.1165831; pmid: 19119229
10. Y. Ke *et al.*, DNA brick crystals with prescribed depths. *Nat. Chem.* **6**, 994–1002 (2014). doi: 10.1038/nchem.2083; pmid: 25343605
11. E. Winfree, F. Liu, L. A. Wenzler, N. C. Seeman, Design and self-assembly of two-dimensional DNA crystals. *Nature* **394**, 539–544 (1998). doi: 10.1038/28998; pmid: 9707114
12. P. W. K. Rothemund, N. Papadakis, E. Winfree, Algorithmic self-assembly of DNA Sierpinski triangles. *PLOS Biol.* **2**, e424 (2004). doi: 10.1371/journal.pbio.0020424; pmid: 15583715
13. Y. He *et al.*, Sequence symmetry as a tool for designing DNA nanostructures. *Angew. Chem. Int. Ed.* **117**, 6852–6854 (2005). doi: 10.1002/ange.200502193; pmid: 16187389
14. T. Gerling, K. F. Wagenbauer, A. M. Neuner, H. Dietz, Dynamic DNA devices and assemblies formed by shape-complementary, non-base pairing 3D components. *Science* **347**, 1446–1452 (2015). doi: 10.1126/science.aaa5372; pmid: 25814577
15. P. Wang *et al.*, Programming Self-Assembly of DNA Origami Honeycomb Two-Dimensional Lattices and Plasmonic Metamaterials. *J. Am. Chem. Soc.* **138**, 7733–7740 (2016). doi: 10.1021/jacs.6b03966; pmid: 27224641
16. W. Liu, J. Halverson, Y. Tian, A. V. Tkachenko, O. Gang, Self-organized architectures from assorted DNA-framed nanoparticles. *Nat. Chem.* **8**, 867–873 (2016). doi: 10.1038/nchem.2540; pmid: 27554413
17. J. H. Chen, N. C. Seeman, Synthesis from DNA of a molecule with the connectivity of a cube. *Nature* **350**, 631–633 (1991). doi: 10.1038/350631a0; pmid: 2017259
18. W. M. Shih, J. D. Quispe, G. F. Joyce, A 1.7-kilobase single-stranded DNA that folds into a nanoscale octahedron. *Nature* **427**, 618–621 (2004). doi: 10.1038/nature02307; pmid: 14961116
19. R. P. Goodman *et al.*, Rapid chiral assembly of rigid DNA building blocks for molecular nanofabrication. *Science* **310**, 1661–1665 (2005). doi: 10.1126/science.1120367; pmid: 16339440
20. P. W. K. Rothemund, Folding DNA to create nanoscale shapes and patterns. *Nature* **440**, 297–302 (2006). doi: 10.1038/nature04586; pmid: 16541064
21. Y. He *et al.*, Hierarchical self-assembly of DNA into symmetric supramolecular polyhedra. *Nature* **452**, 198–201 (2008). doi: 10.1038/nature06597; pmid: 18337818
22. E. S. Andersen *et al.*, Self-assembly of a nanoscale DNA box with a controllable lid. *Nature* **459**, 73–76 (2009). doi: 10.1038/nature07971; pmid: 19424153
23. S. M. Douglas *et al.*, Self-assembly of DNA into nanoscale three-dimensional shapes. *Nature* **459**, 414–418 (2009). doi: 10.1038/nature08016; pmid: 19458720
24. H. Dietz, S. M. Douglas, W. M. Shih, Folding DNA into twisted and curved nanoscale shapes. *Science* **325**, 725–730 (2009). doi: 10.1126/science.1174251; pmid: 19661424
25. D. Han *et al.*, DNA origami with complex curvatures in three-dimensional space. *Science* **332**, 342–346 (2011). doi: 10.1126/science.1202998; pmid: 21493857
26. B. Wei, M. Dai, P. Yin, Complex shapes self-assembled from single-stranded DNA tiles. *Nature* **485**, 623–626 (2012). doi: 10.1038/nature11075; pmid: 22660323
27. Y. Ke, L. L. Ong, W. M. Shih, P. Yin, Three-dimensional structures self-assembled from DNA bricks. *Science* **338**, 1177–1183 (2012). doi: 10.1126/science.1227268; pmid: 23197527
28. R. Iinuma *et al.*, Polyhedra self-assembled from DNA tripods and characterized with 3D DNA-PAINT. *Science* **344**, 65–69 (2014). doi: 10.1126/science.1250944; pmid: 24625926
29. E. Benson *et al.*, DNA rendering of polyhedral meshes at the nanoscale. *Nature* **523**, 441–444 (2015). doi: 10.1038/nature14586; pmid: 26201596
30. R. Veneziano *et al.*, Designer nanoscale DNA assemblies programmed from the top down. *Science* **352**, 1534 (2016). doi: 10.1126/science.aaf4388; pmid: 27229143
31. B. Yurke, A. J. Turberfield, A. P. Mills Jr., F. C. Simmel, J. L. Neumann, A DNA-fuelled molecular machine made of DNA. *Nature* **406**, 605–608 (2000). doi: 10.1038/35020524; pmid: 10949296
32. H. Yan, X. Zhang, Z. Shen, N. C. Seeman, A robust DNA mechanical device controlled by hybridization topology. *Nature* **415**, 62–65 (2002). doi: 10.1038/415062a; pmid: 11780115
33. M. Liu *et al.*, A DNA tweezer-actuated enzyme nanoreactor. *Nat. Commun.* **4**, 2127 (2013). pmid: 23820332
34. Y. Ke, T. Meyer, W. M. Shih, G. Bellot, Regulation at a distance of biomolecular interactions using a DNA origami nanoactuator. *Nat. Commun.* **7**, 10935 (2016). doi: 10.1038/ncomms10935; pmid: 26988942
35. W. B. Sherman, N. C. Seeman, A Precisely Controlled DNA Biped Walking Device. *Nano Lett.* **4**, 1203–1207 (2004). doi: 10.1021/nl049527q
36. P. Yin, H. Yan, X. G. Daniell, A. J. Turberfield, J. H. Reif, A unidirectional DNA walker that moves autonomously along a track. *Angew. Chem. Int. Ed.* **43**, 4906–4911 (2004). doi: 10.1002/anie.200460522; pmid: 15372637
37. T. Omabegho, R. Sha, N. C. Seeman, A bipedal DNA Brownian motor with coordinated legs. *Science* **324**, 67–71 (2009). doi: 10.1126/science.1170336; pmid: 19342582
38. P. Yin, H. M. T. Choi, C. R. Calvert, N. A. Pierce, Programming biomolecular self-assembly pathways. *Nature* **451**, 318–322 (2008). doi: 10.1038/nature06451; pmid: 18202654
39. K. Lund *et al.*, Molecular robots guided by prescriptive landscapes. *Nature* **465**, 206–210 (2010). doi: 10.1038/nature09012; pmid: 20463735
40. S. F. J. Wickham *et al.*, Direct observation of stepwise movement of a synthetic molecular transporter. *Nat. Nanotechnol.* **6**, 166–169 (2011). doi: 10.1038/nnano.2010.284; pmid: 21297627
41. L. Feng, S. H. Park, J. H. Reif, H. Yan, A two-state DNA lattice switched by DNA nanoactuator. *Angew. Chem. Int. Ed.* **42**, 4342–4346 (2003). doi: 10.1002/anie.200351818; pmid: 14502706
42. A. E. Marras, L. Zhou, H.-J. Su, C. E. Castro, Programmable motion of DNA origami mechanisms. *Proc. Natl. Acad. Sci. U.S.A.* **112**, 713–718 (2015). doi: 10.1073/pnas.1408869112; pmid: 25561550
43. J. R. Burns, A. Seifert, N. Fertig, S. Howorka, A biomimetic DNA-based channel for the ligand-controlled transport of charged molecular cargo across a biological membrane. *Nat. Nanotechnol.* **11**, 152–156 (2016). doi: 10.1038/nnano.2015.279; pmid: 26751170
44. R. J. Brownlie, R. Zamoyska, T cell receptor signalling networks: Branched, diversified and bounded. *Nat. Rev. Immunol.* **13**, 257–269 (2013). doi: 10.1038/nri3403; pmid: 23524462
45. S. M. Du, S. Zhang, N. C. Seeman, DNA junctions, antijunctions, and mesojunctions. *Biochemistry* **31**, 10955–10963 (1992). doi: 10.1021/bi00160a003; pmid: 1332747
46. P. C. Nickels *et al.*, Molecular force spectroscopy with a DNA origami-based nanoscopic force clamp. *Science* **354**, 305–307 (2016). doi: 10.1126/science.aah5974; pmid: 27846560
47. P. Yakovchuk, E. Protozanova, M. D. Frank-Kamenetskii, Base-stacking and base-pairing contributions into thermal stability of the DNA double helix. *Nucleic Acids Res.* **34**, 564–574 (2006). doi: 10.1093/nar/gkj454; pmid: 16449200
48. J. Song *et al.*, Direct visualization of transient thermal response of a DNA origami. *J. Am. Chem. Soc.* **134**, 9844–9847 (2012). doi: 10.1021/ja3017939; pmid: 22646845
49. M. Endo *et al.*, Helical DNA origami tubular structures with various sizes and arrangements. *Angew. Chem. Int. Ed.* **53**, 7484–7490 (2014). doi: 10.1002/anie.201402973; pmid: 24888699
50. J.-P. Changeux, The feedback control mechanisms of biosynthetic L-threonine deaminase by L-isoleucine. *Cold Spring Harb. Symp. Quant. Biol.* **26**, 313–318 (1961). doi: 10.1101/SQB.1961.026.01.037; pmid: 13878122
51. J.-P. Changeux, S. J. Edelstein, Allosteric mechanisms of signal transduction. *Science* **308**, 1424–1428 (2005). doi: 10.1126/science.1108595; pmid: 15933191
52. O. Schueler-Furman, S. J. Wodak, Computational approaches to investigating allostery. *Curr. Opin. Struct. Biol.* **41**, 159–171 (2016). doi: 10.1016/j.sbi.2016.06.017; pmid: 27607077
53. L. Yan, R. Ravasio, C. Brito, M. Wyart, Architecture and coevolution of allosteric materials. *Proc. Natl. Acad. Sci. U.S.A.* **114**, 2526–2531 (2017). doi: 10.1073/pnas.1615536114; pmid: 28223497
54. Y. Ke, S. Lindsay, Y. Chang, Y. Liu, H. Yan, Self-assembled water-soluble nucleic acid probe tiles for label-free RNA hybridization assays. *Science* **319**, 180–183 (2008). doi: 10.1126/science.1150082; pmid: 18187649
55. S. Rinker, Y. Ke, Y. Liu, R. Chhabra, H. Yan, Self-assembled DNA nanostructures for distance-dependent multivalent ligand-protein binding. *Nat. Nanotechnol.* **3**, 418–422 (2008). doi: 10.1038/nnano.2008.164; pmid: 18654566
56. F. Kilchherr *et al.*, Single-molecule dissection of stacking forces in DNA. *Science* **353**, aaf5508 (2016). doi: 10.1126/science.aaf5508; pmid: 27609897
57. S. M. Miick, R. S. Fee, D. P. Millar, W. J. Chazin, Crossover isomer bias is the primary sequence-dependent property of immobilized Holliday junctions. *Proc. Natl. Acad. Sci. U.S.A.* **94**, 9080–9084 (1997). doi: 10.1073/pnas.94.17.9080; pmid: 9256438
58. S. Hohng *et al.*, Fluorescence-force spectroscopy maps two-dimensional reaction landscape of the holliday junction. *Science* **318**, 279–283 (2007). doi: 10.1126/science.1146113; pmid: 17932299
59. F. A. Aldaye, A. L. Palmer, H. F. Sleiman, Assembling materials with DNA as the guide. *Science* **321**, 1795–1799 (2008). doi: 10.1126/science.1154533; pmid: 18818351
60. S. M. Douglas *et al.*, Rapid prototyping of 3D DNA-origami shapes with caDNAno. *Nucleic Acids Res.* **37**, 5001–5006 (2009). doi: 10.1093/nar/gkp436; pmid: 19531737

ACKNOWLEDGMENTS

We thank M. Dai, S. Jiang, M. Dong, B. Wei, H. Yan, and P. Yin for technical assistance and discussion. This work was supported by NSF CAREER Award DMR–1654485, the Wallace H. Coulter Department of Biomedical Engineering Startup Fund, a Billi and Bernie Marcus Research Award to Y.K., Office of Naval Research grant N00014-15-1-2707 and NSF grant CMMI–1437301 to C.M., a National Natural Scientific Foundation of China Grant 21605102 to J.S., and NIH grants GM084070 and 3R01GM084070-07S1 to L.F. All data are reported in the main text and supplementary materials.

SUPPLEMENTARY MATERIALS

www.sciencemag.org/content/357/6349/eaan3377/suppl/DC1
Materials and Methods
Figs. S1 to S40
Tables S1 to S13
Movie S1

29 March 2017; accepted 6 June 2017
Published online 22 June 2017
10.1126/science.aan3377